GRANULAR DYNAMICS:
CLUSTERING AND SHEAR FLOWS

The research described in this thesis is part of the research programme of the “Stichting voor Fundamenteel Onderzoek der Materie” (FOM), which is financially supported by the “Nederlandse Organisatie voor Wetenschappelijk Onderzoek” (NWO). It was carried out at the Physics of Fluids research group of the faculty of Science and Technology of the University of Twente, and at the Leiden Institute of Physics.

Publisher:
René Mikkelsen, Physics of Fluids, University of Twente,
P. O. Box 217, 7500 AE Enschede, the Netherlands

Print: PrintPartners Ipskamp B.V., Enschede

ISBN 90-365-2141-6

GRANULAR DYNAMICS:
CLUSTERING AND SHEAR FLOWS

PROEFSCHRIFT

ter verkrijging van
de graad van doctor aan de Universiteit Twente,
op gezag van de rector magnificus,
prof. dr. W.H.M. Zijm,
volgens besluit van het College voor Promoties
in het openbaar te verdedigen
op woensdag 23 februari 2005 om 15.00 uur

door

René Mikkelsen

geboren op 20 juli 1974

te Nykøbing Falster

Dit proefschrift is goedgekeurd door de promotor:
Prof. dr. rer. nat. D. Lohse

Contents

Chapter 1

Introduction

Granular matter is all around us. For example, much of the food we eat has at some point been in a granular form; think of rice, sugar, corn or flour. Dependent on how they are prepared and handled, granular materials can behave as unusual solids, fluids or gases. The combination of their ability to show a broad range of behaviors and the relative simplicity of experiments on granular media make them so attractive from a physicists point of view. However, the description of granular matter is not only interesting because of their surprising behavior, but is also of great relevance for the design and optimization of many industrial processes. The handling and processing of grains and powders plays an important role in industrial processes such as mining, agriculture and the production of pharmaceuticals.

Granular media are large collections of macroscopic particles (grains), sand being an archetypical example [1]. Typical particle sizes are of the order of 100 μm or more, which means that thermal fluctuations play no role and ordinary thermodynamic temperature is irrelevant. In this sense, granular media are *athermal*. Interactions between the grains are dissipative: grains in contact experience repulsive and frictional forces, and particle collisions are inelastic. As a consequence, if no external energy is supplied, granular media get stuck in a metastable state such as a sand heap. We know from experience that collectively, granular media can not only behave as an (unusual) solid, but also as a peculiar liquid or gas. For example, sand flowing through an hourglass behaves fluid-like, while sand in a strongly vibrated container is in a gas-like state. In both cases, energy is supplied externally to overcome the dissipative grain-grain interactions, and clearly such states are far away from equilibrium.

In this thesis we study the behavior of granular media when they are

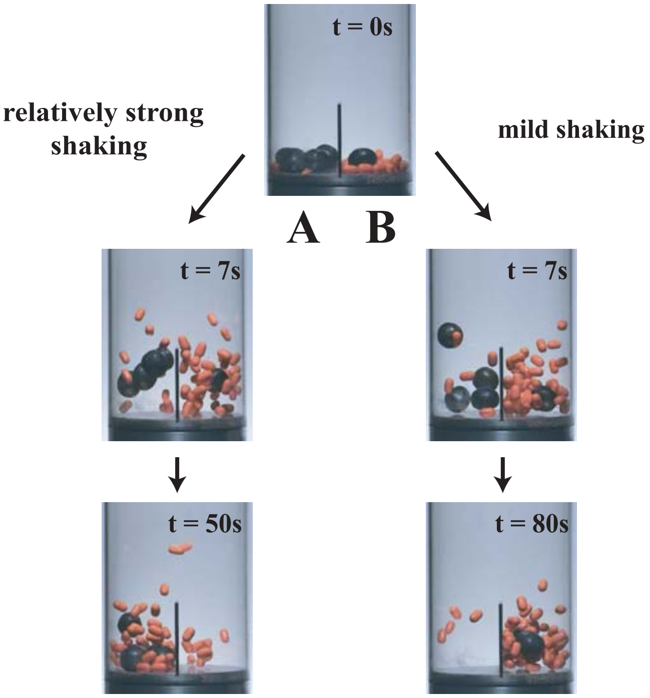

Figure 1.1: Images from two competitive clustering experiments using candy (pictures published in [7]): at relatively strong shaking (f=75 Hz, a=1.25 mm) the mixture clusters in compartment A initially containing mainly large particles. At mild shaking (f=60 Hz, a=1.25 mm) they cluster in the other compartment, initially dominated by the smaller particles.

driven by vibrations, by impact or by applying external shear forces. The first set of experiments considers clustering behavior of compartmentalized granular gases, the second set studies the impact of a heavy sphere ("meteor") on a loose bed of very fine sand, and the final experiments deal with inhomogeneous velocity profiles in sheared dense granular materials.

The clustering behavior of compartmentalized granular gases is studied in Chapters 2-4. When grains in a single container are vibrated sufficiently strong, they lose contact and start to bounce around; this we refer to as a granular gas. It is customary then to define the granular temperature as the mean kinetic energy of the particles. The external energy that is supplied to the grains when they collide with the moving container is dissipated during grain collisions. As we will discuss in Chapter 2 in more detail, such gas-like states are prone to clustering [2, 3] . This is because in locally "cold",

Figure 1.2: Jet created when a solid sphere impacts on loosely packed, fine sand. Notice that the maximum height of the jet exceeds the release height.

dense regions, grain collisions are more frequent than in “hot” regions, so that cold regions cool faster than hot regions, leading to instabilities. In Chapter 3-4 we discuss this clustering instability in a compartmentalized system: when two connected grain-filled compartments are vibrated, clustering occurs whereby most grains cluster in one of the compartments and end up being “cold”. The transition between this clustered state and the state in which both compartments are equally dense and hot can be tuned by parameters such as shaking strength, size and location of the hole where particle exchange takes place. For large amounts of grains this clustering can be described quite well with a simple model in which the order parameter basically represents the particle densities in the container. However, for small amounts of grains, fluctuations in the particle exchange between the two compartments starts to play an important role. This is incorporated into the simple model by an additional noise term. This noise is characterized and studied by means of numerical simulations in Chapter 3. We find that the noise is approximately Gaussian, and for high noise levels, i.e. for small number of grains, it is able to break down the mean-field behavior of the transition between the uniform and clustered states [4].

Granular media that consist of mixtures of strongly different grains, for example grains of different size, are difficult to mix; in fact, in many situations size-segregation takes place. A famous example is the “Brazil Nut” effect, where a large particle (the nut) surrounded by smaller ones rises to the surface when the whole assembly is vibrated [5]. One may also encounter (co-axial) segregation in rotating drums, in which sharply separated bands of similar-sized particles form. When these are colored differently, one can observe beautiful “snake” patterns [6]. In Chapter 4 we find that size seg-

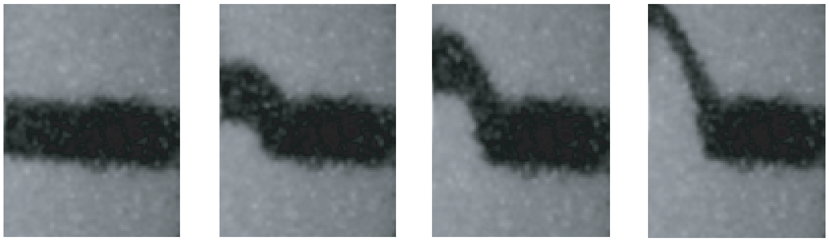

Figure 1.3: Frames showing the surface flow of a sheared granular material (1 mm glass beads), where a line of black particles is added to illustrate the grain motion. A narrow shear band is created where the material deforms, while the rest of the material remains solid-like.

regation also plays a role when two connected boxes filled with a bidisperse mixture of grains are vibrated. Dependent on the shaking strength the clustering can be directed either towards the compartment initially containing mainly small particles or to the one containing mainly large particles [7–9].

An example of bidisperse clustering is shown in Figure 1.1, where a mixture of candies ("Tic-Tac's" and "Salmiakbollen"), starting out from the same initial distribution, cluster in compartment A or B depending on the shaking strength.

In Chapter 5 we study the jet that occurs when we drop a heavy ball in a very loose packing of fine sand (see Figure 1.2). Upon impact a crater is formed which collapses due to the sand pressure and an upward jet emerges. For high impact velocities air is entrained beneath the surface, which slowly rises to the surface causing a granular eruption [10, 11].

Finally, in Chapter 6 we study the slow flow of granular media. When external stresses are imposed on a dense granular medium, it does not flow uniformly as a normal fluid would do under the same conditions. Instead narrow shear bands are formed where the material yields and flows, while the rest of the material remains solid-like and barely deforms (see Figure 1.3). Typically these shear bands are 5-10 grain diameters wide, hindering mixing, making grain flow hard to predict, and forming a major obstacle for any continuum description. Here we study in detail the difference between shear bands located in the bulk and near the wall, and in particular the transition between these two regimes [12].

References

[1] H. M. Jaeger, and S. R. Nagel, Rev. Mod. Phys. **68**, 1259 (1996).

[2] I. Goldhirsch and G. Zanetti, Phys. Rev. Lett. **70**, 1619 (1993).

[3] L.P. Kadanoff, Rev. Mod. Phys. **71**, 435 (1999).

[4] R. Mikkelsen, K. van der Weele, D. van der Meer, M. van Hecke, and D. Lohse, submitted to Phys. Rev. E (2004).

[5] J. B. Knight, H. M. Jaeger, and S. R. Nagel, Phys. Rev. Lett. **70**, 2431 (1993).

[6] M. Newey, S. Van der Meer, J. Ozik, E. Ott, and W. Losert, Europhys. Lett. **66**, 205 (2004).

[7] R. Mikkelsen, K. van der Weele, D. van der Meer, M. Versluis, and D. Lohse, Phys. Fluids **15**, S8 (2003).

[8] R. Mikkelsen, D. van der Meer, K. van der Weele and D. Lohse, Phys. Rev. Lett. **89**, 214301 (2002).

[9] R. Mikkelsen, D. van der Meer, K. van der Weele, and D. Lohse, Phys. Rev. E, *in press* (2004).

[10] R. Mikkelsen, M. Versluis, E. Koene, G.-W. Bruggert, D. van der Meer, K. van der Weele, and D. Lohse, Phys. Fluids **14**, S14 (2002).

[11] D. Lohse, R. Bergman, R. Mikkelsen, C. Zeilstra, D. van der Meer, M. Versluis, K. van der Weele, M. van der Hoef, and H. Kuipers, Phys. Rev. Lett. **93**, 198003 (2004).

[12] R. Mikkelsen, D. Fenistein, and M. van Hecke, preprint (2005).

Chapter 2

Cluster formation in compartmentalized granular gases §

Abstract

A brief overview is given of the recent studies into cluster formation in compartmentalized gases, focusing upon the so-called Maxwell Demon effect. A common thread in these studies is that the clustering is related to the fact that the particle flux from a compartment, or the granular pressure, is a non-monotonic function of the number of particles in the compartment.

2.1 Introduction

One of the characteristic features of granular gases is their tendency to spontaneously separate in dense and dilute regions [1–3]. This property, which makes them fundamentally different from any ordinary molecular gas, can be traced back to the fact that the collisions between the granular particles are inelastic. Every time two particles collide, their relative velocity is reduced proportional to the coefficient of normal restitution $0 \leq e < 1$. The case $e = 1$ corresponds to a standard elastic gas in which no clustering occurs.

[§] Adapted from: Ko van der Weele, René Mikkelsen, Devaraj van der Meer, and Detlef Lohse, in *The Physics of Granular Media*, edited by H. Hinrichsen and D.E. Wolf (Wiley, Weinheim, 2004) 117-139.

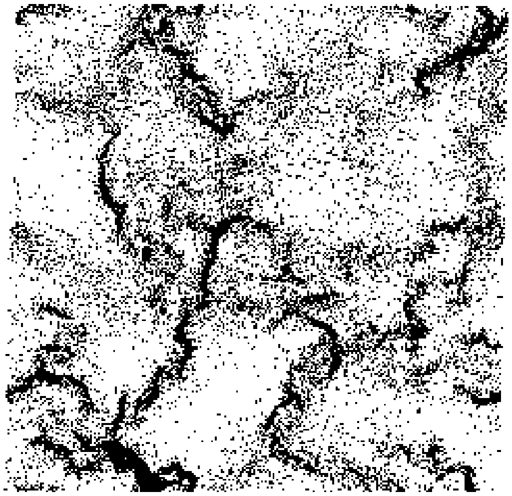

Figure 2.1: Cluster formation in a simulated system of 40,000 disks colliding inelastically (with coefficient of restitution $e = 0.6$) on a frictionless floor, after a time corresponding to 500 collisions per particle. The area fraction covered by the disks is 0.05, and periodic boundary conditions are used in both directions (from [5]).

The clustering effect was first demonstrated in numerical studies of rapid granular shear flows [4], and freely cooling granular gases [5]. Figure 2.1, from the seminal paper by Goldhirsch and Zanetti [5], shows cluster formation in a simulated two-dimensional system consisting of 40,000 disks, colliding inelastically (like hockey pucks on a frictionless ice floor) with restitution coefficient $e = 0.6$. The particles start out from a spatially homogeneous state, with a Maxwellian velocity distribution, and are left to evolve without further energy input, which means that the mean kinetic energy (or equivalently, the granular temperature, as described in the Introduction) decays with time due to the inelastic collisions.

The clustering process can be understood as follows [5]: In a region where, due to some fluctuation, the density exceeds the average density of the gas, the collision rate is higher and the granular temperature will therefore drop faster than in the neighboring, less dense regions. In hydrodynamical terms this means that a pressure gradient is built up between high and low temperature (and thus pressure) regions, resulting in a migration of particles into denser regions from diluter ones. Hence the dense regions become denser, and the dilute regions diluter, and this self-enhancing process spontaneously leads to the formation of clusters (consisting of many slow particles) coexisting with almost empty regions (where the particles move much faster).

The above clustering mechanism also holds for granular gases that are kept at a constant granular temperature by an external energy input – typically by vertically vibrating the whole setup or its bottom [6, 7]. We choose to focus our attention on the cluster formation of such forced gases in a *compartmentalized* system. These are especially suited to get a clear-cut view of the clustering effect; moreover, they can be directly related to compartmentalized systems like sorting machines and conveyor belts, for which clustering is known to be a major source of problems [1, 8].

2.2 The vertically vibrated experiment

A striking illustration of the cluster formation in compartmentalized granular gases is provided by the experiment illustrated in Figure 2.2, which was first described by Schlichting and Nordmeier [9]. The setup consists of a box, mounted on a shaker, divided into two equally sized compartments by a wall extending from the bottom to height h. A few hundred beads are brought into a gaseous state by shaking the system vertically and are able to jump from one compartment to the other.

If the shaking is vigorous enough, the inelasticity of the gas is overwhelmed by the energy input into the system and the particles are distributed uniformly over the two compartments just as in any ordinary gas (Figure 2.2a). However, when the shaking strength is reduced below a critical level, the particles are seen to cluster into one of the compartments (Figure 2.2b-d). This goes on until a dynamical equilibrium is reached between the two compartments: the average outflow of rapid particles from the nearly empty compartment is balanced by the outflow of slow particles from the well-filled compartment. In terms of the granular temperature, one ends up with a “cold” compartment containing a lot of relatively slow particles, and a “hot” compartment containing only a few rapid particles.

This spontaneous separation in cold and hot regions is reminiscent of Maxwell’s demon [10, 11], a thought experiment constructed by Maxwell in 1871. This demon was supposed to guard the door between two rooms filled with a gas in thermodynamic equilibrium. Its task was to let slow molecules pass in one direction and fast molecules in the other and thus create one

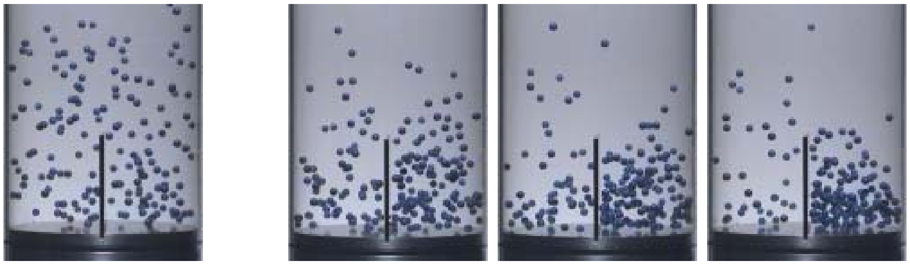

(a) (b) (c) (d)

Figure 2.2: Snapshots from the so-called Maxwell demon experiment. At vigorous shaking (a) the particles (glass beads with diameter 4 mm and restitution coefficient $e = 0.95$) are distributed uniformly over the two compartments. Reducing the shaking strength below a critical value results in the formation of a cluster in one of the compartments (b)-(d). Note that the particles in the dilute compartment jump higher than those in the dense compartment, i.e., the granular temperature is higher in the dilute compartment. The height of the wall is 60 mm.

cold and one hot room. The initial random distribution of molecules with various kinetic energies would then alter such that energy could be extracted from the system. The work of the demon violates the second law of thermodynamics, since it arranges the system into a more ordered state, thereby *decreasing* the systems entropy. The reason why the demon does not work in any ordinary gas is that in order to determine the energy of the molecules, it would have to interact with them, either physically or by exchanging photons, such that the demon itself gains entropy from the gas. The entropy of the whole system then increases, in agreement with the second law of thermodynamics. However, a granular gas can behave as if Maxwell's demon is present, thanks to the non-elasticity of the collisions and the fact that such a gas is intrinsically far from equilibrium. Entropy is transferred to the grains' microstructure by heating them up or by deforming them. However, ordinary temperature does not play a role for the grains, allowing the system to take on a more ordered state as far as macroscopical particle properties are concerned.

The gas is not isolated from the rest of the world: it constantly gets energy from outside, and via the inelastic collisions constantly transfers this energy to the microscopic scales (thereby effectively losing it) in the form of heat, sound, and deformation energy. The granular Maxwell Demon effect is of course not violating any law of physics, but is instead a prime example of pattern formation in a non-equilibrium system [12, 13], like e.g. Marangoni-

Bénard cells in a pan of oil heated from below [14], or sand ripples on the beach [15].

2.3 Eggers' flux model

A theoretical model for the Maxwell Demon effect was proposed by Eggers [10]. As a starting point, he took the condition for a dynamic equilibrium between the two compartments, namely that the flux of particles from left to right must equal that from right to left:

$$F_{l \to r} \quad = \quad F_{r \to l} \quad , \tag{2.1}$$

noting that an asymmetric equilibrium can only be explained if the particle flux from one compartment to the other is *not* a monotonously increasing function of the number of particles (as it would be for elastically colliding particles). Instead, it must show a maximum.

For simplicity, Eggers considered a 2-dimensional gas of colliding disks with radius r, in a slightly different setup than the one in Figure 2.2: The wall is taken to extend over the whole height of the system, with only a small opening (of width S) positioned at height h above the bottom. The bottom of the container is taken to move in a sawtooth manner, with amplitude a and frequency f, such that a colliding particle always finds it to move upward with the same velocity $v_b = af$. Moreover, the amplitude a is very small compared to the mean free path of the particles, so the bottom is effectively stationary.

Assuming the gas inside each compartment to be in a steady state, Eggers proceeds to derive an analytic expression for the particle outflow from each compartment, based on three equations from the kinetic theory of dilute granular gases [16]: (1) the equation of state relating the pressure, density, and temperature, (2) the force balance within the gas, which says how fast the pressure decreases with the height z above the bottom, and (3) the balance between the upward energy flux through the gas (fed by the vibrating bottom) and the dissipation due to the inelastic particle collisions. To minimize wall effects, which are not essential to the problem, all collisions with the walls and bottom are taken to be elastic.

The temperature profile $T(z)$ that is found on the basis of these equations, turns out to be close to constant, except for a narrow region of higher temperature near the bottom; this is the region where the energy is injected into the system and the particles have not yet had the opportunity to redistribute their kinetic energy via collisions. Taking for simplicity a

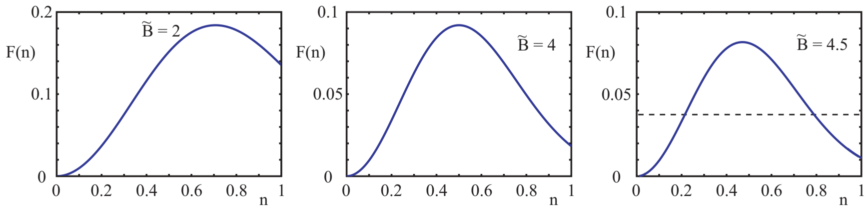

(a) (b) (c)

Figure 2.3: The Eggers flux function for the vertically vibrated system (equation (2.3)) with $A = 1$ s^{-1} and $\widetilde{B} = 2$ (a), $\widetilde{B} = 4$ (b), and $\widetilde{B} = 4.5$ (c), with n representing the particle fraction (in the compartment) relative to the total number of particles in the system. The dashed line indicates that the flux from a relatively empty compartment (left intersection point) can be equal to the flux from a well-filled compartment (right intersection point), which is exactly the condition for a clustered state; the associated fractions add up to 1. The symmetric state $n = 0.5$ (corresponding to a flux just to the right of the maximum of $F(n)$) is unstable at this value of $\widetilde{B}$.

constant temperature profile $T_k(z) = T_k$ throughout the compartment, with $k = 1, 2$ labelling the two compartments, one finds that the number density is exponentially decaying with z (as in the standard barometric height distribution), in fair agreement with molecular dynamics simulations [10]:

$$n_k(z) = \frac{g\bar{N}_k}{T_k} e^{-gz/T_k} \;, \quad \text{with} \quad T_k = \left(\frac{af}{2\sqrt{\pi} r (1-e^2) \bar{N}_k} \right)^2 \;. \tag{2.2}$$

Here $\bar{N}_k$ denotes the number of particles divided by the width of the compartment (N_k/L), r is the radius of a particle, and the expression for T_k ($\equiv \frac{1}{2}\langle v \rangle_k^2$) is obtained by balancing the energy input and the energy dissipated in collisions [10].

The particle flux from compartment k through the hole is then given by $n_k(h)\sqrt{T_k/2\pi}S$, i.e., the product of the number density at the height of the hole, the velocity in the horizontal direction, and the extension of the hole S. This can be worked out to yield

$$F(\bar{N}_k) = F_0 \bar{N}_k{}^2 e^{-b\bar{N}_k{}^2}, \tag{2.3}$$

where $F_0 = \sqrt{8\pi}(Sgr/af)(1-e^2)$ and $b = 4\pi g h r^2 (1-e^2)^2/(af)^2$.

In Figure 2.3 the above flux function is given in terms of n_k (i.e., the *fraction* of the total number of particles in compartment k) rather than $\bar{N}_k$.

Since $\bar{N}_k = N_k/L = n_k N_{tot}/L$ (with L the width of a compartment), the flux function then takes the form

$$F(n_k) = A n_k^2 e^{-\widetilde{B} n_k^2}, \tag{2.4}$$

with

$$A = \sqrt{8\pi} \frac{SgrN_{tot}^2}{afL^2}(1-e^2)\ , \qquad \widetilde{B} = 4\pi \frac{gh}{(af)^2}\left(\frac{rN_{tot}}{L}\right)^2 (1-e^2)^2\ . \tag{2.5}$$

This figure illustrates the Eggers theory, representing the particle flux $F(n_k)$ from any of the two compartments ($k = 1, 2$) as a function of the fraction of the total number of particles in that compartment, $\sum n_k = 1$. The one-humped form of the function makes it possible to have equal fluxes (or pressures) for the two compartments while the number of beads differ, which is precisely the requirement for a clustered state.

The dimensionless number $\widetilde{B}$ determines whether the system will end up in the uniform or in the clustered state. For a given choice of granular beads (r and e fixed), $\widetilde{B}$ can be raised either by increasing the height of the separating wall h or the total number of particles N_{tot}, or by *decreasing* the driving velocity af.

In the limit $\widetilde{B} \to 0$, the exponential term in equation (2.4) approaches unity and $F(n_k)$ thus grows monotonically with n_k (just as for an elastic gas with $e = 1$). This makes a balance between a well-filled and a nearly empty compartment impossible and the system settles into the homogeneous state.

As $\widetilde{B}$ is raised, however, the exponential term comes into play. This is depicted in Figure 2.3c for $A = 1\ \mathrm{s}^{-1}$ and $\widetilde{B} = 4.5$. The function $F(n_k)$ still starts out from zero at $n_k = 0$ and initially increases with n_k. However, beyond $n_k = 1/\sqrt{\widetilde{B}}$ the function goes down again, as a result of the dissipative effect of the increasingly frequent particle collisions. This enables a flux balance (see Figure 2.3c) between a well-filled and a dilute compartment, provided the maximum of $F(n_k)$ lies at a value $n_k < \frac{1}{2}$ (i.e., $\widetilde{B} > 4$). Now the condition $\sum n_k = 1$ can be satisfied not only for an equal pair $n_1 = n_2 = \frac{1}{2}$ (corresponding to a flux just to the right of the maximum in Figure 2.3c) but also for an unequal pair $n_1 \neq n_2$ (corresponding to a smaller flux, indicated by the horizontal dashed line).

The dynamics of the system is governed by the following balance equation,

$$\frac{dn_1}{dt} = -F(n_1) + F(n_2) + \xi_1 = -F(n_1) + F(1-n_1) + \xi_1\ \ , \tag{2.6}$$

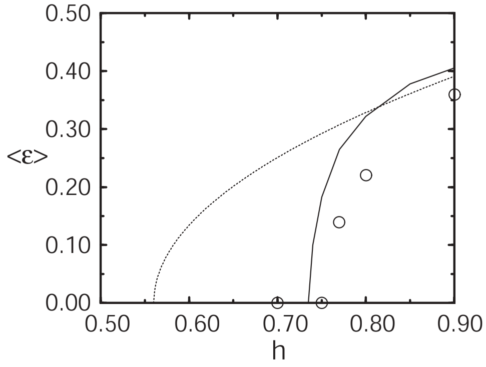

Figure 2.4: The bifurcation of the time-averaged asymmetry parameter ϵ as function of h (the height of the hole above the bottom) in the Eggers model. The circles represent numerical simulations with $N_{tot} = 360$ disks (radius 0.01 m, restitution coefficient $e = 0.95$), compartment width $L = 1.60$ m, and velocity of the bottom $af = 0.149$ m/s. The dotted line is the result of the flux model defined by equations (2.4)-(2.6), while the full line represents a more elaborate version of the model without the simplifying assumption that $T_k(z)$ is independent of z (from [10]).

(and analogously for dn_2/dt) which simply states that the time rate of change dn_k/dt of the particle fraction in the kth compartment is equal to the inflow from its neighbor minus the outflow from the compartment itself. The term ξ_1 models the noise which comes from statistical fluctuations in the particle flux [10]; without it, the above balance equation is to be interpreted as a mean field description.

In equilibrium, the two fluxes in equation (2.6) must cancel each other ($F(n_1) = F(1 - n_1)$), see equation (2.1). For $\widetilde{B} < 4$ this yields one solution $n_1 = \frac{1}{2}$ (the symmetric state). For $\widetilde{B} \geq 4$ this solution becomes unstable, but simultaneously two asymmetric stable solutions come into existence; one representing a state with a cluster in the left compartment and the second one its (equivalent) mirror image with a cluster in the right compartment. The clustering transition is depicted in Figure 2.4, where the absolute value of the (time-averaged) *asymmetry parameter*,

$$\epsilon = \frac{\bar{N}_k - \frac{1}{2}\bar{N}_{tot}}{\bar{N}_{tot}} = n_k - \frac{1}{2} \quad , \tag{2.7}$$

is plotted as function of h (the height of the hole above the bottom). The figure includes the results from molecular dynamics simulations of 360 inelastically colliding disks (open circles), the flux model defined by equations

(2.4)-(2.6) (dotted line), and the numerical result of the Eggers model without the simplifying assumption that $T(z)$ is independent of z (solid line) [10]. Even though there is an offset between the constant-T theory (dashed line) and the simulation, this theory using only one dimensionless parameter ($\widetilde{B}$) captures the form of the bifurcation fairly well. The transition to the clustered state is seen to be similar to a second-order, continuous phase transition. Just above the critical point the asymmetric solutions according to the dashed line are described by $\langle\epsilon\rangle = \pm[3(\widetilde{B}-4)/16]^{\beta}$ with a critical exponent $\beta = 1/2$. This is the common (mean field) power-law behavior near a second order phase transition [17].

In order to get an estimate for the amplitude of the fluctuations in the system, one may assume that the particles pass through the hole uncorrelated (which is equivalent to saying that ξ_1 in equation (2.6) is a Gaussian white noise term, with zero mean and a δ correlation function). The resulting variance of the asymmetry parameter, $\langle(\epsilon - \langle\epsilon\rangle)^2\rangle \propto |N_{tot}(\widetilde{B}-4)|^{-1/2}$, tells us that the relative amplitude of the fluctuations decreases with growing particle number (as expected) and that the divergence near the critical point $\widetilde{B} = 4$ goes with the exponent 1/2 typical of second order phase transitions [17]. Eggers notes that this model prediction is in reasonable agreement with numerical simulations [10]. This noise term will be discussed further in Chapter 3.

2.4 Extension to more than 2 compartments [§]

The transition to the clustered state was measured experimentally by van der Weele *et al.* [18], not only for the original system with two compartments but also for three compartments, and in a subsequent paper this was extended to an arbitrary number of K connected compartments [19]. The systems considered were 3-dimensional, as in Figure 2.2. This has no consequences for the general form of the flux function, which is still given by equation (2.4), but the two factors A and $\widetilde{B}$ now read (cf. equation (2.5)):

$$A = \sqrt{8\pi}\frac{Sgr^2N_{tot}^2}{af\Omega^2}(1-e^2)\ , \qquad \widetilde{B} = 4\pi\frac{gh}{(af)^2}\left(\frac{r^2N_{tot}}{K\Omega}\right)^2(1-e^2)^2 \equiv K^2B\ . \tag{2.8}$$

The opening S between the compartments is now a 2D surface (instead of a 1D length), and the compartment width L has been replaced by the ground

---

[§] The rest of this Chapter is a review of recent work by various other authors on the clustering phenomenon in compartmentalized systems. It appeared as a review paper (see footnote on page 7) and is kept here for completion.

area Ω.

For a system consisting of K compartments arranged cyclically, such that the Kth and 1st compartments are neighbors, the balance equation equation (2.6) takes the form (disregarding the noise term):

$$\frac{dn_k}{dt} = F(n_{k-1}) - 2F(n_k) + F(n_{k+1}) \quad , \tag{2.9}$$

with $k = 1, 2, ..., K$. For a non-cyclic arrangement the equation for the end compartments is modified, of course, but it turns out that this does not qualitatively change the results [19].

For the two-compartment system ($K = 2$), the experimental data confirm the second-order transition predicted by the flux model. This can be seen in Figure 2.5a, where the measured n_k (for both compartments $k = 1, 2$) are plotted as solid dots. In this figure, the factor $\widetilde{B}$ has been rescaled to B, so the critical value at which the transition takes place now lies at 1. The experiments were performed by changing the driving frequency f, while all the other quantities appearing in B were held fixed [18].

In contrast, for $K = 3$ compartments the clustering transition is found to be abrupt and hysteretic, i.e., a first-order phase transition.* Figure 2.5b shows the experimental results together with the flux model predictions for a cyclic three-compartment system [18]. The dots represent measurements from experiments that were started out from the uniform distribution $\{\frac{1}{3}, \frac{1}{3}, \frac{1}{3}\}$, and the crosses for those that were started from a single peaked distribution: They clearly show that there is an interval of B-values for which both the uniform and the clustered state are stable. The dashed curves for $B > 1$ that run above and below the horizontal line of the uniform state are associated with a transient state in which two of the compartments are competing for dominance, while the third compartment is already much more dilute. Staring out from the (unstable) uniform distribution, the system generally first goes through this transient state before it settles in the clustered equilibrium. No such transient states are encountered in the opposite transition for $B < 0.73$.

The same qualitative behavior, with a first-order transition, is found for all $K \geq 3$ [19]. Quantitatively, the hysteretic behavior gets more pronounced as the number of compartments is increased, and the transient states become more numerous and also more important. Figure 2.6a illustrates this for the

---

*There is a close analogy with the K-state Potts model here, i.e., an assembly of N_{tot} connected spins with K possible orientations per spin. Also in the Potts model one finds a phase transition of second order if $K = 2$ (the Ising case) and a transition of first order if $K \geq 3$ [20, 21].

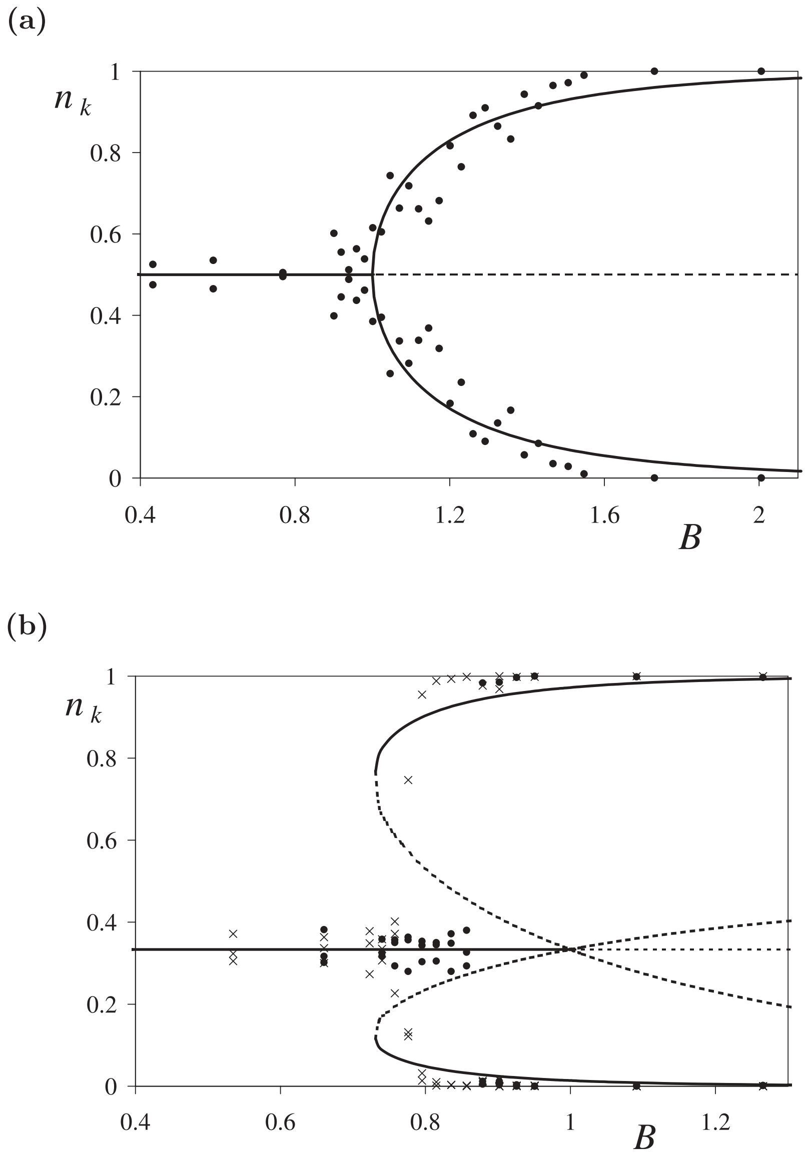

Figure 2.5: (a) Bifurcation diagram for the Maxwell demon experiment with $K = 2$ compartments ($k = 1, 2$). The dots are experimental data, and the lines are the stable (solid) and unstable (dashed) equilibria according to the flux model of Equations (2.4) and (2.8). The transition to the clustered state is a continuous one, i.e., a second-order phase transition. (b) The same for the 3-compartment experiment ($k = 1, 2, 3$). The dots and crosses are experimental data: dots for measurements that were started out from the uniform distribution $\{\frac{1}{3}, \frac{1}{3}, \frac{1}{3}\}$, and crosses for those that were started from a single peaked distribution. The transitions to and from the clustered state are abrupt and hysteretic, typical of a first-order phase transition (from [18]).

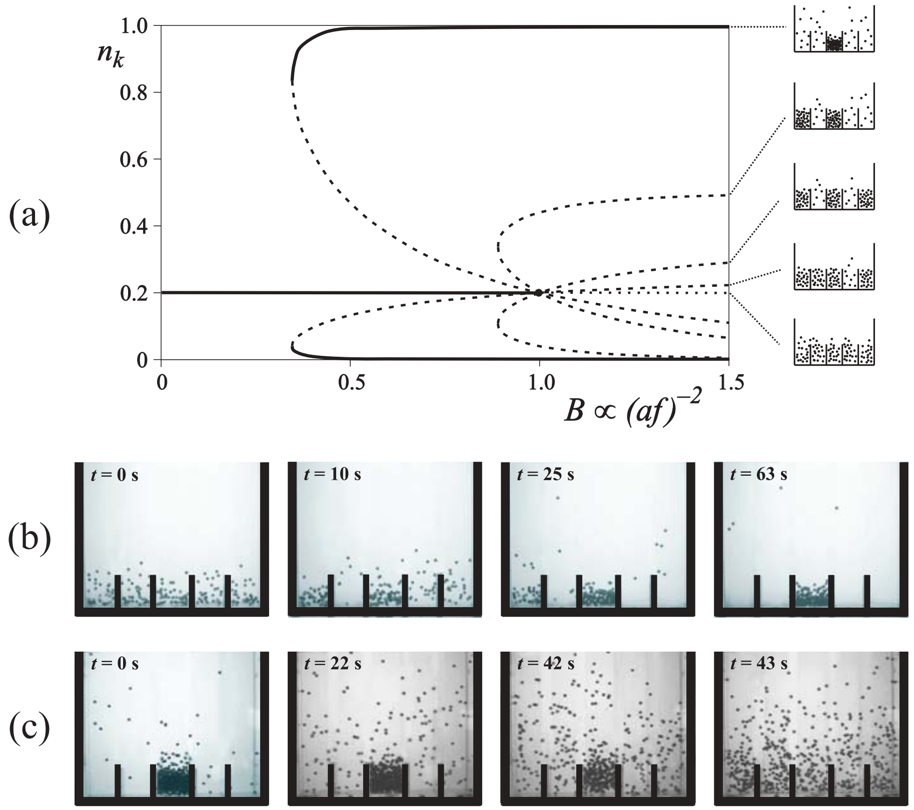

Figure 2.6: (a) Bifurcation diagram for $K = 5$ compartments. The sketches on the right depict typical configurations associated with the solid (stable) and dashed (unstable) equilibria of the flux model. (b) Four stages in a clustering experiment at B slightly above 1. The particles do not cluster directly into one compartment, but first go through a transient 2-cluster state, which can be seen in the snapshots at $t = 10$ s and $t = 25$ s. (c) Sudden collapse of a cluster at stronger shaking ($B = 0.33$): The cluster is clearly present until $t = 42$ s, then suddenly collapses, leaving no trace one second later (from [26]).

case of $K = 5$ non-cyclic compartments. The region of hysteresis (where the uniform and the clustered state are both stable) now extends from $B = 0.34$ to $B = 1$ and the dashed lines of the transient states form a whole web, reaching even to the left of $B = 1$. They correspond to states with $m = 2, 3, 4$ clusters, respectively, of which one representative configuration is depicted.

In Figure 2.6b four stages in the clustering process are shown, for a B-value slightly above 1, starting out from a nearly uniform distribution. A 2-cluster transient state is clearly visible at $t = 10$ s and $t = 25$ s, and it takes about a minute before the single-cluster state is reached. For larger values of K the experiment can easily get stuck in such a transient state (especially for low driving frequencies, i.e., $B \gg 1$) and it may take a very long time before the single-cluster state is reached, even though mathematically speaking this is the only truly stable state [19, 22]. The clusters collapse one by one in an exceptionally slow coarsening process: The characteristic size of the surviving clusters is found to increase as $[\log(t)]^{1/2}$ only [23].

The opposite process of *declustering*, depicted in Figure 2.6c, is also of interest. This is not only because declustering is more desirable in practical applications (e.g. in sorting machines, where clustering is an unwanted and often costly effect) but also because the breakdown of a cluster turns out to be by no means the same as clustering in reverse time order. Van der Meer *et al.* [24] found a surprising phenomenon called "sudden collapse": Starting out with all particles in one compartment, the cluster seems stable for a considerable time, spilling only a small number of particles to its neighbors. However, at a certain moment (between $t = 42$ s and 43 s in the experiment of Figure 2.6c) the cluster suddenly collapses and the particles spread out evenly over all compartments. The collapse, which can be delayed for extremely long times if B approaches the critical value where the single-cluster state becomes stable (with the cluster lifetime diverging as $(B_{crit} - B)^{-1/2}$), has been studied in detail in references [24] and [25].

2.5 Urn model

A different analysis of the Maxwell Demon experiment was given by Lipowski and Droz [28], who pictured it as a modified version of the Ehrenfest urn model [29]. The particles are initially distributed over two urns, and can change urn according to a probabilistic rule that mimics the behavior of granular matter. This approach was introduced to get a better insight into the role played by the statistical fluctuations, which had not been covered by the deterministic Eggers model (excluding the noise term in equation

(2.6)).

In the model defined in [28], the particles in each urn are subject to thermal fluctuations and the granular temperature T of an urn is taken to depend on its particle content as follows:

$$T(n_k) = T_0 + (1 - n_k)\Delta \quad , \tag{2.10}$$

where $n_k = N_k/N_{tot}$ is the fraction of particles in the urn, and T_0 and Δ are positive constants. So $T(n_k)$ decreases with n_k, as it should for a granular gas, yet the linear decay (from $T(0) = T_0 + \Delta$ to $T(1) = T_0$) is markedly different from the inverse square dependence derived by Eggers, cf. equation (2.2).

The rule by which the particles change urn is defined as follows: (*i*) One of the N_{tot} particles is selected randomly, and (*ii*) with probability $\exp(-1/T(n_k))$ it changes urn. This yields the following expression for the flux out of an urn:

$$F(n_k) = n_k \; e^{-1/T(n_k)} \quad , \tag{2.11}$$

which is a again one-humped function of the particle fraction n_k. Note that in the limit of infinite temperature ($T_0 = \infty$ and $\Delta \geq 0$ arbitrary) the original Ehrenfest model is recovered, for which every selected particle changes urn.[†]

Given the flux function, the dynamics of the system is governed by the same balance equation as in the Eggers model (cf. equation (2.6)):

$$\frac{dn_1}{dt} = -F(n_1) + F(1 - n_1) \quad . \tag{2.12}$$

The zeros of this equation are the equilibrium states of the system, and their stability can be found by plotting dn_1/dt as function of n_1 and examining its slope. If dn_1/dt goes through zero with a downward slope, the dynamics is directed (locally) towards this zero and the corresponding equilibrium is stable. Vice versa, an upward slope corresponds to an unstable equilibrium.

In this way, the phase diagram of Figure 2.7a can be constructed. The uniform equilibrium $n_1 = 1/2$ exists for all values of T_0 and Δ, and it is stable everywhere except in region II.

If one follows a path through this phase diagram (by changing the values of T_0 and Δ in very small steps, and very slowly, such that every time the

---

[†] Bena *et al.* [30] study a closely related urn model with $F(n_k) = n_k \exp(-An_k)$. They describe the second-order clustering transition (at $A = 2$) in terms of the Yang-Lee theory of phase transitions.

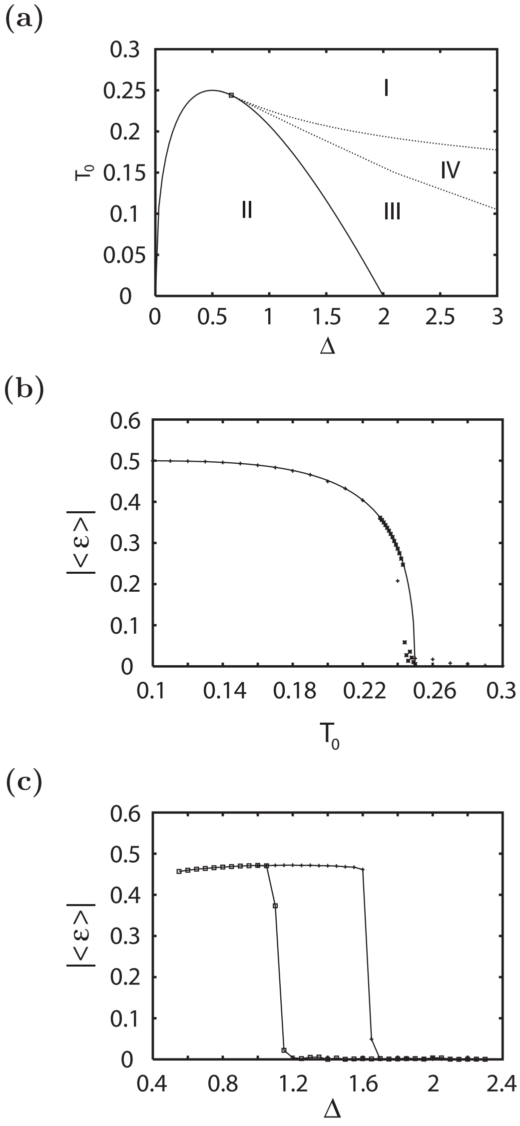

Figure 2.7: (a) Phase diagram of the urn model. The symmetric state ($\langle\epsilon\rangle = 0$) is stable in regions I, III, and IV , and unstable in region II. In regions II, III, and IV a stable asymmetric state exists ($|\langle\epsilon\rangle| \neq 0$). In regions III and IV one can therefore end up in either the symmetric or the asymmetric state depending on the initial condition; the dashed line separating region III from IV is described in the text. (b) Bifurcation diagram of the asymmetry parameter $|\langle\epsilon\rangle|$ as a function of T_0, for $\Delta = 0.5$ fixed, showing the second-order phase transition between regions II and I. The solid curve corresponds to the numerical solution of equation (2.12). The symbols are the result of Monte Carlo simulations for N_{tot}=500 (+) and 5000 ($*$), respectively. (c) Hysteretic, first-order transition of $|\langle\epsilon\rangle|$ as a function of Δ, for $T_0 = 0.2$ fixed, calculated from Monte Carlo simulations for $N_{tot} = 2000$. Symbols (+) correspond to increasing Δ, and ($\square$) to decreasing Δ (from [28]).

system can adjust itself to its new equilibrium) one finds, upon crossing the line between regions I and II from the left, a second order-phase transition. The uniform state $n_1 = 1/2$ undergoes a pitchfork bifurcation, in which it becomes unstable and simultaneously gives birth to two stable asymmetric solutions (one corresponding to $n_1 > 1/2$, and one to its mirror image with $n_1 < 1/2$). This is analogous to what is found in the two-compartment Maxwell demon experiment.

However, if one follows the path further in the direction of region III, additional bifurcations are encountered that are *not* found in the original experiment. Upon entering region III, the symmetric state is re-stabilized via a second pitchfork bifurcation, simultaneously giving birth to two new, unstable asymmetric states. The already existing *stable* asymmetric states are not affected by this bifurcation.

Through regions III and IV, the two unstable asymmetric states grow towards their stable counterparts and eventually, upon crossing the line between IV and I they coalesce and annihilate each other in a reverse saddle-node bifurcation. We then enter region I again, where only the stable symmetric state remains.

The above three bifurcations can all be seen in Figure 2.7b-c, where the absolute value of the time-averaged asymmetry parameter $\epsilon = (N_1 - N_2)/2N_{tot}$ is plotted as a function of the control parameter; this is T_0 in the first plot, and Δ in the second. First, in Figure 2.7b we follow a *vertical* path through the phase diagram at a constant value of $\Delta = 0.5$, with a clear second-order phase transition at $T_0 = 0.25$. The critical point corresponds precisely with the top of the boundary curve between regions I and II $T_0 = \sqrt{\Delta/2} - \Delta/2$. Lipowski and Droz checked that in the vicinity of the critical point the asymmetry parameter $|\langle\epsilon\rangle| \propto |T_0 - 0.25|^\beta$, with the usual critical exponent $\beta = 1/2$, just as in the Eggers model.

Second, in Figure 2.7c we follow a *horizontal* path through the phase diagram at a constant value of $T_0 = 0.2$. If the horizontal axis would have started at $\Delta = 0$, one would also have seen the second-order phase transition at $\Delta = \frac{1}{2}(1 - \sqrt{1 - 4T_0})^2 = 0.153$, associated with the border between regions I and II. As it is, we see the bifurcations at the lines between regions II and III (at $\Delta \approx 1.1$) and IV and I (at $\Delta \approx 1.7$). Together they form a hysteretic, first-order transition between the stable clustered state and the uniform distribution.

There is no bifurcation between III and IV. Nevertheless, in the phase diagram of Figure 2.7a there is a dashed line between III and IV emanating from the tricritical point at $\Delta = \frac{2}{3}, T_0 = (\sqrt{3} - 1)/3 = 0.244$. This line has been determined by considering the probability distribution $p(M, t)$, i.e,

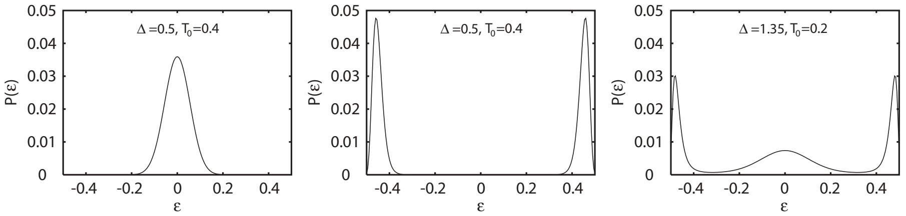

Figure 2.8: Probability distributions $P(\epsilon)$ for the urn model in region I (left), region II (center), and region III (right) in the long-time limit for $N_{tot} = 200$ particles (from [28]).

the probability that a given urn (say 1) contains M particles at time t, as outlined below.

The evolution equations for $p(M, t)$ follow directly from the dynamical rules of the urn model and can be solved numerically, starting from arbitrary initial conditions [28]. Figure 2.8 shows three typical probability distributions, expressed in terms of the asymmetry parameter ϵ, in the long-time limit $t \to \infty$. The left plot, characteristic for region I, shows the single-peak distribution around $\epsilon = 0$ corresponding to the symmetric state: $p(\epsilon) \propto \exp(-\epsilon^2)$, see also [31, 32]. The middle plot, representing region II, shows two peaks away from the center, corresponding to the clustered states. These plots are for $N_{tot} = 200$ particles; the width of the peaks decreases with growing N_{tot}. The critical probability distribution on the border line between regions I and II (for $\Delta < 1/3$) has been determined in references [31, 32] to have the form $p(\epsilon) \propto \exp(-\epsilon^4)$, i.e., a peak with a flattened top. At the tricritical point (for $\Delta = 1/3$) the top flattens even further to $p(\epsilon) \propto \exp(-\epsilon^6)$.

Going into regions III and IV, the probability distribution becomes more complicated and consists of three peaks, since both the symmetric and the asymmetric state are stable here. For comparatively small N_{tot}, as in the right plot of Figure 2.8, all three peaks are clearly visible, but in the thermodynamic limit $N_{tot} \to \infty$ either the central peak vanishes (in region III) or the two outer peaks (in region IV) [28, 32]. This reflects the relative probability to end up in either the symmetric or the asymmetric state, starting from random initial conditions. On the line that separates regions III and IV the three peaks are equally strong; this is interpreted by Lipowski and Droz as a line of discontinuous transitions, based on a phenomenological analogy with the same kind of phase transition in equilibrium statistical mechanics.

One of the main goals of the urn model was to study the fluctuations of the symmetry parameter close to the critical point. Making use of the variance of ϵ, and the calculated probability distribution in the long-time limit $p(i,\infty)$, the susceptibility κ is defined as [28]:

$$\kappa = N_{tot}\langle(\epsilon - \langle\epsilon\rangle)^2\rangle = \frac{1}{N_{tot}}\left(\sum_{i=0}^{N_{tot}} i^2 p(i,\infty) - \left[\sum_{i=0}^{N_{tot}} i\ p(i,\infty)\right]^2\right) \quad . \tag{2.13}$$

At a continuous phase transition the susceptibility is known to diverge, and indeed, that is exactly what is found at the transition between regions I and II. The measured data close to the critical point in Figure 2.7b indicate that $\kappa \propto |T_0 - 0.25|^{-\gamma}$, both in the symmetric and (albeit less clearly) in the asymmetric state, with the mean field exponent $\gamma = 1$ [17, 28].

Finally, the urn model has been extended to more than two urns by Coppex, Droz and Lipowski [20]. The K urns are arranged cyclically, and one allows only nearest neighbor interactions, according to the same selection rule as before. The resulting model is analogous to the K-compartment model described in Section 2.4, and despite the rather peculiar temperature convention (which was at the root of the unprecedented first-order transition in the case of two urns) the results are very similar.

In particular, for $K = 3$ it is found that the transition between the uniform and the clustered state is always of first order and accompanied by hysteresis. Also the unstable transient state (with two well-filled urns while the third one is nearly empty, $n_1 = n_2 > n_3$) is recovered, and even the sudden collapse phenomenon has been re-examined in the context of this model.

All particles are initially put in one urn, and the two parameters T_0 and Δ are chosen such that the system lies *just outside* the region of stability of the cluster. In Figure 2.9a the time evolution of the cluster fraction ($n_{cl}(t)$) is shown for different values of T_0 close to the critical value of $T_{0,c} = 0.1698$, at a fixed value of $\Delta = 0.3$. The behavior is markedly similar to that of a real granular cluster, and for comparison we have included in Figure 2.9b an analogous plot for the five fractions in our 5-compartment system of Figure 2.6c and reference [24]. After some initial spilling, in both cases a situation is reached where the cluster fraction decreases only slightly. At a certain point, however, it suddenly collapses and the particles are spread out uniformly over the K compartments. The first three curves in Figure 2.9a (for $T_0 = 0.1710, 0.1705$ and 0.1703, respectively) show that the lifetime of the cluster grows strongly as T_0 approaches the critical value, in agreement with the divergence found in [24, 25]; and beyond this point the lifetime becomes infinitely long, since the clustered state is stable there, as is indicated by the fourth curve (for $T_0 = 0.1690$).

There is only one dissimilarity between the urn model and the Eggers flux model for K compartments, and this concerns the diffusion towards the uniform state after the sudden collapse. In the urn model, the width of the density profile over the urns grows as $t^{1/2}$, with the standard exponent 1/2 known from random-walker diffusion, whereas the Eggers model yields an anomalous diffusion exponent 1/3 [24]. These different exponents are related to the small-density behavior of the flux functions, which goes as $F(n_k) \propto n_k$ in the urn model and as $F(n_k) \propto n_k^2$ in the Eggers model. Indeed, it can be shown that for the general case $F(n_k) \propto n_k^\alpha$ the diffusion exponent is given by $1/(1+\alpha)$ [27].

2.6 Horizontally vibrated system

An elegant variation on the Maxwell Demon experiment was introduced by Brey *et al.* [33], who considered the horizontally vibrated system depicted in Figure 2.10 (left). It consists of a box, here seen in top view, divided in two equal compartments containing a number of inelastically colliding particles. Energy is injected into the system via the vibrating bottom wall. Just as in the Eggers model, the wall is taken to vibrate in a sawtooth manner (with an amplitude that is much smaller than the mean free path of the particles) and collisions with the walls are taken to be elastic.

The bifurcation diagram for this system is shown in Figure 2.10 (right). Here the absolute value of the time-averaged asymmetry parameter ϵ is plotted as a function of a dimensionless parameter ξ_m, which is proportional to N_{tot} [33]). So the total number of particles is the control parameter here, while all other parameters are kept fixed.[‡] For a sufficiently small number of particles, a steady state is reached with all particles distributed equally over the two compartments. But if N_{tot} is increased beyond a critical value, the symmetry is spontaneously broken and the vast majority of the particles clusters together in one compartment.

To explain these observations, Brey *et al.* use a model based on a hy-

---

[‡] This choice of control parameter could have been made in the original Maxwell Demon experiment as well (cf. the dimensionless number $\widetilde{B}$ in equation (2.8)). Conversely, the control parameter used in that experiment (the velocity af of the vibrating wall) is *not* a valid control parameter here; Brey *et al.* find that the bifurcation diagram is not altered by modifying the velocity of the bottom, as long as it is large enough to keep the system fluidized [33].

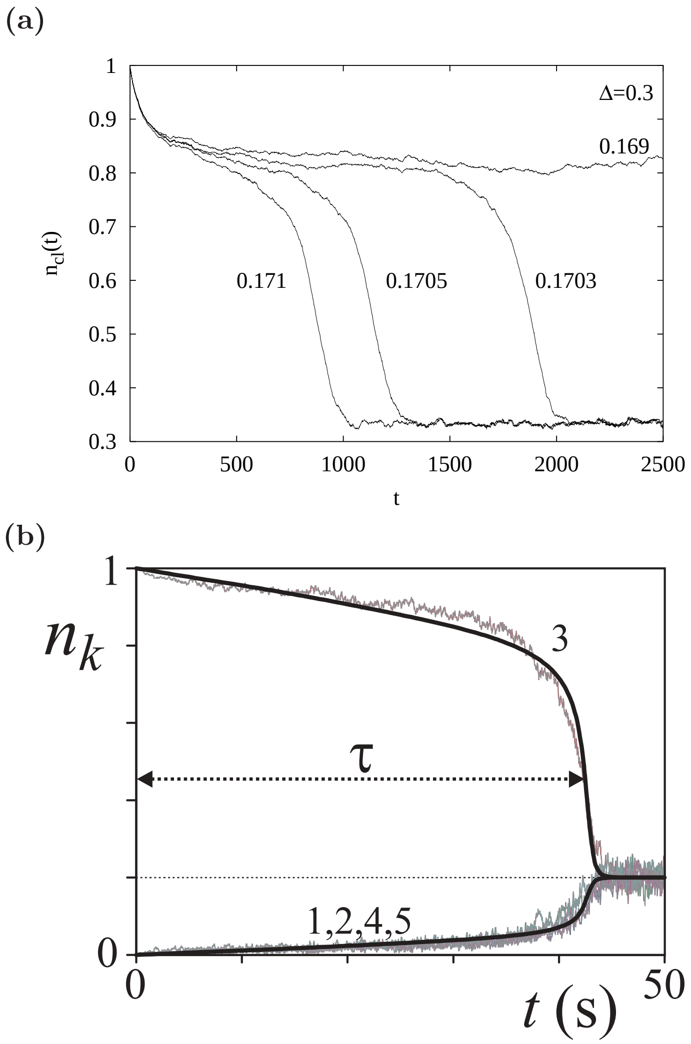

Figure 2.9: (a) Sudden collapse of a cluster in the three urn system. Shown is the time evolution of the cluster fraction $n_{cl}(t)$ (corresponding to the urn initially containing all of the 50,000 particles) for various values of T_0 close to the critical point at $T_{0,c} = 0.169829772$, while $\Delta = 0.3$ is held fixed. The cluster lifetime τ grows as the critical point is approached; beyond this point τ becomes infinite as exemplified by the curve for $T_0 = 0.169$ (i.e, the cluster is stable there). From [20]. (b) The fractions $n_k(t)$, $k = 1, .., 5$ for a five-compartment system at $B = 0.33$, starting out with all the particles in compartment 3. The solid line is calculated from the flux model of equations (2.4),(2.8)-(3.1), and the fluctuating lines are results from molecular dynamics simulations with input parameters corresponding to the actual experiment in Figure 2.6. The cluster collapse occurs at $\tau = 42$ s (from [25]).

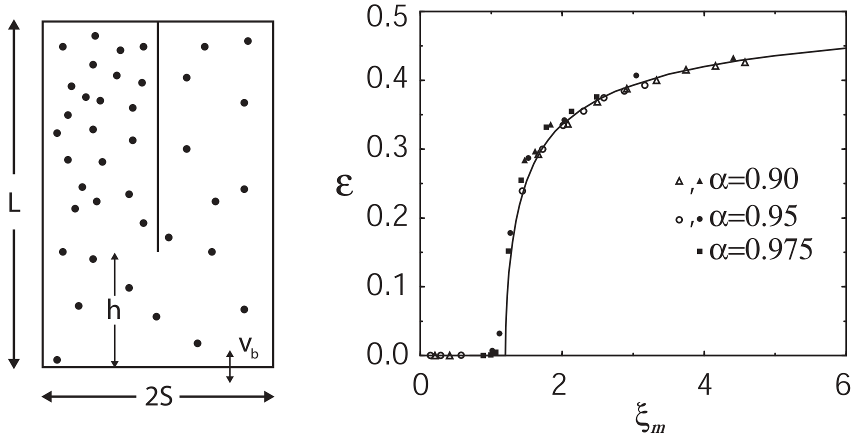

Figure 2.10: (*Left*) Top view of the horizontally vibrated system. The bottom wall is vibrating in a sawtooth manner with very small amplitude. The two compartments are connected by a gap of height h, which is chosen to be considerably larger than the typical mean free path of the particles. (*Right*) Bifurcation diagram showing the asymmetry parameter ϵ as function of the dimensionless parameter ξ_m, which is proportional to the total number of particles N_{tot}. The open symbols are data from molecular dynamics simulations (for a box of dimensions $L = 140d$, $S = 50d$ and $h = 50d$, with d the diameter of the particles), for various values of the restitution coefficient (here denoted by α); the filled symbols are obtained by a direct simulation Monte Carlo method [35]; and the full line is the theoretical prediction from the hydrodynamic model by Brey *et al.* discussed in the text (from [33]).

drodynamic description of a vibrated granular gas [33, 34]. They consider a dilute granular gas confined between a vibrating wall at $x = 0$ and a stationary one at $x = L$, and assume (for each compartment) that there are density gradients only in the x direction. Within this model, the temperature $T(x)$ is a monotonously decreasing function of x, while the pressure $p(x) = p$ is uniform throughout the whole compartment.[§] Its value is found to depend non-monotonically on the number of particles in the compartment (i.e., on

---

[§] There is an interesting difference with the system described by Eggers at this point. The model of Brey *et al.* has a constant pressure p, and a temperature T that decreases with the distance from the vibrating wall. By contrast, in Eggers' model p decreases with the height above the vibrating bottom, while T is constant.

$\xi_{m,k}$):

$$p \propto \frac{2\xi_{m,k} + sinh(2\xi_{m,k})}{cosh^2\xi_{m,k}} \equiv f(\xi_{m,k}) \ , \ k = 1, 2 \ . \tag{2.14}$$

The function $f(\xi)$ (i.e, the number-dependent part of the pressure) is a non-monotonous function just like the flux functions of Eggers, and Lipowski and Droz, with a maximum at $\xi_{m,k} = \xi_0 \approx 1.20$ (the root of $\xi_0 \tanh\xi_0 = 1$). Again, the non-monotonic form is essential for the clustering phenomenon.

For a steady state, the pressures in the two compartments are required to be equal:

$$f(\xi_{m,1}) = f(\xi_{m,2}) \ , \tag{2.15}$$

which may be compared with the analogous condition for the particle fluxes in equation (2.1). For a total particle number such that $\xi_{m,1} + \xi_{m,2} < 2\xi_0$, there is only one solution to the balance equation (2.15), namely the symmetric state $\xi_{m,1} = \xi_{m,2} < \xi_0$, corresponding to a point on the left flank of the function $f(\xi)$.

However, when $\xi_{m,1} + \xi_{m,2} > 2\xi_0$, apart from the symmetric state (which now corresponds to a point on the right-hand flank of $f(\xi)$), also an asymmetric solution $\xi_{m,1} \neq \xi_{m,2}$ comes into existence, with one point lying to the left of ξ_0 and the other one to the right. This yields the theoretical curve in the bifurcation diagram of Figure 2.10 (right). The asymmetry of the two populations, as measured by ϵ, is seen to grow very fast indeed as the total number of particles is increased beyond the critical value.

Just above the critical point, Brey *et al.* checked that the asymmetric solutions are described by $\epsilon = \pm 0.31(\xi_m - \xi_0)^{1/2}$, indicating again (just as in the models of the previous sections) a critical behavior with the standard exponent $\beta = 1/2$ for second order phase transitions.

As a final observation, in the limit for large particle numbers ($\xi \to \infty$) the function $f(\xi)$ takes on the value 2, and the equal-pressure point on the left flank of the function lies at $\xi = 0.63923$, corresponding to a certain small number of particles. Any further increase of N_{tot} is then absorbed by the dense compartment, while the particle number in the dilute compartment remains constant at its fixed value. Naturally, this picture ultimately breaks down when the particle number becomes so large that the dilute-gas approximation is no longer valid and excluded volume effects start to play an important role.

2.7 Double well model

In this section we briefly touch upon an interesting idea put forward by Cecconi *et al.* [36], who portray the Maxwell Demon experiment as an escape problem, in the spirit of the Kramers model for reactions occurring via thermally activated barrier crossing [37, 38]. The two compartments are modelled as a double-well potential $U(x) = -ax^2 + bx^4/4$, in which two particles are moving, driven by a stochastic heat bath and colliding inelastically.

In the noninteracting case, without collisions, a particle is known to spend an average time $\tau \propto \exp(\Delta U/k_B T_b)$ in a well before it escapes to the other one, where ΔU is the height of the potential barrier it has to overcome, and T_b the temperature of the heat bath. The Boltzmann constant k_B is in the present context set equal to unity.

A similar expression for the escape time can be derived for the interacting case, with both ΔU and the granular temperature modified to take into account the particle interaction. Two different situations have to be distinguished: (1) the uniform state with one particle in each well, with escape time τ_1, and (2) the clustered state with both particles occupying the same well, with escape time τ_2. The two escape times can be written as [36]:

$$\tau_n \approx \exp\left(\frac{W_n}{T_n}\right) \quad , \quad n = 1, 2 \quad . \tag{2.16}$$

The barrier height for single occupation of a well is unaltered, $W_1 = \Delta U$, but in the case of double occupation it is reduced to $W_2 = \Delta U - \delta U < \Delta U$ due to the excluded volume effect of the two particles. This acts effectively as a repulsive force.

Similarly, the effective temperature T_1 for a singly occupied well is still nearly equal to T_b, but the temperature T_2 for double occupation is considerably smaller, due to the cooling effect of the inelastic particle collisions [36]. The reduction factor depends on the value of the restitution coefficient, and for a typical value $e = 0.90$ the ratio T_2/T_b is already found to be as low as 0.73. The inelastic collisions effectively act as an attractive force between the particles.

Thus, the excluded volume effect and the inelasticity are two competing effects, the competition of which can be tuned by varying either the heat bath temperature T_b or the restitution coefficient e.

If one increases T_b, keeping all other parameters fixed, both escape times τ_1 and τ_2 naturally decrease (following a linear behavior in an Arrhenius plot of $\log\tau_n$ vs. $1/T_b$ [36]) but they do so at different rates. For high values of

T_b (corresponding to vigorous shaking in the Maxwell Demon experiment) it is found that $\tau_1 > \tau_2$, meaning that the system spends most of the time in the uniform state 1. However, when T_b is decreased below a certain critical value, the situation is reversed and τ_2 becomes larger than τ_1. This heralds the transition to the clustered regime, since now the particles spend most of the time in the clustered state 2.

Also here the clustering can be related to a non-monotonicity in the behavior of the flux $F(n)$ from a well, with $n = 1, 2$ the number of particles in the well. Recognizing that $F(n) \propto \tau_n^{-1}$, the flux for high T_b (when no clustering occurs) is an *increasing* function of n, whereas for low T_b (in the clustered regime) it *decreases* with n. A further bridge between the flux model and the stochastic heat bath description is given in reference [39].

The double well system exhibits, apart from the clustering effect, also another intriguing phenomenon that we want to mention: At low temperature T_b and strong inelasticity, the two particles tend to synchronize their jumps from one well to the other. That is, the relative motion of the two particles becomes frozen out due to the repeated collisions, and together they behave as a two-particle “molecule” [36].

2.8 Further directions

There are many interesting generalizations and applications of the Maxwell demon experiment. For example, with an eye to practical applications, where granular materials are rarely mono-disperse, one may replace the identical particles of the original experiment by a mixtures of different particles. In a two-compartment system filled with a bidisperse granular gas consisting of large and small particles of the same material, we find the clustering to be competitive: Depending on the shaking strength, the clustering can be directed either towards the compartment initially containing the majority of the *large* particles, or to the one containing mainly *small* particles. The experimental observations are quantitatively explained by a bidisperse extension of the Eggers flux model. This behavior is described in Chapter 4.

In the same context, Barrat and Trizac [40] describe molecular dynamics simulations on a bidisperse extension of the horizontally vibrated system discussed in section 2.6. The granular mixture in this case consists of heavy and light particles (of equal size but different mass density), with an equal number of each species. As in the monodisperse system of Brey *et al.* [33], the clustering transition is triggered by increasing the total particle number.

It is found that the clustering of the heavier particles is considerably more complete than that of the lighter ones, since the latter are more mobile.

The clustering effect can also be employed to generate spontaneous *directed transport*, as was recently shown by van der Meer *et al.* in two different compartmentalized systems [41]. The first system is the so-called "granular fountain", which is created via a simple modification to the original Maxwell Demon setup depicted in Figure 2.2: A small hole is drilled, close to the bottom, in the wall between the compartments. As a result, in the clustered situation a net flow of particles goes through this hole back into the dilute compartment; and each particle that enters the dilute compartment soon picks up sufficient kinetic energy to jump over the wall again. This leads to a stable convection roll, with an upward particle flow in the dilute (hot) compartment and a downward flow in the dense (cold) one. In [41] this system is studied experimentally, numerically, and theoretically, and all observed phenomena are well reproduced by an adapted version of Eggers' flux model.

The second, related system is the "granular ratchet". This is a cyclic array of K compartments connected alternatingly by walls of a certain height h (over which the particles can jump) and very high walls, extending to the top lid of the setup, with a small hole near the bottom. The transport in this system takes the form of a net particle current, in either the clockwise or counterclockwise direction, arising spontaneously as a result of the granular clustering effect [41].

Finally, we want to mention the close analogy between granular clustering and the traffic jam problem [42–44]. If one divides the highway in cells of say 500 m (which in large parts of the Dutch highway network has actually been realized via induction loops in the asphalt, which permanently monitor the traffic) and considers the density ρ_k of cars in these cells, the traffic flow from one cell to the next can be described by a flux function $F(\rho_k)$. This function is in fact one of the basic notions in traffic analysis, known as the "fundamental diagram", and has been measured innumerable times in real life [45, 46]: Just as the flux functions in Figure 2.3, $F(\rho_k)$ shows a non-monotonic dependence on ρ_k. At low densities the cars flow freely from cell to cell and $F(\rho_k)$ increases with ρ_k, whereas at densities above 30 vehicles/km/lane the cars start to interact (braking, passing, and other manoeuvres all reduce the forward velocity) and $F(\rho_k)$ decreases. Even though the precise behavior of $F(\rho_k)$ in the congested regime needs further clarification, since the traffic data here do not follow a one-dimensional curve but instead are scattered over a two-dimensional region in the (F, ρ)-plane [47, 48], the fundamental diagram approach with a one-humped function has already proven to be able to give an adequate description of traffic jam formation on the highway. Recent reviews on this highly relevant application of the Maxwell Demon effect can be found in references [45, 46].

References

[1] H.M. Jaeger, S.R. Nagel, and R.P. Behringer, *Granular solids, liquids, and gases*, Rev. Mod. Phys. **68**, 1259 (1996).

[2] L.P. Kadanoff, *Built upon sand: Theoretical ideas inspired by granular flows*, Rev. Mod. Phys. **71**, 435 (1999).

[3] I. Goldhirsch, *Rapid granular flows*, Annu. Rev. Fluid Mech. **35**, 297 (2003).

[4] M.A. Hopkins and M.Y. Louge, *Inelastic microstructure in rapid granular flows of smooth disks*, Phys. Fluids A**3**, 47 (1991).

[5] I. Goldhirsch and G. Zanetti, *Clustering instability in dissipative systems*, Phys. Rev. Lett. **70**, 1619 (1993); see also I. Goldhirsch, *Clustering instability in granular gases*, in Proc. DOE/NSF Workshop on Flow of Particulates and Fluids, Worcester MA, October 1991, edited by S.I. Plasynski, W.C. Peters, and M.C. Roco (National Technical Information Service, Springfield, VA, 1991).

[6] Y. Du, H. Li, and L.P. Kadanoff, *Breakdown of hydrodynamics in a one-dimensional system of inelastic particles*, Phys. Rev. Lett. **74**, 1268 (1995).

[7] A. Kudrolli, M. Wolpert, and J.P. Gollub, *Cluster formation due to collisions in granular material*, Phys. Rev. Lett. **78**, 1383 (1997).

[8] J. Duran, Sand, powders, and grains: An introduction to the physics of granular materials (Springer, New York, 2000).

[9] H.J. Schlichting and V. Nordmeier, *Strukturen im Sand*, Math. Naturwiss. Unterr. **49**, 323 (1996).

[10] J. Eggers, *Sand as Maxwell's demon*, Phys. Rev. Lett. **83**, 5322 (1999).

[11] A.S. Leff and A.F. Rex, *Maxwell's Demon: Entropy, Information, Computing* (Adam Hilger, Bristol, 1990).

[12] J.P. Gollub and J.S. Langer, *Pattern formation in nonequilibrium physics*, Rev. Mod. Phys. **71**, S396 (1999).

[13] T. Shinbrot and F.J. Muzzio, *Noise to Order*, Nature **410**, 251 (2001).

[14] E. Bodenschatz, W. Pesch, and G. Ahlers, *Recent developments in Rayleigh-Bénard convection*, Annu. Rev. Fluid Mech. **32**, 709 (2000).

[15] K.H. Andersen, M.-L. Chabanol, and M. van Hecke, *Dynamical models for sand ripples beneath surface waves*, Phys. Rev. E**63**, 066308 (2001); K.H. Andersen, M. Abel, J. Krug, C. Ellegaard, L.R. Søndergaard, and J. Udesen, *Pattern dynamics of vortex ripples in sand: Nonlinear modeling and experimental validation*, Phys. Rev. Lett. **88**, 234302 (2002).

[16] J. T. Jenkins and S. B. Savage, *A theory for the rapid flow of identical, smooth, nearly elastic, spherical particles*, J. Fluid Mech. **130**, 187 (1983); J. T. Jenkins and M. W. Richman, *Boundary conditions for plane flows of smooth, nearly elastic, circular disks*, J. Fluid Mech. **171**, 53 (1986); S. McNamara and S. Luding, *Energy flows in vibrated granular media*, Phys. Rev. E**58**, 813 (1998).

[17] P.M. Chaikin and T.C. Lubensky, *Principles of condensed matter physics* (Cambridge University Press, Cambridge, 1995).

[18] K. van der Weele, D. van der Meer, M. Versluis, and D. Lohse, *Hysteretic clustering in granular gas*, Europhys. Lett. **53**, 328 (2001).

[19] D. van der Meer, K. van der Weele, and D. Lohse, *Bifurcation diagram for compartmentalized granular gases*, Phys. Rev. E**63**, 061304 (2001).

[20] F. Coppex, M. Droz, and A. Lipowski, *Dynamics of the breakdown of granular clusters*, Phys. Rev. E **66**, 011305 (2002).

[21] F.Y. Wu, *The Potts model*, Rev. Mod. Phys. **54**, 235 (1982).

[22] U. Marini Bettolo Marconi and M. Conti, *Dynamics of vibrofluidized granular gases in periodic structures*, Phys. Rev. E**69**, 011302 (2004).

[23] D. van der Meer, K. van der Weele, and D. Lohse, *Coarsening dynamics in a vibrofluidized compartmentalized granular gas*, JSTAT **1**, P04004 (2004).

[24] D. van der Meer, K. van der Weele, and D. Lohse, *Sudden collapse of a granular cluster*, Phys. Rev. Lett. **88**, 174302 (2002).

[25] D. van der Meer and K. van der Weele, *Breakdown of a near-stable granular cluster*, Prog. Theor. Phys. Suppl. **150**, 297-312 (2003).

[26] K. van der Weele, D. van der Meer, and D. Lohse, *Birth and sudden death of a granular cluster*, in "Advances in Solid State Physics **42**", edited by B. Kramer, Proc. DPG Spring Meeting 2002 in Regensburg, Germany (Springer, Berlin, 2002) 371.

[27] K. van der Weele, D. van der Meer, and D. Lohse, *Maxwell's demon in a granular gas*, in "Order and Chaos **8**", edited by T. Bountis and Sp. Pnevmatikos, Proc. 14th Summerschool on Nonlinear Dynamics, Chaos, and Complexity, July-August 2001, Patras, Greece (K. Sfakianakis Publ., Thessaloniki, 2003) 239.

[28] A. Lipowski and M. Droz, *Urn model of separation of sand*, Phys. Rev. E**65**, 031307 (2002).

[29] P. Ehrenfest and T. Ehrenfest, *The Conceptual Foundations of the Statistical Approach to Mechanics* (Dover, New York, 1990).

[30] I. Bena, F. Coppex, M. Droz, and A. Lipowski, *Yang-Lee zeros for an urn model for the separation of sand*, Phys. Rev. Lett. **91**, 160602 (2003).

[31] A. Lipowski and M. Droz, *Moment ratios for an urn model of sand compartmentalization*, Phys. Rev. E**66**, 016118 (2002).

[32] G.M. Shim, B.Y. Park, and H. Lee, *Analytic study of the urn model for separation of sand*, Phys. Rev. E**67**, 011301 (2003).

[33] J. J. Brey, F. Moreno, R. García-Rojo, and M. J. Ruiz-Montero, *Hydrodynamic Maxwell demon in granular systems*, Phys. Rev. E**65**, 011305 (2001).

[34] J.J. Brey, M.J. Ruiz-Montero, and F. Moreno, *Boundary conditions and normal state for a vibrated granular fluid*, Phys. Rev. E**62**, 5339 (2000).

[35] G. Bird, *Molecular Gas Dynamics and the Direct Simulation of Gas Flows* (Clarendon Press, Oxford, 1994).

[36] F. Cecconi, A. Puglisi, U. Marini Bettolo Marconi, A. Vulpiani, *Noise activated granular dynamics*, Phys. Rev. Lett. **90**, 064301 (2003).

[37] H.A. Kramers, *Brownian motion in a field of force and the diffusion model of chemical reactions*, Physica **7**, 284 (1940).

[38] P. Hänggi, P. Talkner, and M. Borkovec, *Reaction-rate theory: fifty years after Kramers*, Rev. Mod. Phys. **62**, 251 (1990).

[39] U. Marini Bettolo Marconi and A. Puglisi, *Statistical mechanics of granular gases in compartmentalized systems*, Phys. Rev. E**68**, 031306 (2003).

[40] A. Barrat and E. Trizac, *A molecular dynamics 'Maxwell Demon' experiment for granular mixtures*, Molecular Physics **101**, 1713 (2003).

[41] D. van der Meer, P. Reimann, K. van der Weele, and D. Lohse, *Spontaneous ratchet effect in a granular gas*, Phys. Rev. Lett. **92**, 184301 (2004).

[42] O. Biham, A.A. Middleton, and D. Levine, *Self-organization and a dynamical transition in traffic-flow models*, Phys. Rev. A**46**, R6124 (1992).

[43] B.S. Kerner and P. Konhäuser, *Cluster effect in initially homogeneous traffic flow*, Phys. Rev. E**48**, R2335 (1993); *Structure and parameters of clusters in traffic flow*, Phys. Rev. E**50**, 54 (1994).

[44] E. Ben-Naim, P.L. Krapivsky, and S. Redner, *Kinetics of clustering in traffic flow*, Phys. Rev. E**50**, 822 (1994).

[45] D. Chowdhury, L. Santen, and A. Schadschneider, *Statistical physics of vehicular traffic and some related systems*, Phys. Rep. **329**, 199 (2000).

[46] D. Helbing, *Traffic and related self-driven many-particle systems*, Rev. Mod. Phys. **73**, 1067 (2001).

[47] B.S. Kerner, S.L. Klenov, and D.E. Wolf, *Cellular automata approach to three-phase traffic theory*, J. Phys. A: Math. Gen. **35**, 9971 (2002).

[48] K. van der Weele, W. Spit, T. Mekkes, and D. van der Meer, *From granular flux model to traffic flow description*, in “Traffic and Granular Flow '03”, S. Hoogendoorn, S. Luding, and D.E. Wolf (Eds.) (Springer, Berlin, 2004).

Chapter 3

Small-number statistics near the clustering transition in a compartmentalized granular gas [§]

Abstract

Statistical fluctuations are observed to profoundly influence the clustering behavior of granular material in a vibrated system consisting of two connected compartments. When the number of particles N is sufficiently large ($N \approx 300$ is sufficient), the clustering follows the lines of a standard second-order phase transition and a mean-field description works. For smaller N, however, the enhanced influence of statistical fluctuations breaks the mean-field behavior. We quantitatively describe the competition between fluctuations and mean-field behavior (as function of N) using a dynamical flux model and Molecular Dynamics simulations.

3.1 Introduction

As discussed in the previous chapter, clustering is one of the most characteristic features of granular gases. For systems divided into two equally sized compartments separated by a wall of finite height [1–5], a quantitative model

---

[§] Adapted from: René Mikkelsen, Ko van der Weele, Devaraj van der Meer, Martin van Hecke, and Detlef Lohse, *Small-Number Statistics near the Clustering Transition in a Compartmentalized Granular Gas*, submitted to Phys. Rev. E (2004).

for the clustering was derived by Eggers [2], based on a statistical description of the energy budget within the gas. Central in this model is a flux function, which represents the flow of particles between the compartments: The flux out of compartment i ($i = 1, 2$), containing a fraction n_i of the total number of particles in the system, is given by the function $F(n_i)$. The dynamics of the model is then governed by the following balance equation [2, 3]:

$$\frac{dn_1}{dt} = -F(n_1) + F(n_2) + \xi_1 \ , \tag{3.1}$$

i.e., the change in the particle fraction in compartment 1 is equal to the mean flux it receives from compartment 2 ($F(n_2)$), minus the mean flux leaving compartment 1 ($F(n_1)$). The last term ξ_1 is the noise term, which is generally assumed to be Gaussian and white [2, 6, 7].

Due to particle conservation ($n_1 + n_2 = 1$) the dynamics given by equation (3.1) can be rewritten as

$$\frac{dn_1}{dt} = G(n_1) + \xi_1 \ , \tag{3.2}$$

where $G(n_1) = -F(n_1) + F(1 - n_1)$ is the net mean flux out of compartment 1. So far the focus has been on systems containing a large number of particles, for which the statistical noise constitutes only a relatively small perturbation to the mean-field behavior governed by $G(n_1)$. For such systems, the Eggers flux model has proven to describe the clustering transition very well, not only for a two compartment system, but also for the generalized case of $k > 2$ connected compartments [3–5]. In this chapter, however, we will reduce the particle number to such an extent that the influence of the noise term becomes comparable to (or even stronger than) the mean-field behavior. Thus we witness how the mean-field phase transition gives way to its noise-dominated counterpart. At sufficiently high noise rates (i.e., small particle number N) the transition is completely wiped out and no clustering occurs anymore.

The compartmentalized gas at hand (like many other granular systems) is inherently noisy, owing to the fact that it contains *much* less particles than the typical 10^{23} from textbook statistical physics. This makes it a very natural and suitable system to study the influence of statistical fluctuations [8–10].

We will study the granular gas by means of molecular dynamics (MD) simulations. To connect the MD data to the dynamical model, we introduce a discrete time version of equation (3.2), with dt being taken equal to the period T of the shaking, which is also defined as the unit of time ($dt = T = 1$):

$$n_i(t+1) = n_i(t) + [M(n_i(t)) + \xi(n_i(t))] \ . \tag{3.3}$$

The notation $M(n_i(t))$, instead of $G(n_i(t))$, is adopted to stress the fact that we are now dealing with a discrete time mapping. To obtain M and ξ from the MD simulations, one simply counts the number of particles that changes compartment during one complete shaking cycle: the average corresponds to M (which may be directly compared with the net flux $F(n_i)$ according to Eggers' theory), and the fluctuations define ξ. We will in particular study the case of small total particle number N, down to N=50. The dynamics given by equation (3.3) has the advantage over equation (3.2) that it is easier to implement the constraint on n_i to take on only positive integer values, and it more naturally captures the small-number noise.

Moreover, since in the present context the number of particles is a crucial parameter, we will work mostly with the actual particle numbers N_i (with $N_1 + N_2 = N$) instead of the particle fractions n_i, which conceal the actual numbers. Of course, the two notations can be translated into one another via $n_i = N_i/N$.

This chapter is constructed as follows: Section 3.2 gives the MD results for the different (uniform and clustered) shaking regimes and describes how the nature of the clustering transition changes for decreasing particle number N. In Section 3.3 the mapping equation (3.3) is reconstructed from the MD data, i.e., both the mean-field term M and the fluctuation term ξ. In Section 3.4 we introduce a potential related to M, which enables a direct comparison between the strengths of M and ξ. In Section 3.5 we then describe the time correlations in the signal $n_i(t)$, one of the key indicators of a critical point in the theory of phase transitions, and used here to illustrate the breakdown of the mean-field behavior for small N. Finally, Section 3.6 contains concluding remarks.

3.2 MD simulations

3.2.1 Numerical scheme

The molecular dynamics (MD) simulations are based on a code that updates the particle and bottom positions every 10^{-5} seconds. Between collisions, the particles move freely, describing parabolic paths under the influence of gravity. Whenever a particle-particle or particle-wall collision takes place, signalled by a spatial overlap, the velocity vector of the involved particles after collision is computed from the vector before collision according to Newton's laws.

The simulated system consists of two connected rectangular compartments of size 2.45 cm × 4.90 cm, separated from each other along their longest side by a 3 cm high wall. A total number of N particles is distributed over the two compartments and given a random initial velocity following a normal distribution. The particles are chosen to be smooth (no friction) and hard (no deformation) with radius r=1.25 mm and are taken to be made of steel, having mass $m = 0.0625$ g and coefficient of restitution $e_{particles} = 0.85$. The particle positions are sampled every 0.01 seconds. The code gives information not only on the change in the particle distribution, but also on how many particles have changed compartment from $1 \rightarrow 2$ and $2 \rightarrow 1$. As a result, not only the net particle flux ($G(N_1)$), but also the individual fluxes from compartment 1 ($F(N_1)$) and 2 ($F(N_2)$) are obtained.

The side walls enclosing the setup are taken to be infinitely high, so the system has no upper boundary. All walls, including the bottom, are assigned a coefficient of normal restitution equal to that of glass, $e_{wall} = 0.95$.

Energy is injected into the system by means of a sinusoidally vibrating bottom with adjustable frequency and amplitude. For simplicity, the amplitude is fixed at a=1 mm in all simulations presented in this chapter, such that the frequency is the only control parameter by which we tune the shaking strength.

3.2.2 Time evolution and Probability Distribution Functions

The MD results give a very clear picture of the main phenomenology around the clustering transition. In Figure 3.1 (left column) we see how the number of particles evolves in the left compartment as a function of time, for three different frequencies around the critical one. These simulations were done for $N = 300$ particles, starting out from the symmetric distribution with ($N_1(0) = N_2(0) = 150$). The particle distribution was sampled at 100 Hz, and each picture depicts 10^5 samples (10^3 seconds) in the steady state.

These and similar time series yield the probability distribution function (PDF) shown in the right column of Figure 3.1, representing the probability of finding a given number of particles within a compartment. In creating the PDFs the particle numbers for both compartments are used, therefore these are always symmetric around $N/2$ due to particle conservation. The maximum value of the PDF gives the most probable particle distribution and the width of the peaks around the maximum value is a measure of the magnitude of the fluctuations. The first 10^4 samples (10^2 s) are omitted, in

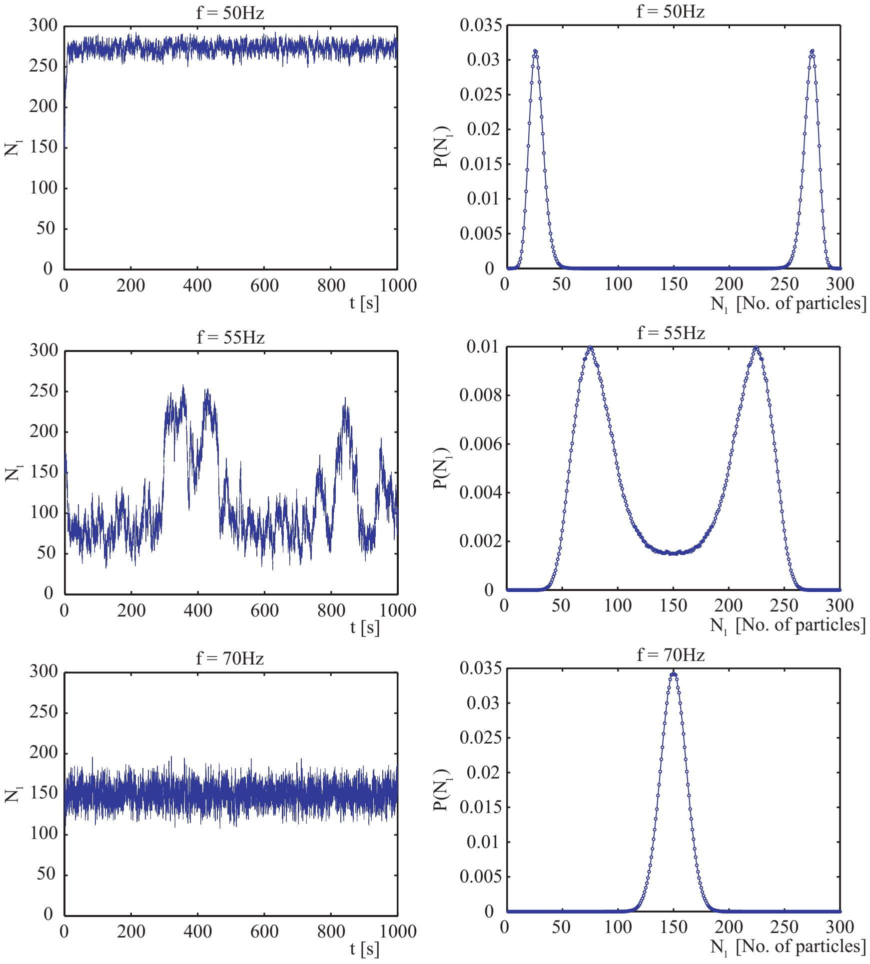

Figure 3.1: Molecular dynamics simulations for $N = 300$ particles. Left column: Time evolution of the number of particles in the left compartment $[N_1(t)]$ starting from the symmetric distribution $N_1(0) = N_2(0) = N/2 = 150$. Right column: Probability distribution function (PDF) showing the statistical distribution of the particles over the two compartments. Three different regimes are distinguished, depending on the shaking strength: (I) At mild shaking (top row, f=50Hz), the particles cluster in one of the two compartments. (II) At intermediate shaking strength (middle row, f=55Hz), they still tend to cluster, but the system is intermittently driven out of this state by the statistical fluctuations. (III) For strong shaking (bottom row, f=70Hz), the system is fluctuating around the symmetric distribution.

order to avoid initial transients, using the next 10^6 samples (10^4 s) for the determination of the PDFs.

Let us first consider the shaking frequency $f = 50$ Hz (Figure 3.1, top). The initial symmetric distribution is highly unstable and the particles rapidly cluster into one of the two compartments. The clustered state at $N_1 \approx 270$ is stable and the particle distribution will fluctuate around this value as the shaking is continued. This behavior is reflected in the PDF which has two separate peaks corresponding to the two clustered states, with $N_1 > N_2$ (cluster in left compartment, depicted in the time series plot) and $N_1 < N_2$ (cluster in right compartment) respectively. The maximum and mean value of the peaks are not located at precisely the same position, as the peaks are skewed slightly towards the center $N/2$.

Increasing the shaking strength to $f = 55$ Hz shows a change in the behavior of the particle distribution (Figure 3.1, middle). The unclustered state still is unstable and the particles rapidly begin to cluster into one of the compartments. However, due to the increased shaking strength (and the fact that the clustered state lies closer to the symmetric state than before) the fluctuations are strong enough to take the system out of this situation and towards the unclustered state again. Since this is unstable, the system quickly evolves back into either one of the two clustered states, giving rise to the intermittent behavior seen in the time series. Looking at the corresponding PDF, two distinct peaks are still present, but they are now connected, in agreement with the observation that the system spends some considerable time in the neighborhood of the unclustered state. The fact that the two peaks have moved closer together illustrates the decreased asymmetry of the clustered state, and their broadening reflects the stronger fluctuations.

For strong shaking, $f = 70$ Hz, the only stable configuration is the unclustered state (Figure 3.1, bottom). Here the energy input into the system (via the vibrating bottom) overpowers the energy dissipation (via the inelastic collisions) and no clustering occurs. Hence the particle distribution is seen to fluctuate around the unclustered state. The PDF reduces to a single peak, taking the shape of a Gaussian distribution around the unclustered state. Note that the peak is narrower than those for $f = 55$ Hz (middle plot): the influence of the fluctuations has decreased again.

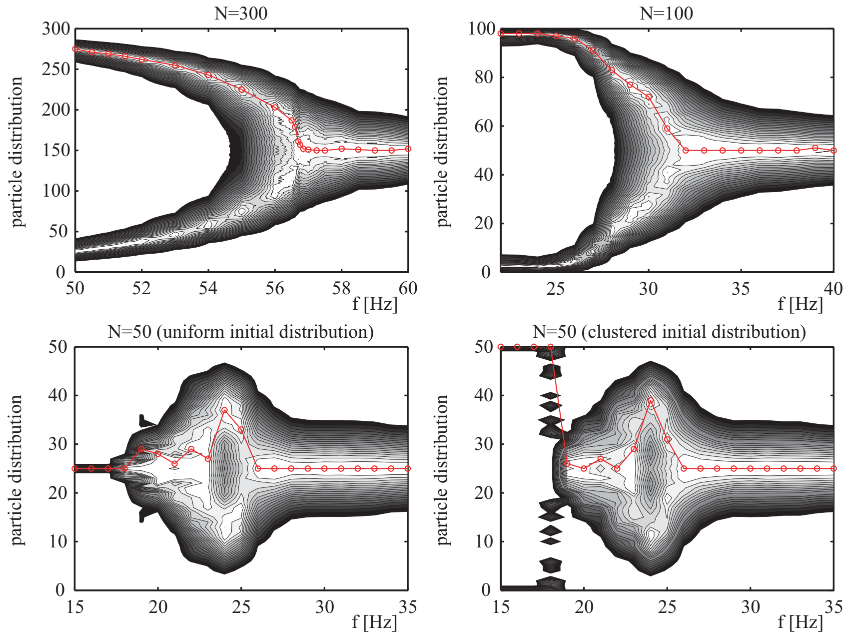

Figure 3.2: The clustering transition for three different particle numbers: N=300 (top left), N=100 (top right), and N=50 particles (bottom left [starting with both compartments equally filled] and right [starting from a clustered state]). The contours give the probability. These diagrams are constructed from the PDFs (cf. Figure 3.1) for a range of shaking frequencies f around the critical value f_c; the PDFs of Figure 3.1 are vertical cuts through this figure. The circles represent the maximum of the PDF at each measured frequency. For N=300 the diagram has all the characteristics of a standard second-order phase transition: a pitchfork bifurcation with its branches opening as $(f_c - f)^{\beta}$, with the mean-field critical exponent $\beta = \frac{1}{2}$. For N=100 the branches do not follow this power-law anymore due to the increased influence of statistical fluctuations, and for N=50 even the branches themselves have deteriorated.

3.2.3 The clustering transition for varying total particle number N

The PDFs obtained for a range of frequencies around the critical value f_c can be used to construct the bifurcation diagrams of Figure 3.2. Here we see how the PDF evolves as function of f for three different particle numbers: N=300 (top left), N=100 (top right), and N=50 (bottom left and right). The magnitude of the PDF is indicated by the gray-scale, with black corresponding to a low probability ($0.1 < p/p_{max} \leq 0.15$) and white to the highest ($0.95 < p/p_{max} \leq 1$). The gray backbone curve locates the maximum of the PDF ($p_{max}(f)$), and the width of the gray-scale area around this curve is directly related to the amplitude of the fluctuations.

For N=300 particles the transition between the unclustered and clustered states resembles that of second-order phase transitions known from equilibrium statistical physics, with a characteristic pitchfork bifurcation, branching off as $(f_c - f)^\beta$, where $\beta = \frac{1}{2}$ is the standard mean-field critical exponent [11]. When the critical frequency ($f = f_c \approx 56.7$ Hz) is approached from above, the fluctuations around the (stable) symmetric state grow. Below the critical point ($f < f_c$) the symmetric state is unstable, and it has given way to two asymmetric distributions, one with $N_1 > N_2$ (cluster in the left compartment) and one with $N_1 < N_2$ (cluster in right compartment). These distributions become more asymmetric as f is lowered further away from the critical point f_c, while the fluctuations around the equilibrium decrease. All in all, in this case with relatively many particles the clustering transition is very similar to that predicted by the Eggers model with zero noise [2]. Together with experimental results [3], these MD simulations further validate the Eggers model and its ability to capture the many-particle (mean-field) transition.

Reducing the number of particles in the system causes a change in the transition, since the fluctuations become so strong that they destroy the mean-field characteristics. For N=100 particles (Figure 3.2, top right) the bifurcation branches are already no longer following the standard square root behavior. Just below $f_c \approx 32$ Hz they stay somewhat closer to the symmetric state, owing to the fact that the fluctuations cause the system to switch intermittently from one clustered state to the other, and in doing so forces it to spend some time in the unstable symmetric state as well (cf. the time series in Figure 3.1, middle left).

On the other hand, far away from the critical point the clustering is very pronounced, even more so than in the case of $N = 300$ particles. This is due to the small shaking strength here, which leads to an enhanced clustering [2, 3].

The breakdown of the mean-field behavior becomes even more evident for N=50 (Figure 3.2, bottom left). At shaking frequencies above $f_c \approx 26$ Hz, the symmetric state is stable. Upon decreasing the driving frequency below f_c, the particles attempt to cluster in one of the compartments – with many intermittent switches from one compartment to the other – but the branches do not manage to form a fork anymore. In fact, a further decrease of f makes the shaking strength so small that the particles (starting from the symmetric distribution with 25 particles in each compartment) are not able to overcome the separating wall anymore and they are frozen in the initial state. This also explains the vanishing fluctuations for $f \leq 17$ Hz.

If alternatively we start out from the clustered state (with all 50 particles in the left compartment) we get the transition diagram of Figure 3.2, bottom right. Up to $f = 18$ Hz the particles remain frozen in the clustered configuration, followed by a regime where half-grown clusters are intermittently switching from one compartment to the other (19 Hz $\leq f \leq$ 25 Hz), until finally the symmetric distribution becomes stable at $f_c \approx 26$ Hz.

3.3 Construction of the map

3.3.1 Flux function

We will now proceed to reconstruct the flux function from the MD data, i.e., the outflow of particles from a compartment as function of its particle content. In contrast to the simulations used to create the time series in Figure 3.1, where the particles initially were distributed equally over the two compartments followed by simulating for a long time, this time we sweep through different initial distributions, in order to get sufficient statistics also for the improbable states. The sampling interval is synchronized to the frequency of the shaking, in order to obtain the outflow of particles during one complete shaking cycle, and hence the discrete time map of equation (3.3).

We checked that the outflow of particles after a shaking cycle is uncorrelated to the outflow in the previous stroke. The particle outflow is therefore a Markovian process [9], only depending on the number of particles in the compartment at the start of the shaking cycle (and not on previous particle numbers at earlier strokes), justifying the form of the mapping in equation (3.3).

For every initial distribution, 20 pre-strokes are carried out with an infinitely high wall separating the compartments, enabling the particles within

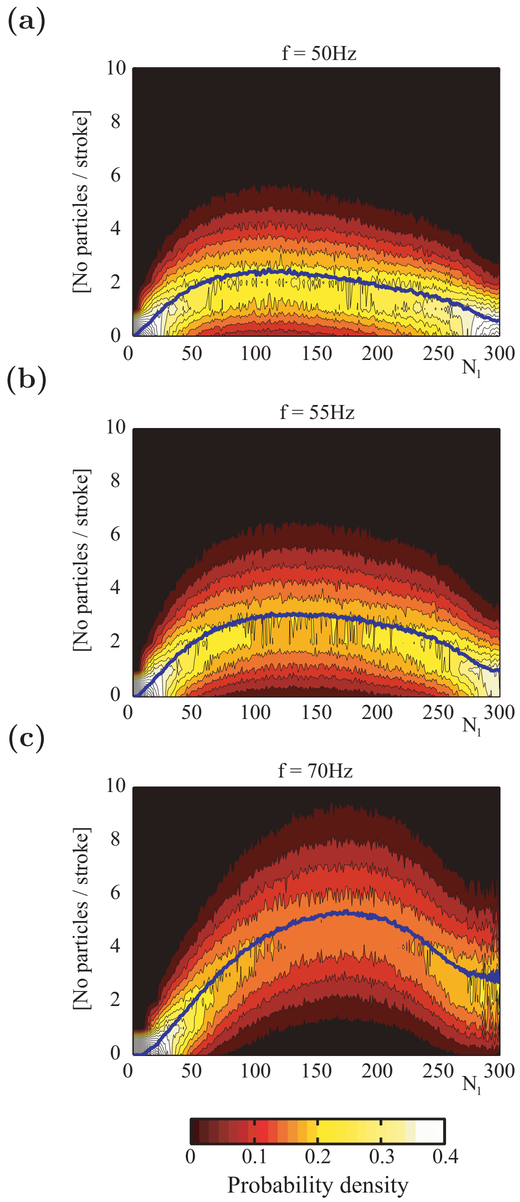

Figure 3.3: Contour plots showing the probability density of having a given outflow of particles from a compartment as a function of the number of particles N_1 in the compartment, for f=50Hz (a), f=55Hz (b) and f=70Hz (c), all at driving amplitude a=1mm. The probability density has been normalized to 1 for each value of N_1 (integrating along a vertical line in the figure) and its value can be read off from the color bar. The thick, gray backbone line corresponds to the averaged particle flux $F(N_1)$, which can slightly differ from the most probable flux. The plots are based on MD simulations during 20,000 driving strokes.

each compartment to equilibrate. The wall is then abruptly reduced to 3 cm, after which 20 more strokes are carried out. The results from these last 20 strokes are used to determine the outflow shown in Figure 3.3. This procedure is repeated 1000 times for different initial conditions to get good statistics.

Figure 3.3, for $N = 300$ particles, contains the results for f=50 Hz (a), f=55 Hz (b), and f=70 Hz (c). As expected the outflow is seen to increase with the shaking strength. The gray scale indicates how probable a given outflow is for a compartment containing N_i particles ($i = 1, 2$). The thick, solid line corresponds to the average outflow of particles, which is the MD analogue of the Eggers flux function $F(N_i)$ with zero noise. Just as predicted by Eggers' theory, the average outflow is a one-humped function of N_i, which is indeed an essential prerequisite for the clustering phenomenon to occur [2]. However, where the theoretical Eggers function has the form $F(N_i) \propto N_i^2 \exp(-BN_i^2)$, the reconstructed flux function starts out from $N_i = 0$ with a power smaller than quadratic. This can be traced back to the fact that in the Eggers theory the dissipation was taken to result from the binary collisions between the particles only (the frequency of which grows as N_i^2), whereas in reality also the collisions of the particles with the walls (linear in N_i) contribute [12]. At low densities ($N_i \to 0$) the particle-wall collisions even become the dominant source of dissipation.

A dynamical equilibrium between the compartments (not necessarily stable) is obtained when the average flux of particles going from 1 → 2 is balanced by the flux in the opposite direction 2 → 1. In Figure 3.4 we therefore plot the averaged flux of particles leaving compartment 1 (black curve, starting out from zero at $N_1 = 0$) together with the flux from compartment 2 (gray curve, starting out from zero at $N_1 = 300$, i.e., $N_2 = 0$): We do so for f=50 Hz (a), f=55 Hz (b), and f=70 Hz (c). Where the two curves intersect the total flux vanishes and the system is in equilibrium.

In the first plot (f=50 Hz) *three* equilibrium points can be discerned, corresponding to the (unstable) symmetric distribution $\{N_1 = N_2 = 150\}$ and the two stable clustered states $\{N_1 \approx 25, N_2 \approx 275\}$ and $\{N_1 \approx 275, N_2 \approx 25\}$. The second plot ($f$=55 Hz) is close to the critical frequency and the three equilibria are on the verge of merging into one, i.e, into the symmetric distribution. In the third plot (f=70 Hz) the symmetric equilibrium is the only one left and has become stable in the process.

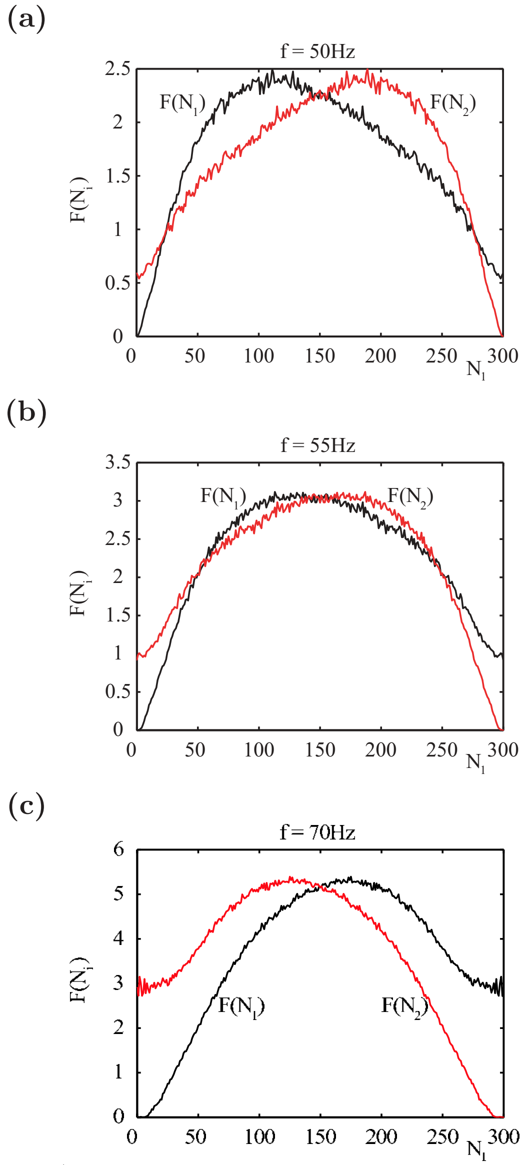

Figure 3.4: The averaged fluxes $F(N_1)$ (black) and $F(N_2)$ (gray) in a two-compartment system, obtained from MD simulations for f=50Hz (a), f=55Hz (b) and f=70Hz (c) with a=1mm. Where the two curves intersect, the flux of particles out of compartment 1 (black, starting out from zero at $N_1 = 0$) is balanced by the particles it receives from compartment 2 (gray, starting out from zero at $N_1 = 300$, i.e., $N_2 = 0$).

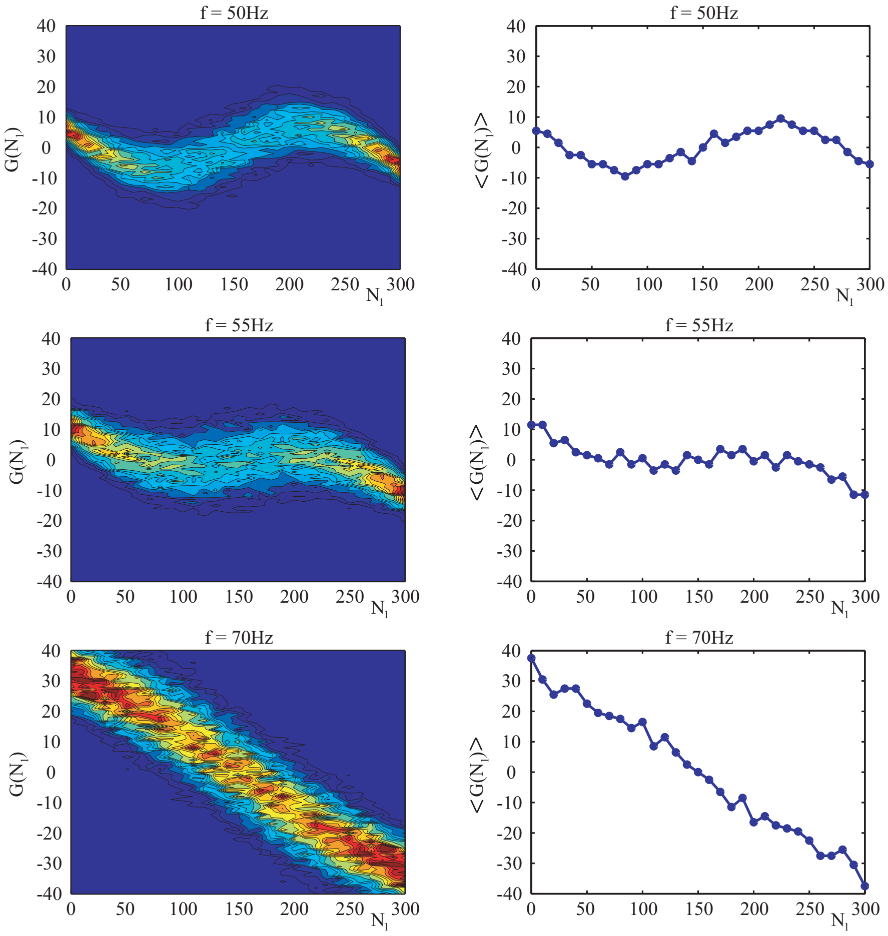

Figure 3.5: The net flux $G(N) = -F(N_1) + F(N_2)$ (left column) and its average $\langle G(N)\rangle = \langle -F(N_1) + F(N_2)\rangle$ (right column) obtained from MD simulations for f=50Hz (top row) , f=55Hz (middle row) and f=70Hz (bottom row). The amplitude of the driving is a=1mm.

3.3.2 Stochastic map

In any equilibrium state the net flux $G(N_1) = -F(N_1)+F(N_2)$ is zero. This quantity is shown in Figure 3.5 for the same three frequencies as in Figures 3.3 and 3.4. The left column shows the net flux and the right column the averaged function $\langle G(N)\rangle = \langle -F(N_1) + F(N_2)\rangle$. Since we have sampled the flux per stroke of the driving, this averaged net flux is precisely the mean-field term of the mapping introduced in equation (3.3):

$$\langle G(N_i)\rangle = M(N_i) \ . \tag{3.4}$$

The form of $M(N_i)$ does not only give information about the position of the equilibrium states, but also about their stability. In the clustered regime, $M(N_i)$ takes the form of an s-shaped curve (Figures 3.5, top row). Three points of zero net flux exist, corresponding to the two asymmetric equilibria towards the sides (clustered states) and the symmetric distribution in the middle. From the sign of $M(N_i)$ on the intervals between these zeroes, it immediately follows that the clustered states are stable and the symmetric one is unstable. E.g., for $20 \lesssim N_1 \lesssim 150$, the net flux into compartment 1 is negative: This means that during the following strokes compartment 1 will be depleted even more until it reaches the equilibrium at $N_1 \approx 20$, where the average net flux vanishes.

Closing in upon the critical frequency, the s-shaped curve is stretched out around the symmetric distribution (Figure 3.5, middle row). At the critical frequency itself, $M(N_i)$ becomes very flat and has an inflexion point at the symmetric solution. At this point the two clustered states recombine with the symmetric state.

Above the critical frequency only this symmetric equilibrium survives (Figure 3.5, bottom row), which is clearly stable now: For $N_1 > N/2$ the averaged net flux is negative, depleting the compartment until the equilibrium at $N_1 = N/2$ is reached. Equivalently for $N_1 < N/2$ the average net flux is positive and the compartment will gain particles until $N_1 = N/2$.

Also the *fluctuation term* ($\xi(N_i)$) of the mapping in equation (3.3) can be obtained from Figure 3.5. Making a cut in the vertical direction through the contour plots in the left column, the width of the distribution at any given value of N_i corresponds to the magnitude of the fluctuations at that point, i.e., to $\xi(N_i)$.

We find that the distributions along the vertical cuts follow an approxi-

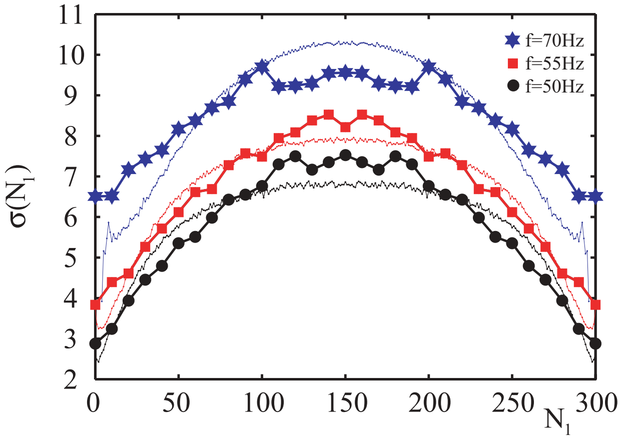

Figure 3.6: The standard deviation $\sigma(N_1)$ [or equivalently, the fluctuation term $\xi(N_1)$ in equation (3.3)] of the roughly Gaussian profiles that one gets by vertically cutting through the contour plots of the net flux in Figure 3.5; the measurements are given by the symbols, which have been connected to guide the eye. The magnitude of the fluctuations is seen to be highest around the symmetric distribution ($N_i = N/2$) and grows mildly with increasing driving frequency $f = 50, 55, 70$ Hz. The thin fluctuating lines represent the quantity $2.8[F(N_1) + F(N_2)]^{1/2}$ (with $F(N_1)$ and $F(N_2)$ taken from Figure 3.4), which follow the curves of $\sigma(N_1)$ reasonably well, in agreement with Eggers' prediction equation (3.6).

mately Gaussian profile, with standard deviation

$$\sigma(N_i) = \sqrt{\langle G^2(N_i) - \langle G(N_i)\rangle^2\rangle} \equiv \xi(N_i) \ . \tag{3.5}$$

The standard deviation $\sigma(N_i)$ is highest in the middle region (near $N_i = N/2$) as can be seen in Figure 3.6, and decreases towards the sides. We also observe that $\sigma(N_i)$ grows with increasing frequency, though less strongly than the magnitude of the average flux (cf. Figures 3.3 and 3.4). This is in agreement with our earlier observation that the relative influence of the fluctuations diminishes at high frequencies above the critical value f_c.

It is interesting to compare our results with the prediction of Eggers [2] concerning the amplitude of the fluctuations. He assumed that the particles passing from one compartment to the other are uncorrelated, which is equivalent to saying that $\xi(N_i)$ is uncorrelated Gaussian white noise [2, 13]. Under this assumption the second moment is given by (cf. equation (8) in Reference [2], properly integrated over time and normalized to hold for the actual particle numbers N_1 and $N_2 = N - N_1$ instead of particle fractions):

$$\sigma^2(N_1) = K^2(f)[F(N_1) + F(N - N_1)] \ , \tag{3.6}$$

with $K(f)$ a factor that may depend on the frequency f (but not on the total number of particles N). In Figure 3.6 we see that this relation is satisfied reasonably well in our simulations, with $K(f) = 2.8$ for each of the frequencies $f = 50, 55, 70$ Hz.

3.4 Potential formulation

In order to quantify the relative influence of the terms $M(N_i)$ and $\xi(N_i)$, we define a potential related to the average net flux $M(N_i)$. In the unclustered regime this potential has a single minimum at the symmetric distribution, whereas in the clustered regime it becomes a double-well potential with a barrier in the middle. By comparing the height of this barrier to the amplitude of the noise term $\xi(N_i)$, we have a direct measure for the relative importance of the fluctuations.

The average net flux $M(N_i)$ can be interpreted as a force, working towards one compartment. With this force one can associate a potential $V(N_i)$ as follows:

$$M(N_i) = -\frac{dV(N_i)}{dN_i} \ , \tag{3.7}$$

or equivalently:

$$V(N_i) = -\int_{N/2}^{N_i} M(N_i')dN_i' \ . \tag{3.8}$$

In Figure 3.7 we have plotted the potentials corresponding to the average net fluxes in Figure 3.5, for $N = 300$ particles. In fact, the raw net flux from the MD simulations (i.e., from the M depicted in Figure 3.5) was fitted to a cubic polynomial, yielding a potential of the following general form:

$$V(N_i) = V_0 + aN_i^2 + bN_i^4 \ . \tag{3.9}$$

The values of V_0, a, and b for each potential are given in the caption of Figure 3.7.

For strong shaking ($f = 70$ Hz, Figure 3.7c) the potential has one single minimum at $N_i = 150$, representing the stable symmetric state. Upon reducing the frequency, the bottom of the potential becomes flatter and flatter, giving the fluctuations ample opportunity to have a big effect on the particle numbers in each compartment. At the critical shaking frequency

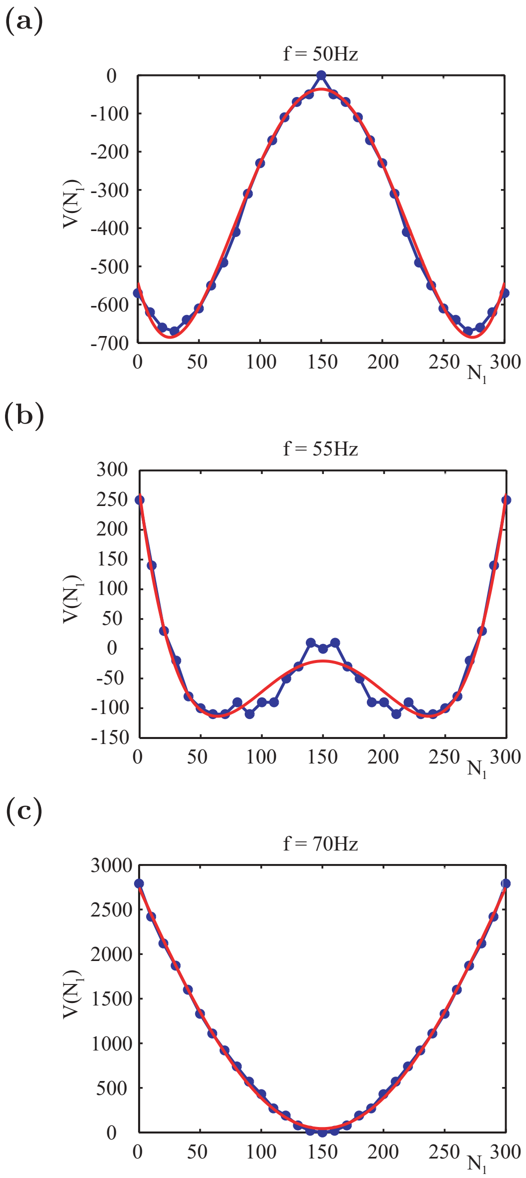

Figure 3.7: The potential $V(N_i)$ corresponding to the average net fluxes for the same three frequencies as in Figure 3.5. (a): For mild shaking ($f = 50$ Hz) the potential consists of two wells (representing the clustered states) separated by a barrier. (b): At the critical shaking frequency (close to $f = 55$ Hz) the barrier disappears. (c): For higher shaking strengths the potential has just one single minimum at the symmetric state $N_i = N/2$ ($f = 70$ Hz). The data have been fitted to a quartic potential as in equation (3.9); the coefficients $\{V_0, a, b\}$ take on the values $\{-36.34, -0.0848, 2.77 \times 10^{-6}\}$ for $f = 50$ Hz, $\{-20.68, -0.0248, 1.66 \times 10^{-6}\}$ for $f = 55$ Hz, and $\{43.48, 0.1396, -8.65 \times 10^{-7}\}$ for $f = 70$ Hz.

itself (close to $f = 55$ Hz, Figure 3.7b) the minimum in the center becomes a maximum (the symmetric state becomes unstable) and the potential develops two wells corresponding to the clustered states. So in the clustered regime ($f = 50$ Hz, Figure 3.7a) the potential consists of two wells separated by a barrier in the middle.

As long as the amplitude of the fluctuations is larger than the height of the potential barrier, the clustering dynamics into either well will be interrupted (at irregular time intervals) by a statistical fluctuation that drives the system back to the symmetric state (and from there again into any of the two wells). This is exactly the intermittent behavior that we observed in the MD simulations for frequencies just below the critical value f_c. In Figure 3.8 the amplitude of the fluctuations is compared to the height of the potential barrier, as function of f, for $N = 300$, 100, and 50 particles. It is seen that the region where the fluctuations are larger than the barrier grows with decreasing total particle number N, just as expected.

When the driving frequency is reduced further below f_c, the height of the potential barrier increases (and at the same time the amplitude of the fluctuations decreases) until at a certain point the fluctuations are not able to kick the system out of the well anymore. It is at this point (for $N = 300$ and 100 particles) that the mean-field behavior sets in. For $N = 50$ the system never reaches such a point.

The situation is further illustrated in Figure 3.9a, which shows the bifurcation diagram for $N = 300$ particles (cf. the backbone in Figure 3.2, top): Just below the critical frequency f_c the points in this diagram do not follow the mean-field behavior (the dashed curve, branching off as $(f_c - f)^2$) but stay closer to the symmetric state. This is the result of the fact that the system still spends a considerable part of the time near the symmetric state, forced by the fluctuations. The mean-field behavior is seen to set in around $f = 53$ Hz. This is illustrated also in the inset of Figure 3.9a, where the dashed straight line represents the mean-field prediction.

The deviations from the mean-field behavior are much more apparent for smaller values of N, as in Figure 3.9b for $N = 100$. Here the critical value lies around $f_c = 32$ Hz, but the mean-field behavior does not set in before $f \approx 28$ Hz.

The same potential formulation can also be applied when the total number of particles is smaller. In Figure 3.10 we show two typical potentials for $N = 100$ particles, at driving frequencies $f = 25$ Hz (clustered regime) and $f = 36$ Hz (symmetric regime). These have the same form as those for $f = 50$ Hz and $f = 70$ Hz with $N = 300$ particles (see Figure 3.7, right-

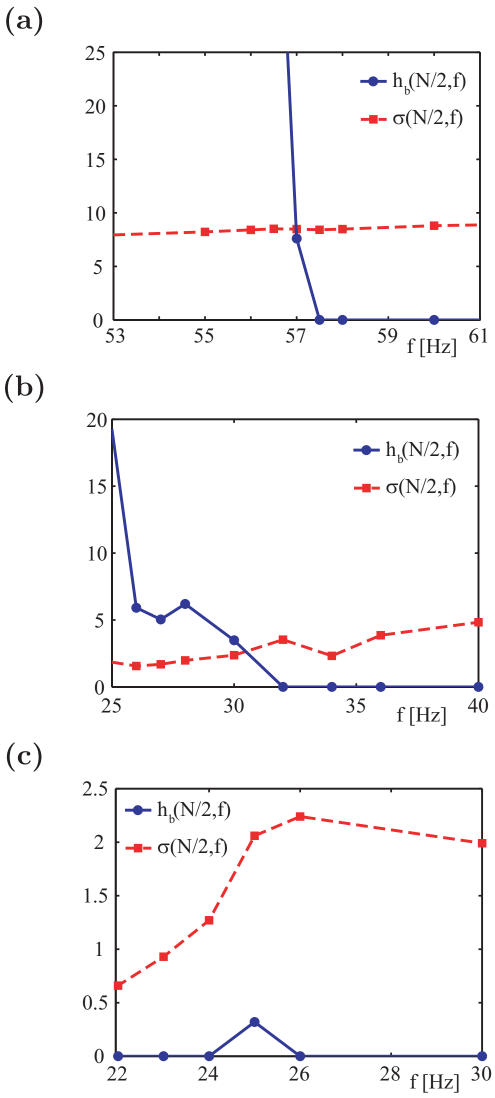

Figure 3.8: The amplitude of the fluctuations (represented by the maximal standard deviation $\sigma(N/2)$, i.e. $\xi(N/2)$, see Figure 3.6; squares connected by dashed line) and the height of the potential barrier $h_b(N/2)$ (cf. Figure 3.7; dots connected by solid line) as function of the driving frequency f, for $N = 300$, 100, and 50 particles (top to bottom). There is a region below the critical frequency f_c (at which the barrier height becomes non-zero) where the fluctuations are still larger than the barrier height, which means that the system will switch intermittently from one potential well to the other, thus frustrating the mean-field behavior. The size of this region (and hence the overall influence of the fluctuations) grows for decreasing particle number N. For $N = 50$ particles the fluctuations are seen to dominate at all frequencies.

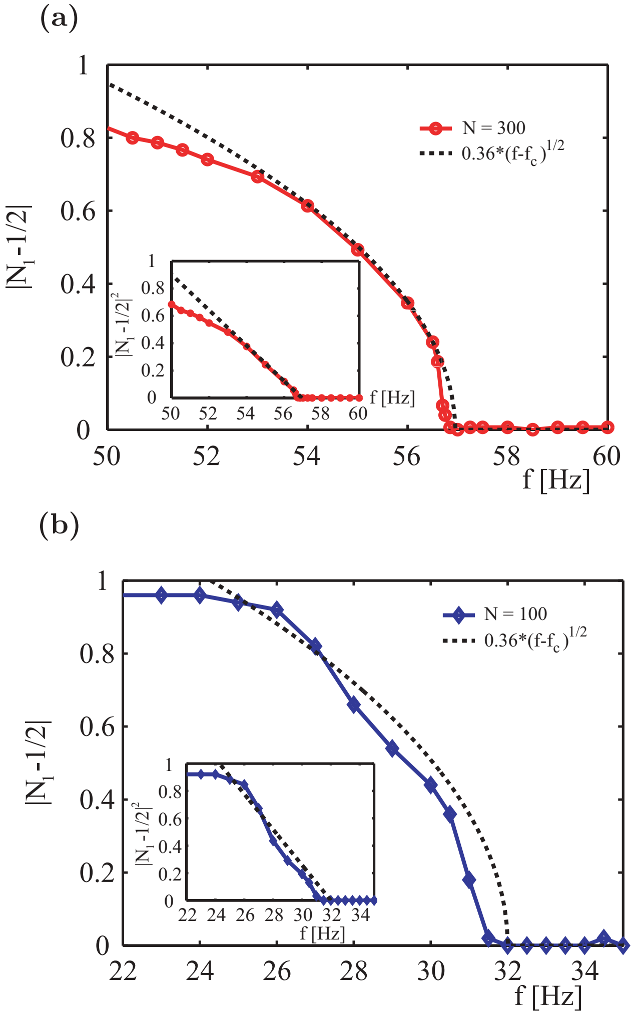

Figure 3.9: (a) The bifurcation diagram for $N = 300$ particles, driven at an amplitude of $a = 1$ mm. Just below the critical frequency $f_c \approx 56$ Hz, the mean-field behavior (indicated by the dashed line) is slightly thwarted by the statistical fluctuations in the system. The inset shows the same diagram with the quantity along the vertical axis squared: the mean-field behavior now is represented by a straight line. (b) The same for $N = 100$ particles. It is seen (also in the inset) that the mean-field behavior is much more disturbed than in (a).

most column), but the absolute values differ considerably. In particular, the height of the potential barrier for $N = 100$ is much smaller than for $N = 300$, which means that it is much easier for the fluctuations to overcome it.

It may also be noted that the numerical data for $N = 100$ are coarser than those for $N = 300$. This is due to a practical complication at small particle numbers: the increased influence of the fluctuations makes it necessary to run the MD simulations for a much longer time before one obtains a reliable average net flux $M(N_i)$, needed for the potential $V(N_i)$. This problem becomes even worse for the case of $N = 50$ particles.

3.5 Time correlation

A useful indicator for a phase transition in equilibrium statistical physics is the normalized time autocorrelation function $C(\tau)$ [9, 11, 14]:

$$C(\tau) = \frac{\langle \delta n(t) \delta n(t+\tau) \rangle_t}{\langle \delta n^2(t) \rangle_t} \ , \tag{3.10}$$

where $\delta n(t) \equiv n(t) - \langle n(t) \rangle_t$ and the index t indicates that we take the temporal average. The function $C(\tau)$ is a measure of how correlated the signal $n(t)$ is to its value $n(t + \tau)$ a time τ later. It is 1 when the signal is totally correlated (for $\tau = 0$), and fluctuates around zero when all correlations are lost. The typical lifetime of correlations in the signal τ_0 can be defined as the value of τ for which $C(\tau)$ becomes smaller than $e^{-1}(\approx 0.37)$, corresponding to the standard mean-field form of the autocorrelation function $C_{mf}(\tau) = e^{-\tau/\tau_0}$ [11, 15–17]. Alternatively, one may define τ_0 via the slope of $C(\tau)$ as follows:

$$\frac{1}{\tau_0} = -\frac{dC(\tau)}{d\tau}\bigg|_{\tau=0} \ , \tag{3.11}$$

which is the *decay rate* of the correlations at short timescales. Since we cannot take the validity of the mean-field approximation for granted here, we will use this second definition of τ_0.

For a standard second-order phase transition the lifetime τ_0 is known to diverge at the critical point, or equivalently, the inverse timescale $1/\tau_0$ (the decay rate of the correlations) goes to zero. We want to see to what extent this still holds for the clustering transition in our granular system, for decreasing values of the particle number N.

For this purpose, we have to determine averages over the time signal. This poses no difficulties in the regimes where the particles are either clearly

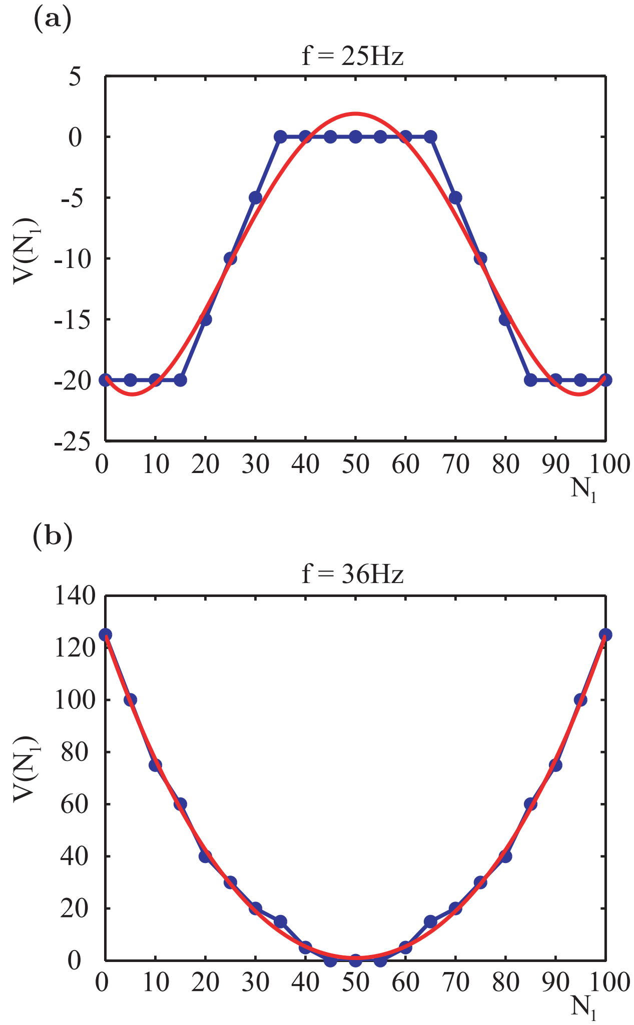

Figure 3.10: The potential $V(N_i)$ for $N = 100$ particles at mild shaking ($f = 25$ Hz) and strong shaking ($f = 36$ Hz), corresponding to the symmetric and clustered regimes, respectively (cf. Figure 3.2, top right). The raw data from the average net flux have been fitted to a quartic polynomial as in equation (3.9); the coefficients $\{V_0, a, b\}$ are $\{1.90, -0.0231, 5.81 \times 10^{-6}\}$ for $f = 25$ Hz, and $\{1.00, 0.0442, 2.14 \times 10^{-6}\}$ for $f = 36$ Hz.

clustered or not clustered at all, but in the intermittent regime just below the critical frequency (see Figure 3.1, middle) the mean value $\langle n(t)\rangle$ (or equivalently, $\langle N_1(t)\rangle$) is an ambivalent quantity, since the particle numbers fluctuate between two different equilibrium points. That is why in this regime we work instead with the related quantity

$$\epsilon(t) = |\frac{N}{2} - N_1(t)| + \frac{N}{2} \ , \tag{3.12}$$

which makes all the data fluctuate around only one equilibrium point (namely the upper one, between $N/2$ and N). The corresponding correlation function takes the form:

$$C(\tau) = \frac{\langle \delta\epsilon(t)\delta\epsilon(t+\tau)\rangle_t}{\langle \delta\epsilon^2(t)\rangle_t} \ . \tag{3.13}$$

The result is depicted in Figure 3.11 for $N = 300$ particles. The autocorrelation goes from 1 downward, at different rates for different frequencies. As expected, the slowest decrease is observed for f around the critical frequency $f_c \approx 56$ Hz.

From these curves, one can obtain the corresponding decay rates $1/\tau_0(f)$ (equation (3.11)) that are plotted in Figure 3.12. This figure shows the decay rates not only for $N = 300$ particles (top), but also for $N = 100$ (middle) and $N = 50$ (bottom). Below the critical frequency f_c we have evaluated $1/\tau_0$ both from the raw data (with $C(\tau)$ given by equation (3.10), solid stars) *and* from the intermittency-corrected data (with $C(\tau)$ as in equation (3.13), open stars). As explained above, just below f_c one should work with the corrected, open symbols; for $f \ll f_c$ the intermittency disappears from the signal and the solid and open symbols simply coincide.

The standard behavior, namely that $1/\tau_0$ goes to zero at the critical frequency, is still clearly present for $N = 300$ (see the dashed lines). In fact, from this plot of τ_f we get the most accurate determination of the value of the critical frequency f_c so far, namely $f_c = 55.7$ Hz.

The decay rate is seen to approach zero linearly, as $1/\tau_0 \propto |f - f_c|^\gamma$ with the critical exponent $\gamma = 1$ known from mean-field theory [15]. In the symmetric regime ($f > f_c$) this linear behavior extends relatively far beyond the critical point, whereas in the clustered regime ($f < f_c$) it breaks down much more quickly. This is in agreement with the Landau theory for second-order phase transitions and is due to the nonlinearities that come into play as soon as the system moves away from the symmetric equilibrium [11, 15, 16].

Also for $N = 100$ (Figure 3.12, middle plot) the decay rate $1/\tau_0$ is still seen to tend to zero linearly at the critical point, which on the basis of this plot is estimated to lie at $f_c \approx 28.6$ Hz. This is considerably smaller than

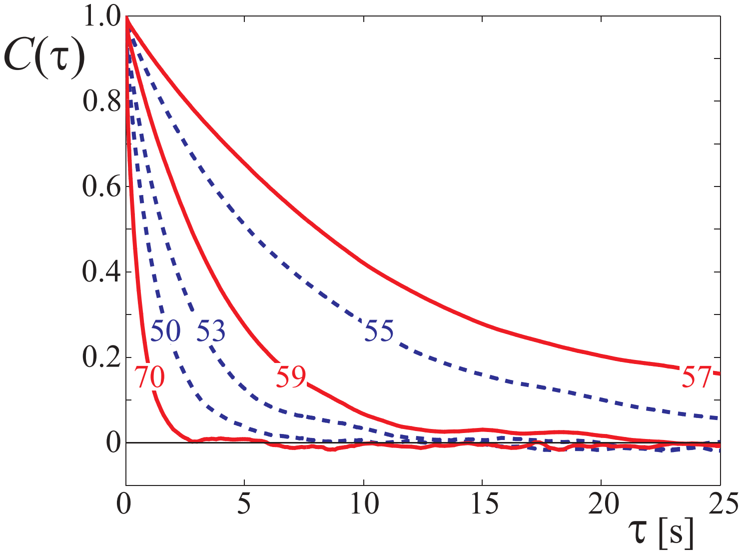

Figure 3.11: The normalized autocorrelation function $C(\tau)$ for $N = 300$ particles, for various driving frequencies f (indicated in the plot). The curves all decrease from the initial value 1, but at different rates depending on f. Close to the critical frequency $f_c \approx 56$ Hz the decay is slowest. The curves corresponding to $f < f_c$ are dashed, to distinguish them more easily from those for $f > f_c$ (solid lines).

the value $f_c \approx 32$ Hz we had found earlier from the bifurcation diagram for $N = 100$ in Figures 3.2 and 3.9b.

Finally, for $N = 50$ particles (Figure 3.12, bottom) the mean-field behavior breaks down, as expected. A proper determination of the critical point f_c is no longer possible from this plot, neither can one reliably derive a critical exponent γ.

3.6 Conclusion

In conclusion, we have seen that statistical fluctuations profoundly influence the clustering behavior of a compartmentalized granular gas. As long as the number of particles (N) is sufficiently large, the clustering still largely follows the lines of a standard second-order phase transition (i.e., a pitchfork bifurcation with critical exponent $\beta = 1/2$). For smaller N, however, the enhanced influence of statistical fluctuations breaks the mean-field behavior. We demonstrated this by means of bifurcation diagrams (Figure 3.2) and

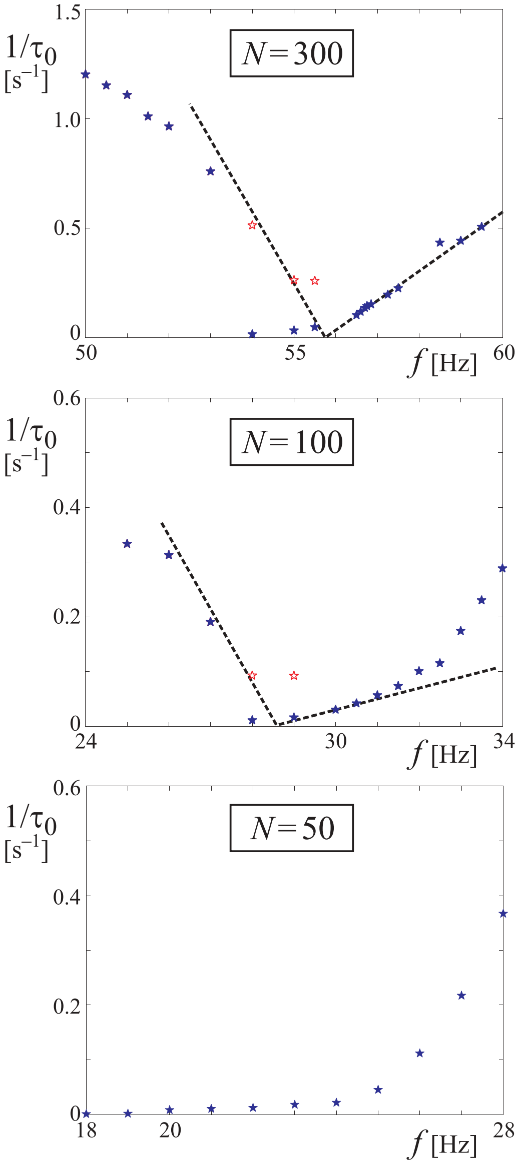

Figure 3.12: The correlation decay rates $1/\tau_0$ as function of the shaking frequency for $N = 300, 100$, and 50 particles respectively. The standard behavior of $1/\tau_0$ going to zero at the critical frequency f_c is still recognizable for $N = 300$ and 100, but deteriorates for $N = 50$. The plots for $N = 300$ and $N = 100$ show that $1/\tau_0$ approaches zero linearly, i.e., as $|f_c - f|^\gamma$ with the mean-field critical exponent $\gamma = 1$. The solid stars are based on the raw data; the open ones have been corrected for the intermittency that occurs just below the critical point, according to the recipe given in the text (see equations (3.12)-(3.13)).

also via the correlation time τ_f at the clustering transition (Figure 3.12).

In order to model the fluctuations in our system, we constructed the mapping according to equation (3.3) (describing the outflow of particles from a compartment per shaking cycle) in which the mean-field flux and the fluctuations appear as two separate terms. This separation enables us to directly compare the relative importance of both contributions to the dynamics and to study how the fluctuations start to dominate for decreasing particle number N.

Our results show that already at $N = 300$ (i.e., much less than the 10^{23} particles of textbook statistical physics) mean-field results and the Eggers flux theory hold very nicely. Only for smaller N the finite-number noise starts to dominate, and the mean-field description breaks down.

References

[1] H.J. Schlichting and V. Nordmeier, Math. Naturwiss. Unterr. **49**, 323 (1996).

[2] J. Eggers, Phys. Rev. Lett.**83**, 5322 (1999).

[3] K. van der Weele, D. van der Meer, M. Versluis, and D. Lohse, Europhys. Lett. **53**, 328 (2001).

[4] D. van der Meer, K. van der Weele, and D. Lohse, Phys. Rev. E**63**, 061304 (2001).

[5] D. van der Meer, K. van der Weele, and D. Lohse, Phys. Rev. Lett. **88**, 174302 (2002).

[6] A. Lipowski and M. Droz, Phys. Rev. E**65**, 031307 (2002).

[7] U. Marini Bettolo Marconi and A. Puglisi, Phys. Rev. E**68**, 031306 (2003).

[8] L.E. Reichl, *A modern course in statistical physics*, 2nd ed. (Wiley, New York, 1998).

[9] N.G. van Kampen, *Statistical processes in physics and chemistry* (North-Holland Personal Library, Amsterdam, 1992).

[10] D.I. Goldman, J.B. Swift, and H.L. Swinney, Phys. Rev. Lett. **92**, 174302 (2004).

[11] P.M. Chaikin and T.C. Lubensky, *Principles of condensed matter physics* (Cambridge University Press, Cambridge, 1995).

[12] D. van der Meer, *Flux dynamics in the Eggers approximation*, unpublished lecture notes (Univ. of Twente, 2002).

[13] H. Risken, *The Fokker-Planck equation* (Springer, Berlin, 1984).

[14] H.E. Stanley, *Introduction to phase transitions and critical phenomena* (Oxford University Press, New York and Oxford, 1971).

[15] S.-K. Ma, *Modern theory of critical phenomena*, Frontiers in Physics Lecture Note Series Vol. 46 (W.A. Benjamin, Reading, MA, 1976).

[16] X.-L. Qiu and G. Ahlers, *Dynamics of fluctuations below a stationary bifurcation to electroconvection in the planar nematic liquid crystal N4*, preprint (Univ. of California, Santa Barbara, 2004).

[17] S.-Q. Zhou and G. Ahlers, *Fluctuations of a homeotropically aligned nematic lquid crystal in the presence of an applied voltage*, preprint (Univ. of California, Santa Barbara, 2004).

Chapter 4

Competitive clustering in a bidisperse granular gas §

Abstract

A compartmentalized bidisperse granular gas is experimentally found to cluster competitively: By tuning the shaking strength, the clustering can be directed either towards the compartment initially containing mainly small particles or to the compartment containing mainly large particles. Here, the conditions under which this competitive clustering occurs are studied experimentally, numerically (by means of molecular dynamics simulations), and analytically. A theoretical flux model is derived that quantitatively accounts for the observed phenomena.

4.1 Experimental observations

The clustering behavior of a granular gas in compartmentalized systems as described in chapter 2 and 3 concerns granular gases consisting of (approximately) identical particles. In this chapter we will study the clustering behavior of a *bidisperse* mixture of large and small particles. The crucial observation is that due to the fact that bidisperse granular gases can demix, the clustering scenario becomes richer than for monodisperse granular gases. A compartmentalized bidisperse granular gas is experimentally found to clus-

---

§ Adapted from: René Mikkelsen, Devaraj van der Meer, Ko van der Weele, and Detlef Lohse, *Competitive Clustering in a Bidisperse Granular Gas*, Phys. Rev. Lett. **89**, 214301 (2002), and René Mikkelsen, Devaraj van der Meer, Ko van der Weele, and Detlef Lohse, *Competitive clustering in a bidisperse granular gas: Experiment, molecular dynamics, and flux model*, Phys. Rev. E **70**, 061307 (2004).

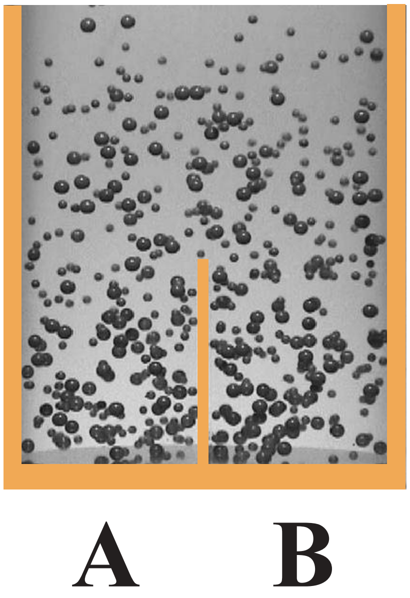

Figure 4.1: Image from the experiment with a bidisperse mixture of 300 large (radius = 2.5 mm) and 600 small (radius =1.25 mm) steel beads that is driven vigorously; no clustering takes place here. The shaking frequency $f = 110$ Hz, and the shaking amplitude a is 1.0 mm. Only the lower third of the tube is shown, since particles rarely go up all the way to the top lid.

ter *competitively*: By tuning the shaking strength, the clustering can be directed either towards the compartment initially containing mainly small particles or to the compartment containing mainly large particles. An example of this competition was shown in the introductory chapter (Figure 1.1) for a mixture of two different types of vibrated candy. In this chapter, the conditions under which this competitive clustering occur are studied experimentally, numerically (by means of molecular dynamics simulations), and analytically. A theoretical flux model is derived that quantitatively accounts for the observed phenomena.

We will start here with a discussion of the experimental results for bidisperse mixtures; these will motivate the work in subsequent sections of this chapter. Our experimental setup consists of a cylindrical glass tube with inner diameter 11.2 cm and height 42.2 cm, divided into two equal compartments, labelled A and B, by a wall of height 6 cm. The tube is filled with grains and mounted on a shaker, which brings the system into a gaseous state

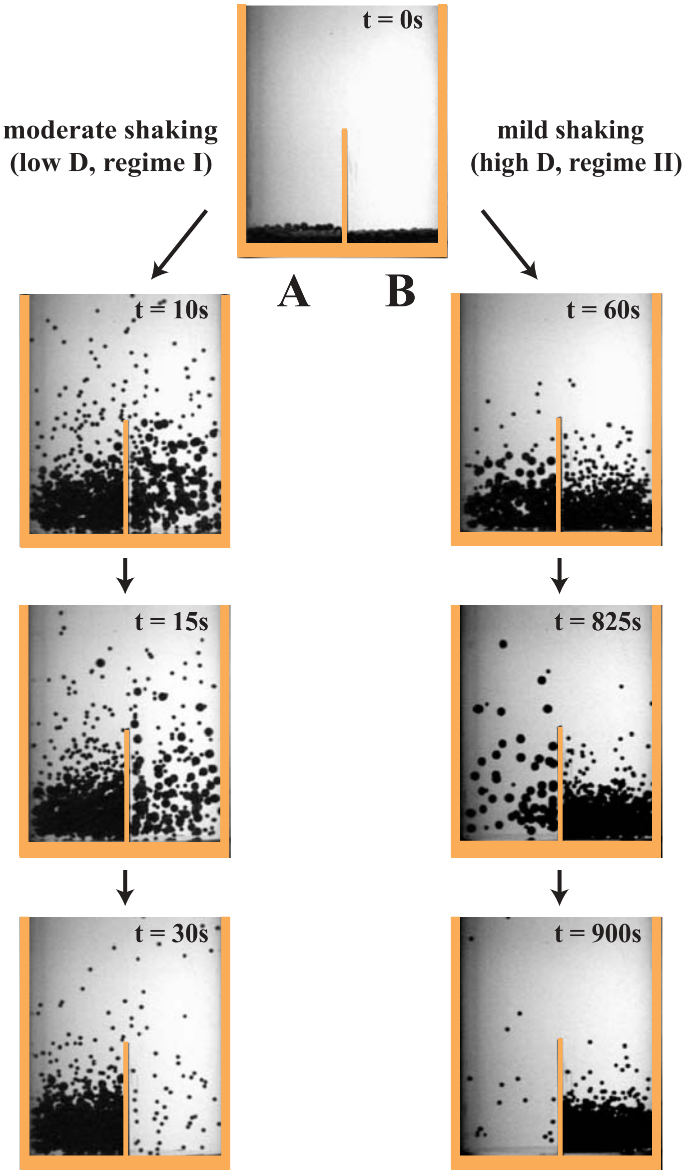

Figure 4.2: Images from two experiments with a bidisperse mixture of steel beads, starting from the same initial condition; again only the lower third of the tube is shown. For relatively strong shaking (left column) the clustering is directed towards the *left* compartment, whereas for mild shaking (right column) it goes into the *right* compartment. The shaking frequency in the left column is $f = 60.0$ Hz, and in the right column 37.5 Hz, while the peak-to-peak amplitude in both cases is $2a = 2$ mm. The initial condition (topmost picture) is {180 large, 200 small} in the left compartment, and {120 large, 400 small} in the right one. With the radius of the large beads ($r_1 = 2.50$ mm) being twice that of the small ones ($r_2 = 1.25$ mm), this means that initially 55% of the total particle mass is in the left compartment.

through vertical, sinusoidal vibrations with frequency f and amplitude a. We will take these two parameters together in the inverse shaking strength, which is proportional to $1/(af)^2$. In fact, we define D as $16\pi \frac{gh}{(2af)^2}(1-\epsilon^2)^2$, where g is the gravitational acceleration, h is the height of the wall and ϵ is the coefficient of restitution. This expression comes from balancing the energy dissipated in grain-grain collisions with the energy input from the shaker; for more details see section 4.3.5. In the experiments presented below, we have $h = 6.0$ cm and $\epsilon = 0.9$.

Figures 4.1 and 4.2 show images from experiments with a mixture of $P_1 = 300$ stainless steel beads of radius $r_1 = 2.50$ mm and $P_2 = 600$ smaller ones of $r_2 = 1.25$ mm. For very strong shaking (small D) the large and small particles distribute themselves uniformly over the two compartments (Figure 4.1). This will be denoted as regime **0**. In this case, the dissipation from the particle collisions is overwhelmed by the energy input into the system. But for moderate and mild shaking strengths, clustering occurs as shown in Figure 4.2. Note that in both cases the same, asymmetric, initial distribution is taken: $\{180$ large, 200 small$\}$ in the left compartment (A), and $\{120$ large, 400 small$\}$ in the right compartment (B). This means that in the initial situation 55% of the total particle mass is in compartment A. The peculiar feature now is that depending on the precise value of the inverse shaking strength D, the cluster either ends up in the left compartment (A) or in the right compartment (B). Clearly, the outcome of the experiment is strongly dependent on the shaking strength.

When we reduce the shaking strength below a certain threshold, starting out from the same initial state, the particles form a cluster in compartment A, see Figure 4.2, left column. This is regime **I**. The direction of the clustering is towards the larger total particle mass. The reason is as follows: Many of the small beads quickly cluster in compartment A, where the dissipation is highest due to the greater number of large beads, which (with their larger mass and surface area) act as "coolers". The remaining beads in compartment B are able to jump higher than before, since there are fewer collisions, and also large ones now start to make it over the wall into compartment A. After about 20 seconds to a minute (depending on the value of D) the final state is reached: a dynamical equilibrium with practically all large particles and most of the small ones in compartment A and only a few rapid small particles in compartment B.

For very mild shaking, however, the same initial condition surprisingly leads to a cluster in the *other* compartment: see Figure 4.2, right column. We will call this regime **II**. The series of events is as follows: At first the large particles stay close to the floor, transferring energy from the vibrating bottom to the smaller ones above them, which thereby gain relatively high velocities. This is reminiscent of the demonstration experiment in which one puts a tennis ball on top of a basket ball and lets them drop together: when they hit the ground, the tennis ball is “launched” and jumps much higher than its release height [11]. The effect is stronger in the left box (which has more large particles) than in the right box, and thus the small beads go preferentially into the latter (B). As a consequence, the remaining particles in compartment A become more mobile, and after a couple of minutes the first large beads also begin to make it over the wall into compartment B, where they are immediately swallowed by the developing cluster. With every particle that leaves compartment A, the process progressively speeds up. In the experiment of Figure 4.2, right column, the clustering is complete after 15 minutes.

An overview of the competitive clustering transition for a range of shaking strengths using the same particles and initial distribution as in Figure 4.2 is shown in Figure 4.3. Remember that the parameter D is proportional to the inverse shaking strength, such that a small D value corresponds to strong shaking (regime 0, $D < 10$). For moderate shaking (regime I, $10 < D < 140$) we find clustering in compartment A, and for mild shaking (regime II, $D > 140$) the clustering takes place in compartment B. The transition between regime I to II is quite abrupt.

The experiments thus show that clustering in a bidisperse gas has a rich phenomenology and in the remainder of this chapter we will give a quantitative description of this competitive clustering phenomenon. First of all we will perform molecular dynamics (MD) simulations, which allow us to probe in detail the granular temperature distribution and competitive clustering for a wide range of parameters. In the simulations we will work with particles of the same material, which thus have the same material density ρ and will be taken to have one constant coefficient of restitution ϵ; that is, we neglect the dependence of ϵ on the velocity and size of the particles [12, 13]. This assumption is found to not influence the phenomenology substantially, illustrating the robustness of the experimentally observed phenomena. It is important to realize, that even though the clusters in Figure 4.2 look very dense, this is an optical illusion due to the fact that the particles are projected onto a plane; in reality they are scattered throughout the three-dimensional compartment. We therefore take the number of particles such that at rest they form one to two layers on the bottom of the container. This number is sufficiently large to keep the relative effect of statistical fluc-

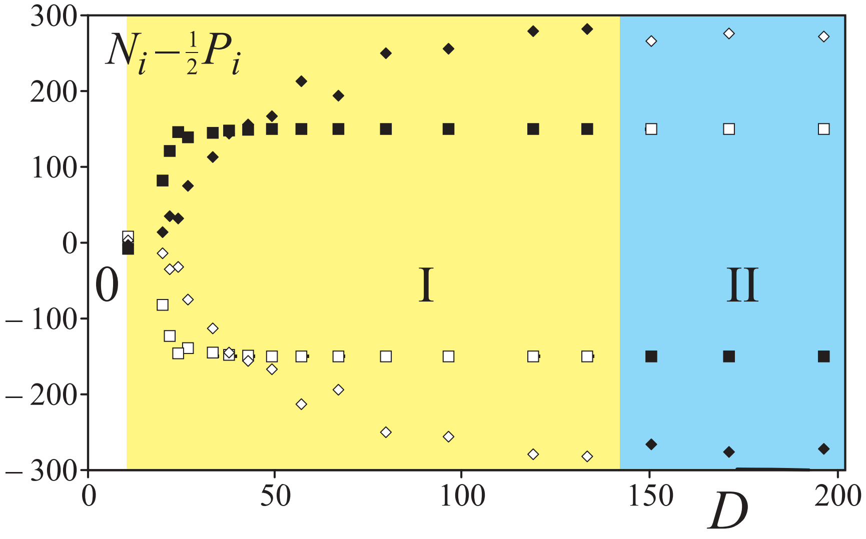

Figure 4.3: Experimental results showing the three different regimes 0, I, and II, for our setup filled with a mixture of stainless steel beads: $P_1 = 300$ large ones with radius $r_1 = 2.5$ mm, and $P_2 = 600$ small ones with radius $r_2 = 1.25$ mm. Every new run was started from the same initial condition: $\{180 \text{ large}, 200 \text{ small}\}$ in compartment A, and $\{120 \text{ large}, 400 \text{ small}\}$ in B. The particle numbers N_i $(i = 1, 2)$ are given relative to the symmetric solution: $N_i - \frac{1}{2}P_i$. The squares correspond to the large beads, and the diamonds to the small ones. Solid symbols refer to compartment A, and open symbols to B; note that every measurement is thus represented by two points, which accounts for the mirror-symmetry of the plot.

tuations limited and thus to allow for a mean field description. On the other hand, it is small enough to keep the gas reasonably dilute even in the clustered situation.

4.2 MD simulations for one compartment

4.2.1 Numerical scheme

For the simulations we use a three-dimensional event driven code: Between two events (collisions) the particles move freely, describing parabolic paths under the influence of gravity, until the next collision occurs. A collision can be either between particles or between a particle and a wall, and is signalled by a spatial overlap of the two. At such an event, the velocities of the particles after contact are computed from the velocities just before contact using Newton's laws.

The particles are taken to be hard spheres. This means that we ignore any deformations, which for the steel particles used in our experiments is a reasonable approximation. The coefficient of normal restitution ϵ for particle-particle collisions is taken to be constant, $\epsilon = 0.85$, and the same for the large and small beads. The coefficients of tangential restitution and dynamical friction are adjustable in the code, but for the simulations presented here they are set equal to their ideal (dissipationless) values.

The coefficients of restitution between the particles and the walls and bottom can be adjusted independently. For the coefficient of normal restitution we use 0.95, obtained from test experiments in which we let the beads bounce on solid plates of glass (representing the walls) and aluminum (for the bottom).

For simplicity the experimental setup is simulated as a rectangular box with infinitely high side walls. The ground area of each compartment and the height of the wall between them is the same as in the actual experiment. The bottom is vibrated vertically with adjustable frequency f and amplitude a following a sinusoidal wave form.

4.2.2 Height distribution and granular temperature

One of the main assumptions in the bidisperse flux model is that the granular *temperatures* T_1 and T_2 of the large and small particles are independent of the height z. This assumption leads to the barometric height distribution, just as in an ordinary gas. That is, the number densities of both species (i = 1,2) are taken to decay exponentially with z:

$$n_i(z) = n_i(0)e^{-m_i g z/T_i}. \tag{4.1}$$

The temperature T_i is defined in analogy with the standard relation from statistical physics $\frac{1}{2}m_i\langle v_i^2\rangle = \frac{3}{2}k_B T_i$, where the Boltzmann constant k_B is to be replaced by a mere number. Here we will choose $k_B = 1$. So $T_i \equiv \frac{1}{3}m_i\langle v_i^2\rangle$ is directly proportional to the mean kinetic energy of the particles of species i. Its value is determined by a balance between the input of energy due to the vibrating bottom and the dissipation of energy via the collisions [14].

The second, bolder assumption in the model is that $T_1 = T_2 (= T)$. The large and small particles are (per compartment) taken to be in thermal equilibrium with each other at the *same* granular temperature, such that equation (4.1) simplifies to $n_i(z) = n_i(0)\exp\{-m_i g z/T\}$. For size ratios ψ close to unity (the monodisperse limit) this is expected to hold well,

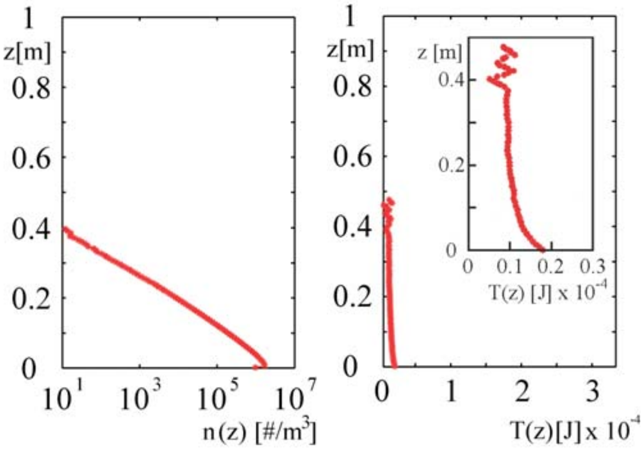

Figure 4.4: Molecular Dynamics (MD) simulation results for a monodisperse granular gas (size ratio $\psi = 1$) shaken at frequency $f = 70$ Hz and amplitude $a = 1$ mm. Shown are the particle density (left) and the granular temperature (right) as function of the height z. The ground area of the container is $\Omega = 100$ cm^2 (equivalent to the experimental setup of Figure 4.2 without the central wall), the number of particles is P=900, their radius is 1.25 mm, and the plots are based on 10^6 numerical snapshots of the gas in its steady state, sampled at a rate of 1000 per second. The scale used in these plots is the same as in Figures 4.5 and 4.6, to allow for a comparison with the bidisperse case.

but for large values of ψ the correspondence will deteriorate. Several recent studies [15–20] have shown that energy equipartition generally breaks down in bidisperse granular gases, with the heavier particles having a higher temperature.

In particular, Wildman and Parker [15] used positron emission particle tracking to experimentally determine the granular temperature in a vibrofluidized mixture of glass beads with radii $r_1 = 2.5$ mm and $r_2 = 2.0$ mm ($\psi = 1.25$). They found that the temperature of the larger particles was always higher than that of the smaller ones. Keeping the total particle mass in the system the same, the temperature ratio T_1/T_2 could be raised by increasing the ratio (P_1/P_2) between the numbers of large and small beads.

To check the temperature ratio and the density profiles in our own system, we performed MD simulations. In Figures 4.4-4.6 the results are shown for $\psi = 1$, 2, and 3, respectively.

In all three cases $\log(n_i(z))$ (for i =1 and 2) follows an approximately

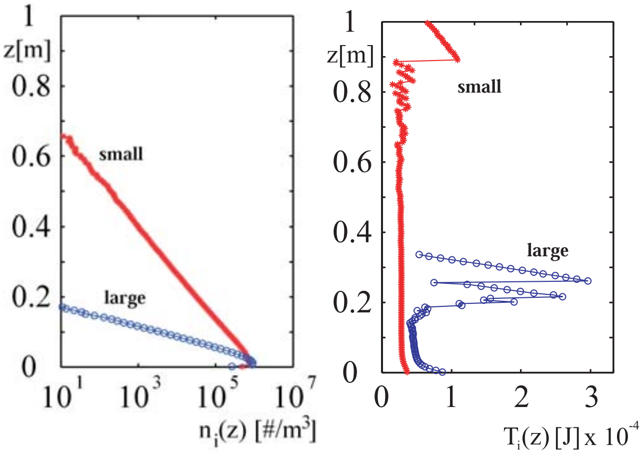

Figure 4.5: Same as Figure 4.4, but now for a bidisperse granular gas consisting of 300 large and 600 small particles with size ratio $\psi = 2$. The small particles have the same size as those in Figure 4.4, i.e., $r_2 = 1.25$ mm. The density profiles of both the large and the small particles follow straight lines, indicating an exponential decay with z (barometric height distribution). The right plot shows that the granular temperature of the large beads is larger than that of the small beads. The slanting lines at the top of the temperature profiles correspond to free parabolic flights of single particles; see also Figure 4.7.

straight line, indicating that the density profiles of both large and small beads indeed decay exponentially, with the large-particle profile decaying faster in agreement with equation (4.1). Only at small z do the profiles deviate significantly from the straight line. This is caused by the vibrating floor: Many of the particles here have a relatively high energy, since they have just been kicked by the floor but have had no chance yet to pass on their energy to the other particles. So the temperature close to the bottom is high and this means that the curve of $\log(n_i(z))$ flattens. Moreover, a very narrow region immediately above the floor is swept clean by the vibrating bottom itself.

An interesting observation is that the small particles in the bidisperse situations (Figures 4.5 and 4.6) reach considerably larger heights and have a higher temperature than the same particles in the monodisperse situation of Figures 4.4. This is the “tennis ball on basketball” effect mentioned earlier. The maximum height reached by the small particles increases with ψ, i.e., with the growing size of the larger particles.

The above characteristics are also reflected in the temperature profiles.

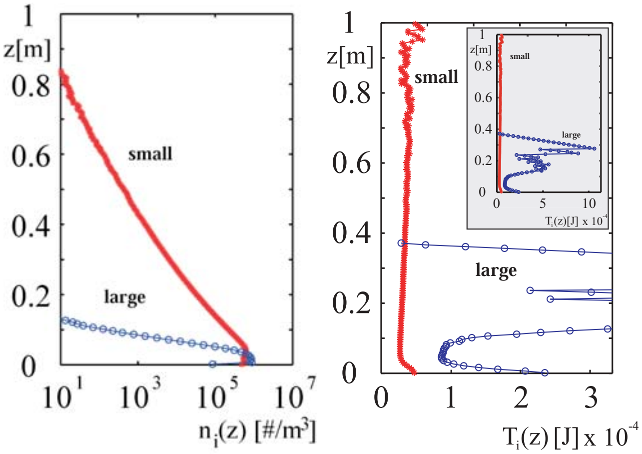

Figure 4.6: Same as Figure 4.5, but now for size ratio $\psi = 3$. The densities of the large and small particles still follow an approximately exponential decay. The temperature shows considerable deviations from a constant value especially for the large particles (see also the inset, in which the same profiles are shown on a different scale); however, the upper region of the temperature profile is made up by only a few particles and has hardly any statistical weight. It is apparent that the temperature difference between the large and small particles has increased with ψ, cf. Figure 4.8.

The temperature is found to be roughly constant except at the bottom and top. Close to the bottom the temperature is significantly higher, especially for the large particles. That this is indeed caused by the vertical kicks from the vibrating floor is shown in Figures 4.7, where the individual x, y, and z components of the temperature are given (for $\psi = 2$): For the large particles the z component close to the bottom is seen to be almost *three* times as high as the other two components.

In the bulk of the profile (the long central part) the temperature components are roughly equal, which means that the velocity distribution is approximately constant and isotropic here.

The upper part of the temperature profile shows considerable fluctuations. The reason for this is that the particle density is rather low here, so (a) the statistics is relatively poor and (b) the collisions between particles are rare, which makes the equipartition of energy via collisions less effective. In this region the mean free path of the particles increases rapidly with height and their kinetic energy is primarily converted into potential energy due to gravity and not lost in collisions.

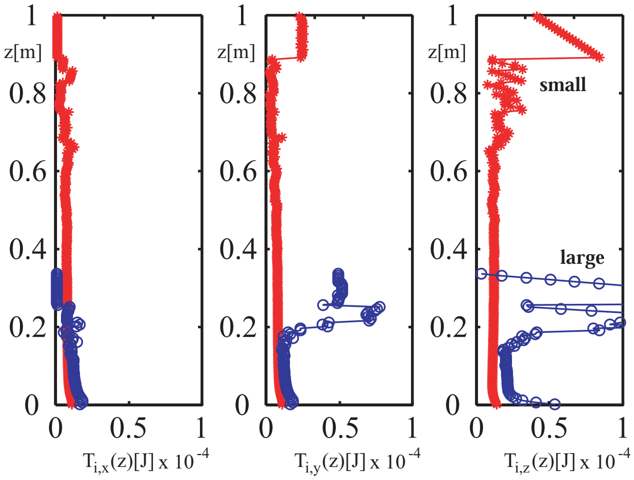

Figure 4.7: The x, y and z components of the granular temperature for the bidisperse mixture of Figure 4.5, $\psi = 2$. These temperature components are directly proportional to the kinetic energies of the particles: $T_{i,x} = \frac{1}{3} m_i v_{i,x}^2$, etc. ($i = 1, 2$ denoting the large and small particles, respectively).

In the uppermost region (above $z = 0.9$ m in Figure 4.7) we see the ballistic behavior of an individual small particle that freely travels upward, reaches the top (velocity in the z direction becomes zero at $z = 1.10$ m, outside the plot) and goes down again. The velocity components in the x and y direction remain practically constant during this parabolic flight [21]. A ballistic regime is also apparent in the temperature profiles of the larger particles: two parabolic flights that go considerably higher than the rest of the large particles and are not thwarted by the surrounding small ones are clearly visible in Figure 4.5 (and Figure 4.7) around $z = 0.22 - 0.35$ m. Indeed, the pronounced increase of the large-particle temperature toward the top of their range is due to the the fact that the large particles observed at these heights are the ones that have chanced to fly up straight from the bottom, with no (or very few) collisions on the way up. The increase of the temperature profile here thus roughly reflects the temperature peak at the bottom.

The simulations show that the large particles have a higher temperature than the small ones, in agreement with the results found in the recent literature on this subject [15–20]. In Figure 4.8 the temperature ratio T_1/T_2 as estimated from our MD simulations, is given as a function of the size ratio

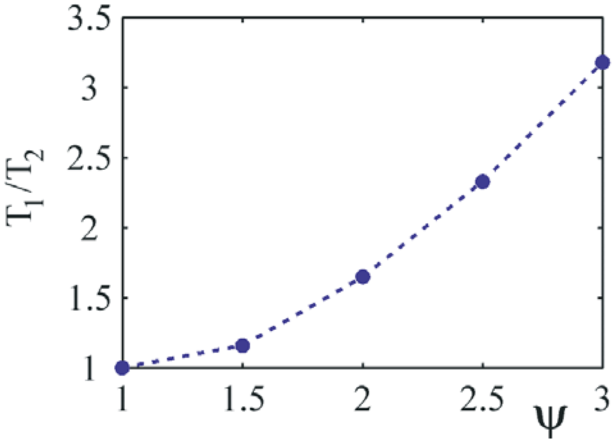

Figure 4.8: Temperature ratio T_1/T_2, determined from MD simulations, as function of the size ratio $\psi = r_1/r_2$. The values are taken at $z = 0.075$ m, which lies in the "constant" part of the large-particle temperature profile for each ψ.

$\psi = r_1/r_2$. The values in this plot hold at a height where the temperature profiles of both species are approximately constant; in the present case we have chosen z =0.075 m for each value of ψ. They can be read off directly from the temperature profiles (see Figures 4.4-4.6), or indirectly from the density profiles, by using the following relation between the slopes [from the barometric height equation (4.1)] :

$$\frac{\text{slope large-particle profile}}{\text{slope small-particle profile}} = \frac{m_1 T_2}{m_2 T_1} = \psi^3 \, \frac{T_2}{T_1}. \tag{4.2}$$

Both methods yield the same value for the temperature ratio.

In summary, we find that both species are not in equilibrium with the same granular temperature unless their mass ratio is one. On the other hand, even for $\psi = 2$, where the corresponding mass ratio m_1/m_2 is 8, the temperature ratio is still less than 1.7. Here the assumption of energy equipartition (with $T_1/T_2 = 1$) is still a meaningful first approximation.

4.3 Flux model

4.3.1 Basic equations and approximations

The flux model describes the flow of large and small particles between the compartments, as a function of the particle numbers in each compartment and of the shaking strength. It is a bidisperse generalization of Eggers' model for a monodisperse granular gas [8]. For its derivation we first consider the gas in a single compartment and from its steady state behavior determine the so-called *flux function*, i.e., the number of particles of each species that leaves the compartment per unit time [22]. In order to keep the model transparent, we make several strong approximations that are highlighted below. Even though these approximations seemingly bypass the state of the art in granular gas dynamics, the resulting model is definitely sufficient to account for our experimental and numerical observations on competitive clustering.

Barometric height distribution: The particles in each compartment are taken to obey the following equation of state [23]:

$$p_i = n_i k_B T_i \ , \tag{4.3}$$

(the ideal gas law, with $k_B = 1$ in the present context) and the momentum balance

$$\frac{dp_i}{dz} = -m_i g n_i \ , \tag{4.4}$$

for both species $i = 1, 2$ separately. Combining these two equations under the assumption that the granular temperature $T_i = (m_i/3k_B)\langle v_i \rangle^2$ is independent of z gives $k_B T_i dn_i/dz = -m_i g n_i$. Integration gives the barometric height formula:

$$n_i(z) = n_i(0) e^{-m_i g z / k_B T_i} \ . \tag{4.5}$$

In the previous Section we saw that this exponential distribution describes the real situation remarkably well, given the fact that both the ideal gas law (4.3) and the assumption that T_i is independent of z only hold in an approximate sense. One might make the agreement even better by using a more refined equation of state [24–26] and by letting T vary with z [27], but this would make an analytical expression for the flux function very difficult (if not impossible) while not affecting the resulting height distribution too much.

Energy equipartition: The assumption that both species have the same granular temperature ($T_i = T$ for $i = 1, 2$) strictly speaking means that we confine ourselves to size ratios ψ close to 1, see Figure 4.8. Nevertheless, also for $\psi = 2$ and even for $\psi = 3$ the model turns out to give results that closely agree with our experiments and MD simulations. This implies that the inequality of T_1 and T_2 does not play an essential role in the competitive clustering effect and the assumption $T_1/T_2 = 1$ may thus be viewed as an application of Occam's razor in order to keep the theory as simple as possible.

The density at ground level in equation (4.5) follows from the condition $\Omega \int_0^\infty n_i(z)dz = N_i$:

$$n_i(0) = \frac{m_i g N_i}{\Omega k_B T}, \tag{4.6}$$

where N_i is the number of particles (of species i) in the compartment under consideration and Ω is its ground area.

The temperature T should be interpreted as an average value for the whole compartment. Its value is determined by balancing the energy input via the vibrating bottom and the energy loss through the inter-particle collisions (both per unit of time):

$$J_0 = \Omega \int_0^\infty q(z)dz. \tag{4.7}$$

Here J_0 is the energy input rate and $q(z)$ is the dissipation rate per volume. We now calculate these two quantities in order to obtain the granular temperature T of the particles in the compartment. For the sake of simplicity we neglect the energy loss resulting from collisions with the wall, i.e., we treat those collisions as being completely elastic.

4.3.2 Energy input

The energy input comes from collisions of the particles with the bottom. For simplicity, we assume a sawtooth motion of the bottom, such that colliding particles always find it moving upwards with velocity $v_b = 2af$. The peak-to-peak amplitude $2a$ is taken to be sufficiently small compared to the mean free path of the particles, so that the bottom is effectively stationary.

Thus, when a particle with downward vertical velocity component v_{zi} collides with the bottom, it is reflected back with an upward vertical velocity of $|v_{zi}|+2v_b$. The energy gain per collision is equal to the difference in kinetic energy before and after collision, i.e.,

$$\Delta E_{kin} = 2m_i v_b(|v_{zi}| + v_b) \ . \tag{4.8}$$

To obtain the total energy input rate, this expression must be multiplied by the number of collisions per unit time, which is $\frac{1}{2}n_i(0)|v_{zi}|\Omega$ for each species (with the factor $\frac{1}{2}$ representing the fact that half of the particles have a downward vertical velocity component) and averaged over all possible v_{zi}. Now, let us assume that the velocity distribution is Maxwellian and isotropic. This is an approximation again (both with respect to the Maxwellian nature [33, 34] as to the isotropy, see Figure 4.7) to keep the model as simple as possible. It allows us to set $\langle v_{zi}^2 \rangle = \frac{1}{3}\langle v_i^2 \rangle = k_B T/m_i$ and $\langle |v_{zi}| \rangle = \sqrt{2k_B T/\pi m_i}$, yielding the following expression for the rate of energy input:

$$J_0 = \Omega \sum_{i=1,2} n_i(0) \left(v_b k_B T + \sqrt{\frac{2}{\pi}} v_b^2 \sqrt{m_i k_B T} \right) \ . \tag{4.9}$$

This equation can easily be generalized to two different temperatures T_i for the species $i = 1, 2$, but we will not do so here. Since the velocity of the bottom v_b is typically much smaller than the velocity of the particles ($v_b \ll v_i$), the first term in equation (4.9) is much larger than the second, which we therefore neglect. The energy input then becomes:

$$\begin{aligned} J_0 &= \Omega v_b k_B T \left(n_1(0) + n_2(0) \right) \\ &= g v_b \left(m_1 N_1 + m_2 N_2 \right) , \end{aligned} \tag{4.10}$$

where in the last step we have used equation (4.6).

4.3.3 Energy loss

To evaluate $q(z)$, the dissipation rate per volume, we consider a particle of mass m_i and velocity $\mathbf{v_i}$ travelling through a bidisperse background. If it collides with another particle of mass m_j and $\mathbf{v}_j$ the energy loss will be, on the average (i.e., averaged over the collisional cross-section):

$$E_{loss} = \frac{1}{4} \frac{m_i m_j}{m_i + m_j} (1 - \epsilon^2) \left(\mathbf{v}_i - \mathbf{v}_j \right)^2 \ , \tag{4.11}$$

which happens to be precisely *half* of the energy loss in a frontal collision.

A collision will happen (within a time interval dt) if either of the two particles finds itself in the cross-sectional volume of the other, which is a cylinder of length $|\mathbf{v}_i - \mathbf{v}_j| dt$ and front area $\pi(r_i + r_j)^2$. Hence the collision rate per volume is the product of the particle densities $n_i(z) n_j(z)$ and this cross-sectional volume divided by dt, where we assume that the densities do not vary significantly over this volume.

The dissipation rate per volume $q(z)$ is found by multiplying the collision rate per volume with the energy loss (4.11) and averaging over all possible realizations of the independently distributed velocities $\mathbf{v}_i$ and $\mathbf{v}_j$:

$$q(z) = \frac{1}{8}(1 - \epsilon^2) \times \tag{4.12}$$

$$\sum_{i,j=1}^{2} n_i(z)n_j(z)\pi(r_i+r_j)^2 \frac{m_i m_j}{m_i+m_j}\left\langle|\mathbf{v}_i-\mathbf{v}_j|^3\right\rangle \ ,$$

where we have multiplied by an additional factor $\frac{1}{2}$ to balance the fact that in this procedure we count every collision twice.

To evaluate the ensemble average $\langle|\mathbf{v}_i-\mathbf{v}_j|^3\rangle$, we note that – under the assumption of Maxwellian velocity distributions – all of the components of $\mathbf{v}_i$ and $\mathbf{v}_j$ are distributed Gaussian with variances (i.e., squared standard deviations) $\sigma_i^2 = k_B T/m_i$ and similarly for σ_j^2. Again, it is possible to generalize this to two different temperatures T_i for the species $i = 1, 2$, but here we will continue to work with $T_1 = T_2 = T$.

It follows that the components of the combined variable $\mathbf{u}_{ij} \equiv (\mathbf{v}_i - \mathbf{v}_j)/\sqrt{2}$ are also Gaussian, with zero mean and its variances are found by adding those of the (independently distributed) constituents $\mathbf{v}_i$ and $\mathbf{v}_j$ and dividing by 2: $\sigma^2 = k_B T/2m_i + k_B T/2m_j$. The distribution function $P(\mathbf{u}_{ij})$ thus equals

$$\begin{aligned} P(\mathbf{u}_{ij}) &= \frac{1}{(2\pi\sigma^2)^{3/2}}\, e^{-u_{ij}^2/2\sigma^2} \qquad (4.13)\\ &= \left(\frac{m_i m_j}{(m_i+m_j)\pi k_B T}\right)^{3/2} \exp\left\{\frac{-m_i m_j u_{ij}^2}{(m_i+m_j)k_B T}\right\}, \end{aligned}$$

where $u_{ij} = |\mathbf{u}_{ij}|$, and with this we can calculate:

$$\begin{aligned} \langle|\mathbf{v}_i-\mathbf{v}_j|^3\rangle &= 2\sqrt{2}\ \langle|\mathbf{u}_{ij}|^3\rangle \\ &= 8\pi\sqrt{2}\int_0^\infty u_{ij}^5 P(u_{ij})du_{ij} \\ &= \frac{16}{\sqrt{2\pi}}\left(\frac{k_B T(m_i+m_j)}{m_i m_j}\right)^{3/2} . \qquad (4.14) \end{aligned}$$

Inserting this expression in equation (4.12) we find:

$$\begin{aligned} q(z) &= \sqrt{2\pi}(1-\epsilon^2)(k_B T)^{3/2} \times \\ &\quad \sum_{i,j=1}^{2} n_i n_j\,(r_i+r_j)^2\left(\frac{m_i+m_j}{m_i m_j}\right)^{1/2} \\ &= 8\sqrt{\pi}(1-\epsilon^2)(k_B T)^{3/2} \times \\ &\quad \left(\frac{n_1^2 r_1^2}{\sqrt{m_1}} + \frac{n_2^2 r_2^2}{\sqrt{m_2}} + \frac{n_1 n_2 (r_1+r_2)^2}{2\sqrt{2}\sqrt{m_{12}}}\right), \qquad (4.15) \end{aligned}$$

with $m_{12} = m_1 m_2/(m_1 + m_2)$ the so-called reduced mass. The energy dissipation rate Q now follows by integrating $q(z)$ over the whole volume of the compartment:

$$Q = \Omega \int q(z)dz = \sqrt{2\pi}(1-\epsilon^2)(k_B T)^{3/2} \times \tag{4.16}$$
$$\sum_{i,j=1}^{2} (r_i + r_j)^2 \left(\frac{m_i + m_j}{m_i m_j}\right)^{1/2} \int_0^\infty n_i(z) n_j(z) dz \ .$$

The integral in the above expression is readily evaluated using equations (4.5) and (4.6):

$$\int_0^\infty n_i(z) n_j(z) dz = \frac{g}{\Omega^2 k_B T} \frac{m_i m_j}{m_i + m_j} N_i N_j \ , \tag{4.17}$$

with which we finally obtain:

$$Q = \frac{4\sqrt{\pi} g (1-\epsilon^2)}{\Omega} \sqrt{k_B T} \times \tag{4.18}$$
$$\left(\sqrt{m_1} r_1^2 N_1^2 + \sqrt{m_2} r_2^2 N_2^2 + \sqrt{\frac{m_{12}}{2}} (r_1 + r_2)^2 N_1 N_2\right) .$$

4.3.4 Granular temperature

Equating the two expressions for the rate of energy input (equation (4.10)) and energy loss (equation (4.18)) yields the following expression for the granular temperature T of the compartment:

$$k_B T = \frac{(2af)^2 \mu}{16\pi (1-\epsilon^2)^2} \ , \tag{4.19}$$

where the effective mass μ is given by:

$$\mu(N_1, N_2) = \tag{4.20}$$
$$\left(\frac{\Omega(m_1 N_1 + m_2 N_2)}{r_1^2 \sqrt{m_1} N_1^2 + r_2^2 \sqrt{m_2} N_2^2 + (r_1 + r_2)^2 \sqrt{\frac{1}{2} m_{12}} N_1 N_2}\right)^2 .$$

with $m_{12} = m_1 m_2/(m_1 + m_2)$. It is through this quantity μ that the particle numbers of the two species enter the temperature. One may check that in the monodisperse limit ($r_1 = r_2 = r$, $m_1 = m_2 = m$) it reduces to $\mu_{\psi=1} =$

$\Omega^2 m/[r^2(N_1+N_2)]^2 = m\{\pi\Omega/\text{total projected area of the particles}\}^2$, i.e., the particle mass divided by the square of a dimensionless filling factor.

The temperature from equation (4.19) compares well with the temperatures T_1 and T_2 of the large and small particles in the MD simulations of Figures 4.4-4.6. Indeed, for $\psi = 2, 3$ one finds the temperature from equation (4.19) to be in between T_1 and T_2. It is slightly *larger* (about 10%) than the weighted average of T_1 and T_2, as can be understood from the idealizations in the model. E.g., the model does not take into account the dissipation from the particle-wall collisions and assumes a sawtooth driving instead of the sinusoidal driving used in the simulations.

4.3.5 Flux function

The central quantity of the model is the flux function F_i, defined as the number of particles (of species i) that leaves the compartment per unit time. It is the product of half the density $\frac{1}{2}n_i(z)$ (so that we count particles moving in one direction only) and the average horizontal velocity (which is equal to $\sqrt{2k_BT/\pi m_i}$) integrated over the space above the wall (width b) from $z = h$ to some cut-off height $h + H$. Above the cut-off height, the state variables of the two compartments are in equilibrium and hence no net flux occurs. In principle, H will depend on the mean free path of the particles, but here we take it to be constant. The integration is then straightforward [28]:

$$\begin{aligned} F_i(N_1, N_2) &= \frac{1}{2}\sqrt{\frac{2k_BT}{\pi m_i}}\, b\int_h^{h+H} n_i(z)dz \\ &= \sqrt{\frac{k_BT}{2\pi m_i}}\frac{bN_i}{\Omega}e^{-m_igh/k_BT}\left(1-e^{-m_igH/k_BT}\right) \\ &\approx KN_i\sqrt{\frac{m_i}{\mu}}e^{-Dm_i/\mu} \quad , \quad i=1,2. \end{aligned} \tag{4.21}$$

In the last step we have linearized $\exp(-m_igH/k_BT)$, implying that $H \ll \langle v_i^2\rangle/g$, and expressed k_BT in terms of the particle numbers N_i by means of equations (4.19)-(4.20). The prefactor K determining the absolute rate of the flux is given by [29]:

$$K = 2\sqrt{2}(1-\epsilon^2)\frac{gbH}{\Omega(2af)}, \tag{4.22}$$

and the dimensionless parameter D, which governs the clustering behavior, has the form

$$D = 16\pi\frac{gh}{(2af)^2}(1-\epsilon^2)^2. \tag{4.23}$$

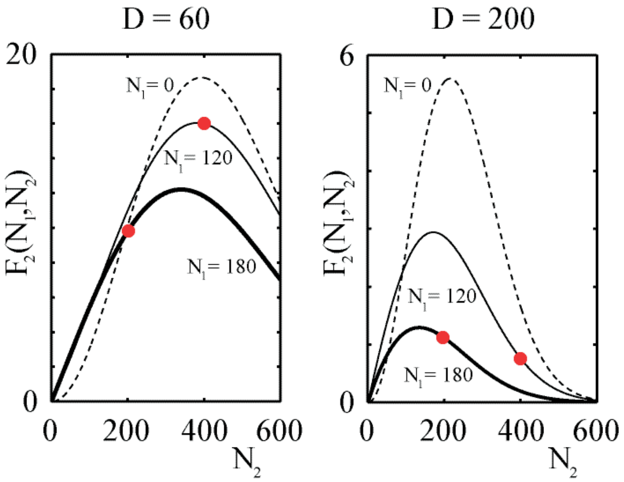

Figure 4.9: The small-particle flux $F_2(N_1, N_2)$ as a function of N_2, for various numbers of large particles in the compartment: $N_1 = 0$ (dashed), $N_1 = 120$ (thin), and $N_1 = 180$ (thick). For $D = 60$ (relatively strong shaking; left plot) the flux from a compartment with {180 large, 200 small} particles (indicated by the left dot) is smaller than from a compartment with {120 large, 400 small} particles (right dot). Hence the clustering is towards the former compartment, i.e. type I clustering, in agreement with the experimental observation of Figure 4.2. For $D = 200$ (weak shaking; right plot) it is the other way around, leading to type II clustering, again in agreement with experiment. The "tennis ball on basketball effect" is most pronounced on the left flank of the flux function, where the small-particle flux from the compartment actually *rises* (with respect to the dashed curve) upon adding large particles. Note the different scales of the vertical axis in the two plots: the stronger the shaking, the higher the particle flux.

The influence of the large particles on the small-particle flux (and vice versa) is contained in the parameter μ, given by equation (4.20).

In Figure 4.9 we show the small-particle flux $F_2(N_1, N_2)$ as a function of N_2, at $D = 60$ (relatively strong shaking) and $D = 200$ (weak shaking) respectively, for three different values of the number of large particles N_1.

For $N_1 = 0$ (*no* large particles in the compartment, dashed curve) the flux function has the well-known monodisperse form studied in [8, 9, 30, 31]. It starts out from zero at $N_2 = 0$ (expressing the fact that there is no particle flux from an empty compartment) and initially increases with growing N_2. For any ordinary molecular gas it would always keep increasing, but for a granular gas it is seen to reach a maximum and goes down again: The inelastic collisions (which become more and more frequent as N_2 grows) make the particles slow, until they are hardly able to jump over the wall anymore and the flux $F_2(0, N_2)$ approaches zero in the limit for $N_2 \to \infty$.

For $N_1 = 120$ (thin curve) and $N_1 = 180$ (thick curve) the maximum of the flux function decreases as compared to the situation without large particles (dashed curve), due to the much larger total mass in the compartment. However, on the left flank there is a region where the drawn curves are actually *higher* than the dashed one. This is an illustration of the "tennis ball on basketball effect" mentioned earlier, with the small particles becoming more mobile thanks to the presence of the larger ones.

One can deduce the type of clustering that results from the plots in Figure 4.9. Let us start, just as in the experiments of Figure 4.2, with {180 large, 200 small} particles in one compartment (A) and {120 large, 400 small} particles in the other (B). In the left plot, for $D = 60$, we see that the flux from compartment A (indicated by the left dot) is smaller than from compartment B (right dot). Hence the direction of clustering is towards A, i.e., type I clustering, in agreement with the experimental observation of Figure 4.2 (see also Figure 4.10). In the plot for $D = 200$ it is precisely the other way around, resulting in type II clustering, again in agreement with experiment. Note also the different scales along the vertical axis in the two plots: The flux function is considerably smaller for weak shaking, confirming the fact that the clustering process takes much longer there.

With the above flux function we are now in a position to calculate the dynamics of our two-compartment system starting from any initial condition and for any shaking strength. The evolution of the number of particles N_{iA} in compartment A ($i = 1, 2$) is given by the net balance between the (outgoing) flux from A to B and the (incoming) flux from B to A:

$$\begin{aligned} \frac{dN_{iA}}{dt} &= -F_i(N_{1A}, N_{2A}) + F_i(N_{1B}, N_{2B}) \\ &= -F_i(N_{1A}, N_{2A}) + F_i(P_1 - N_{1A}, P_2 - N_{2A}) \ , \end{aligned} \tag{4.24}$$

where we have used particle conservation, $N_{iA} + N_{iB} = P_i$. The evolution of the (complementary) particle numbers in compartment B is governed by the same equation with A and B interchanged.

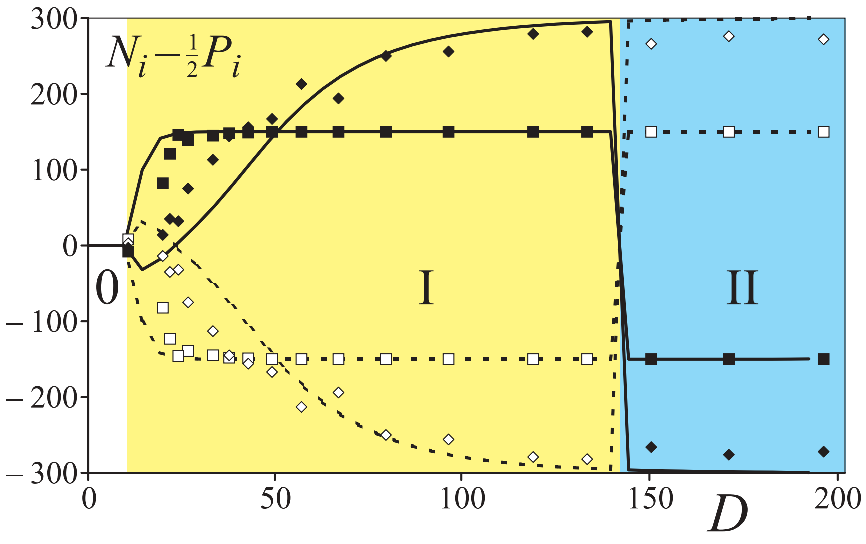

Figure 4.10: Bifurcation diagram comparing the three different regimes 0, I, and II, as obtained from experiments and the flux model. The same setup and parameters as in Figure 4.3 are used and the particle numbers N_i $(i = 1, 2)$ are given relative to the symmetric solution: $N_i - \frac{1}{2}P_i$. The curves represent the steady state according to the theoretical flux model and the squares and diamonds are experimental data presented in Figure 4.3. The squares correspond to the large beads and the diamonds to the small ones. Solid symbols refer to compartment A, and open symbols to B; note that every measurement is thus represented by two points, which accounts for the mirror-symmetry of the plot in the vertical direction.

4.4 Comparing the flux model, experiment, and MD simulations

4.4.1 Competitive clustering for size ratio $\psi = 2$

The predictions from the flux model, calculated from equations (4.21)-(4.24), are found to be in good quantitative agreement with our experimental results which were shown in Figure 4.3. In Figure 4.10 we compare model predictions and experimental data for a mixture of $P_1 = 300$ large and $P_2 = 600$ small steel beads, with size ratio $\psi = 2$, starting always from the same initial situation:

$$\begin{aligned} \{N_{1A}(0), N_{2A}(0)\} &= \{180, 200\} \quad \text{in compartment A,} \\ \{N_{1B}(0), N_{2B}(0)\} &= \{120, 400\} \quad \text{in compartment B.} \end{aligned} \tag{4.25}$$

Both in the model and in experiment we recover the three different regimes observed in the Introduction: For vigorous shaking (regime O, $D < 10$) the system quickly settles into a symmetric state with equal amounts of small and large particles in both compartments. At moderate shaking (regime I, $10 < D < 140$) the clustering takes place in compartment A, the one initially containing the majority of large particles. This regime has been indicated by a light gray shading in Figure 4.10 and in all figures that follow. At even milder shaking (regime II, $D > 140$) the clustering takes place in compartment B; for this regime we use a darker shading.

The time scale of the clustering grows with increasing D. This is illustrated in Figure 4.11, where the evolving particle numbers $N_{iA}(t)$ and $N_{iB}(t)$ (evaluated by the flux model) are given at $D = 100$ and 200, respectively. In the first case the clustering is complete already after 150 s, whereas in the latter case it takes almost a hundred times as long. In agreement with our experimental observations the small particles cluster first and only when nearly all of them have reached their final destination do the large ones follow. The clustering times obtained from the flux model are in reasonable agreement with the experimental observations, including a sudden jump in the time scale at the transition from type-I to type-II clustering: Just before the transition the clustering (into box A) is experimentally found to be about 10 times as fast as just after the transition (into box B). This jump is also found in the time scales evaluated from the flux model.

In order to see what causes the transition from regime I to II, we make flow diagrams (see Figure 4.12) that show how the particle numbers $N_{1B}(t)$ and $N_{2B}(t)$ in compartment B evolve for any initial condition. The arrows indicate the dynamics of the system and the cross denotes the initial condition that was used in the experiments (specified in equation (4.25)).

For very strong shaking (Figure 4.12a, $D = 1$) only one fixed point exists: the stable uniform distribution $\{150, 300\}$ in the center of the flow diagram. The system quickly approaches this point regardless of the initial condition.

At $D = 20$, just beyond the pitchfork bifurcation, the homogeneous state has become unstable and has given way to two new stable fixed points. These correspond to compartment B being either comparatively empty (fixed point in the lower part of the flow diagram, type I clustering) or well filled (upper part, type II). The basins of attraction for these two points are indicated by the shading: Any initial condition in the light gray region will lead to a cluster in box A, while initial conditions lying in the dark region lead to a cluster in box B. The initial condition for the experiments of Figure 4.10 (indicated by the cross) lies in the light gray basin, so this one leads to a cluster in compartment A. The arrows indicate that first the small particles

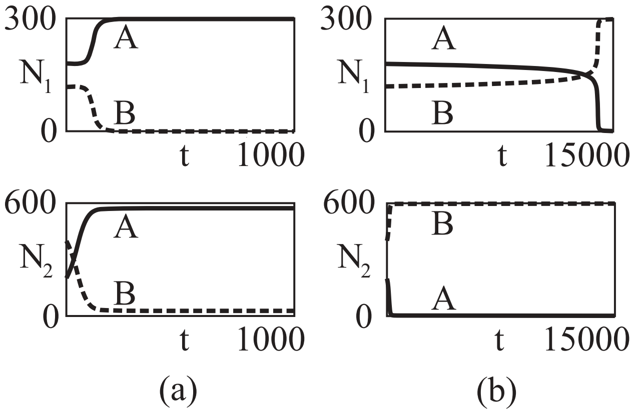

Figure 4.11: Evolution of the system calculated from the flux model, starting from the initial condition equation (4.25), for (a) $D = 100$ (type-I clustering) and (b) $D = 200$ (type-II clustering). The solid curves represent the number of particles in compartment A, the dashed ones compartment B. It is seen that the small particles (lower row) cluster first, followed by the large ones (top row). Note the different time scales between type-I and type-II clustering.

settle into their preferred distribution over the compartments and that the large ones follow later (as we also noted in the plots of Figure 4.11). At this relatively small value of D the small beads are still divided over the two compartments, but the large beads already cluster heavily: This is in agreement with the bifurcation diagram of Figure 4.10.

For $D = 80$ the clustering has become much more pronounced, since also the small beads accumulate into the same compartment. We furthermore note that the boundary between the two basins of attraction has shifted and is now almost horizontal.

At very mild shaking ($D = 200$), the boundary between the two basins of attraction has shifted again. The initial condition (the cross) now lies within the dark basin of attraction and we end up with nearly all particles in compartment B. The same plot shows that the fixed points move further into their corners for increasing D, i.e., the clustering becomes more pronounced for decreasing shaking strength. This feature was apparent already in Figure 4.2, and has been observed earlier also for clustering in a monodisperse gas, i.e., for $\psi = 1$ [8, 9].

Interestingly the boundary between the two basins of attraction is found to move (as function of D) in a non-monotonic fashion. From $D = 20$ to

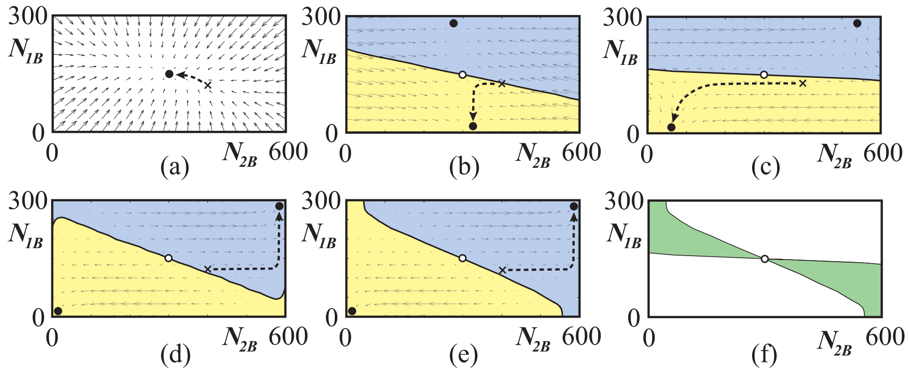

Figure 4.12: Flow diagrams calculated from the flux model (for the same system as in Figures 4.10 and 4.11) showing how the contents of compartment B evolve at five successive values of the shaking parameter: (a) D =1, (b) D =20, (c) D =80, (d) D =200, and (e) D =250. The cross indicates the initial condition used in the experiments: $\{N_{1B}(0), N_{2B}(0)\}$={120, 400}. At D=1 there is no clustering and all initial conditions lead to the uniform distribution (the central point in the flow diagram). For $D = 20, .., 250$ all initial conditions in the light gray basin of attraction lead to a comparatively empty compartment B (type-I clustering) and those in the dark basin of attraction lead to a well-filled compartment B (type-II clustering). Note that the slope of the boundary between the two regimes shows non-monotonic behavior as function of D. Figure (f) shows the region of *competitive* clustering (gray): The boundary between the two basins of attraction in Figures (a)-(e) sweeps through this region and therefore the initial conditions here lead to either type-I or type-II clustering depending on the value of D.

$D = 80$ it is seen to straighten out towards an almost horizontal position, but from $D = 80$ onwards it starts to slant again and at the same time develops a curve. At some point between $D = 200$ and $D = 250$ it goes through the diagonal position and eventually seems to come to a standstill. We shall not pursue the limit for very high values of D, however, since here the shaking becomes so weak that no particles are able to jump over the wall anymore: Any clustering predictions in this limit will no longer be reproducible in experiments or MD simulations.

The motion of the basin boundary shows that competitive clustering does not occur for *all* initial situations: Only a set of conditions in the lower right quadrant and (equivalently) the upper left quadrant can be directed into either compartment by tuning the shaking strength. On the other hand, there is also a region through which the boundary sweeps twice, so here we find *two* consecutive transitions between the clustering regimes I and II as

D is varied. The initial condition used in the experiment lies just outside this double transition region; had it been chosen slightly differently, the bifurcation diagram of Figure 4.10 would have had an additional band of type-II clustering between regimes O and I. The twist in the small-particle curve immediately after the pitchfork bifurcation at D=20 is a "ghost" of this band.

4.5 Exploring the parameter space: Dependence on size ratio (ψ) and relative abundance of large and small particles (σ)

4.5.1 Size ratio ψ

How do the above observations generalize to size ratios $\psi = r_1/r_2$ different from 2 ? This ratio has a marked effect on the critical D values where the transition from the regimes O, I, and II take place. In Figures 4.13 and 4.14 we show the position of these regimes as a function of ψ and D, for the same initial condition that was specified in equation (4.25). The drawn curves have been calculated from the flux model and the symbols are data from experiments (Figure 4.13) and MD simulations (Figure 4.14). The vertical dashed line in Figure 4.13 corresponds to the case $\psi = 2$ studied in the previous subsection.

It is seen that for $\psi < 1.5$ the transition from regime O to regime II is immediate: here the larger beads are not sufficiently big to compensate for the fact that they are a minority. It is the larger number of beads that decides where the cluster goes, just as for the mono-disperse case ($\psi = 1$). On the other hand, for high values of ψ, the dominant size of the large beads always makes *them* the decisive factor (only regime I survives). It is precisely the intermediate region $1.5 < \psi \lesssim 2.3$ in which the competition takes place: The curving border between regimes I and II indicates the critical value of D where the basin boundary sweeps through our initial condition (4.25). For $\psi \approx 1.6$ the boundary sweeps twice through this initial condition and we witness the particularly interesting sequence 0-II-I-II, both in the model and in experiment.

Both in experiment (Figure 4.13) and in the MD simulations (Figure 4.14) the actual border between regimes I and II is found to lie more to the right than predicted by the flux model. This shift of the borderline means that the "counterintuitive" type-II clustering is even stronger than predicted by the flux model. This may be understood from the fact that the mobility

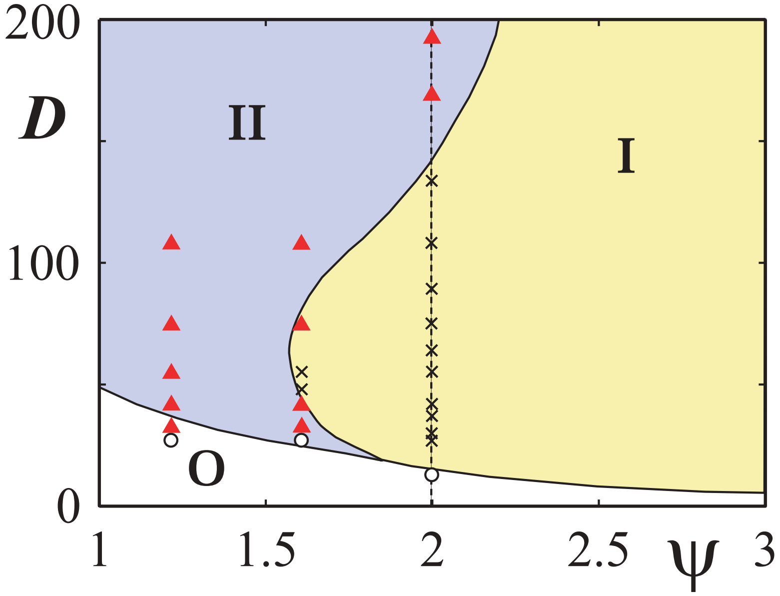

Figure 4.13: Phase diagram showing the three clustering regimes as a function of the inverse shaking strength D and the size ratio $\psi = r_1/r_2$. The drawn curves are calculated from the flux model and the symbols correspond to experiments: ∘ : no clustering, × : type-I clustering, and ▲ : type-II clustering. The experimental results on the vertical dashed line $\psi = 2$ corresponds to the results illustrated in Figure 4.10. The initial condition is always taken to be as in equation (4.25).

of the large beads is underestimated by the flux model, which assumes the granular temperatures for the large and the small beads to be equal. In reality (in experiments and MD simulations) the temperature of the large ones is known to be higher and therefore the type-II scenario in which the majority of large beads switches compartment occurs somewhat easier than suggested by the flux model.

4.5.2 Relative abundance σ

In the experiments and simulations so far we have always used mixtures in which the number of large particles was half the number of small ones: $\sigma = P_1/P_2 = 1/2$. Let us now have a brief look at other compositions,

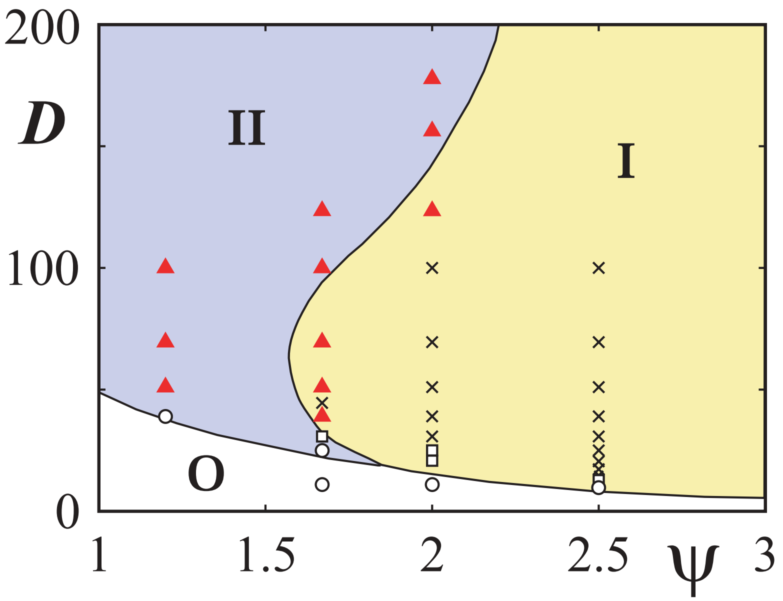

Figure 4.14: The same phase diagram as in Figure 4.13, for the same initial situation (4.25), but this time the symbols represent MD simulations. Between the regimes of type-I and type-II clustering there is also a zone where the clustering in the MD simulations can go either way depending on statistical fluctuations. This undecided state of affairs is indicated by the open squares, □ : Each of them is based on 10 repetitions of the MD simulation, of which typically half ended in type-I clustering and the other half in type-II. As in all previous figures the ratio of large to small particles is $\sigma = P_1/P_2 = 300/600 = 1/2$.

since obviously this parameter σ must have an important influence on the clustering behavior: A larger value of σ means that the large beads become a more important minority (or even a majority for $\sigma > 1$) and hence type-I clustering will gain ground. This is indeed the case as illustrated by Figure 4.15 for $\sigma = 1/6$ and 1. The initial condition we use here ($\{\frac{3}{5}P_1, \frac{1}{3}P_2\}$ in compartment A and $\{\frac{2}{5}P_1, \frac{2}{3}P_2\}$ in compartment B) is equivalent to the one taken in all previous experiments and simulations (equation (4.25)), but due to the change in P_1 and P_2, the absolute number of particles initially inserted into the two compartments are different.

The position of all the lines (i.e., transitions) in the phase diagram are affected by the changing particle numbers. Take e.g. the value of D at which the transition from regime O to II occurs in the monodisperse limit

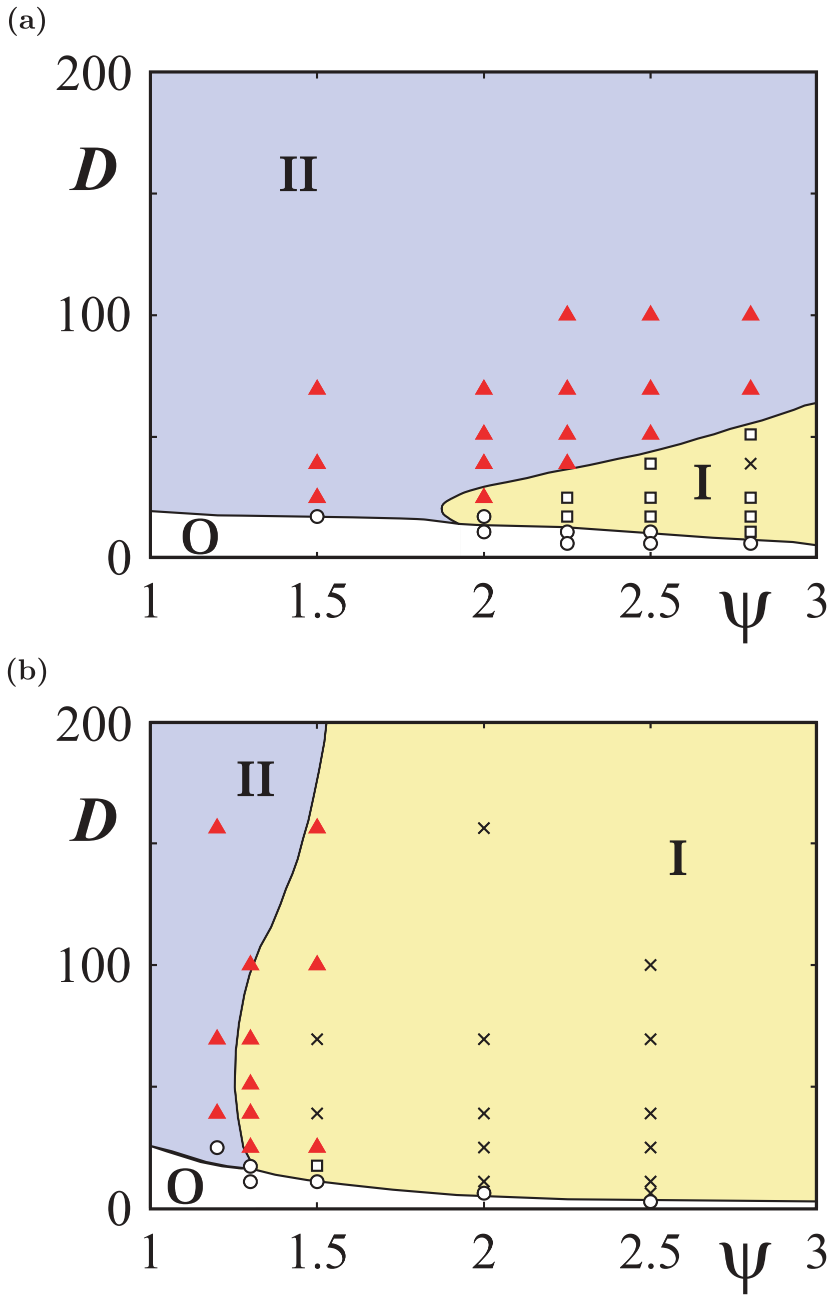

Figure 4.15: The same as Figure 4.14, but now for (a) $\sigma = P_1/P_2 = 200/1200 = 1/6$ and (b) $\sigma = 600/600 = 1$. For growing σ (relative abundance of the large particles) type-I clustering clearly gains ground. The initial condition used here is $\{\frac{3}{5}P_1, \frac{1}{3}P_2\}$ in compartment A and (hence) $\{\frac{2}{5}P_1, \frac{2}{3}P_2\}$ in compartment B, in analogy with the condition (4.25) which was taken in all previous figures (where $\sigma = 300/600 = 1/2$).

$\psi = 1$. This clearly goes down as the total number of particles in the system increases: In Figure 4.14 (with $P_1 + P_2 = 900$) the critical D-value exceeds 40, while in Figure 4.15a (with $P_1 + P_2 = 1400$) it lies below 20. The physical reason for this is that the larger number of particles induces more collisions and hence the dissipation rate increases, so stronger shaking is necessary to obtain the homogeneous distribution. According to the monodisperse flux model [8, 9, 30] the critical D-value for $\psi = 1$ goes as

$$D_{c,\psi=1} \propto \frac{1}{(P_1 + P_2)^2} \; . \tag{4.26}$$

That is, the product of $D_{c,\psi=1}$ and $(P_1 + P_2)^2$ is exactly the same in all three plots of Figures 4.14 and 4.15a,b.

The border between the two clustered states (regime I and II) is affected even more drastically. Particularly the band of ψ values where both clustering types can be obtained by adjusting the shaking strength (competitive clustering) depends strongly on σ. For $\sigma = 1$ it is confined to the narrow band of values $1.2 < \psi < 1.5$. Here regime I dominates the phase diagram and the borderline between type-I and type-II clustering is pushed towards the vertical axis at $\psi = 1$.

For decreasing σ the same borderline moves towards the right and bends down, thereby reducing regime I and broadening the band of competitive clustering. Indeed, in Figure 4.15a for $\sigma = 1/6$, there is only one point (indicated by the cross) which consistently gave type-I clustering in our MD simulations. It is surrounded by a number of points for which the clustering was undecided, sometimes going in one direction and sometimes in the other; this is a manifestation of statistical fluctuations, which are not taken into account in our mean field approach [32]. Not surprisingly, given the relatively large values of ψ in this region (and the associated deterioration of the one-temperature assumption, see Figure 4.8) the simulations do not precisely follow the predictions of the flux model here. Nevertheless, the general trend of the phase diagram is still well reproduced.

4.6 Conclusion

The main conclusion of this work is that experiment, theory, and numerics all agree on the phenomenon of competitive clustering in a bidisperse granular gas: The clustering can be directed either towards the compartment initially containing the majority of large particles (type-I clustering) or to the one containing mainly small particles (type-II) simply by adjusting the shaking strength.

The best quantitative agreement with the theoretical flux model is found when the size ratio between the large and small particles (ψ) is not too much larger than 1. This can be traced back to the fact that in the model the granular temperatures T_1 and T_2 are assumed to be equal, which is an accurate assumption only for ψ close to 1. Since the region of competitive clustering is found to move closer and closer towards $\psi = 1$ if we let the number of large particles grow (see Figure 4.15), this means that the theory works best for comparatively large numbers of large particles.

For smaller large-particle numbers the region of competitive clustering in the phase diagram is pushed towards higher ψ values. The theoretical description here becomes less accurate, but still shows the correct qualitative features. Our MD simulations show that in these regions the borderline between type-I and type-II clustering widens to a broad zone where the cluster can go in either direction.

References

[1] R. Mikkelsen, D. van der Meer, K. van der Weele and D. Lohse, Phys. Rev. Lett. **89**, 214301 (2002).

[2] I. Goldhirsch and G. Zanetti, Phys. Rev. Lett. **70**, 1619 (1993).

[3] H.M. Jaeger, S.R. Nagel, and R.P. Behringer, Rev. Mod. Phys. **68**, 1259 (1996).

[4] A. Kudrolli, M. Wolpert, and J.P. Gollub, Phys. Rev. Lett. **78**, 1383 (1997).

[5] L. Kadanoff, Rev. Mod. Phys. **71**, 435 (1999).

[6] I. Goldhirsch, Annu. Rev. Fluid Mech. **35**, 267 (2003).

[7] H.J. Schlichting and V. Nordmeier, Math. Naturwiss. Unterr. **49**, 323 (1996).

[8] J. Eggers, Phys. Rev. Lett. **83**, 5322 (1999).

[9] K. van der Weele, D. van der Meer, M. Versluis, and D. Lohse, Europhys. Lett. **53**, 328 (2001).

[10] J.J. Brey, F. Moreno, R. García-Rojo, and M.J. Ruiz-Montero, Phys. Rev. E**65**, 011305 (2001).

[11] J.L. Spradley, Am. J. Phys. **55**, 183 (1987); J.S. Huebner and T.L. Smith, Phys. Teacher **30**, 46 (1992).

[12] J. Schäfer, S. Dippel, and D.E. Wolf, J. Physique I **6**, 5 (1996).

[13] T. Schwager and T. Pöschel, Phys. Rev. E**57**, 650 (1998).

[14] V. Kumaran, Phys. Rev. E**57**, 5660 (1998).

[15] R.D. Wildman and D.J. Parker, Phys. Rev. Lett. **88**, 064301 (2002).

[16] K. Feitosa and N. Menon, Phys. Rev. Lett. **88**, 198301 (2002).

[17] V. Garzó and J. Dufty, Phys. Rev. E**60**, 5706 (1999).

[18] W. Losert, D.G.W. Cooper, J. Delour, A. Kudrolli, and J.P. Gollub, Chaos **9**, 682 (1999).

[19] A. Barrat and E. Trizac, Granular Matter **4**, 57 (2002).

[20] M. Alam and S. Luding, Granular Matter **4**, 139 (2002).

[21] For the highest parabolic flight in Figures 4.5 and 4.7c the z component of the velocity goes down from $v_z = 2.03$ m/s at $z = 0.89$ m to 0 m/s at $z = 1.10$ m, as the particle's vertical kinetic energy $\frac{1}{2}m_2v_z^2 (= \frac{3}{2}T_z)$ is converted into potential energy m_2gz. The constant values of the other components, $v_x = 0.36$ m/s and $v_y = 1.08$ m/s, can be read off from Figure 4.7a,b with $m_2 = \frac{4}{3}\pi\rho r_2^3 = 0.063$ g.

[22] An alternative theoretical approach to the clustering phenomenon in granular gases is the so-called hydrodynamic model introduced by Brey *et al.* in [10] and generalized to a bidisperse gas by Barrat and Trizac [19]. The two approaches are put side by side in K. van der Weele, R. Mikkelsen, D. van der Meer, and D. Lohse, Cluster Formation in Compartmentalized Granular Gases, in "The Physics of Granular Media", edited by H. Hinrichsen and D.E. Wolf (Wiley, Berlin, August 2004).

[23] The ideal-gas law normally applies for a gas with conservative (dissipationless) collisions and negligible excluded volume. Both these conditions are met reasonably well in the present system: (a) The coefficient of restitution $\epsilon = 0.85$ is not too different from 1, and (b) the gas is dilute enough to neglect excluded volume effects in first approximation. For more refined equations of state, see References [24–26].

[24] J.T. Jenkins and M.W. Richman, Phys. Fluids **28**, 3485 (1985).

[25] E.L. Grossman, T. Zhou, and E. Ben-Naim, Phys. Rev. E**55**, 4200 (1997).

[26] S. Luding, Phys. Rev. E**63**, 042201 (2001).

[27] J.J. Brey, M.J. Ruiz-Montero, and F. Moreno, Phys. Rev. E**62**, 5339 (2000); Phys. Rev. E**63**, 061305 (2001).

[28] Naively integrating up to $h \to \infty$ would lead to an (unphysical) non-zero flux for $N_i = 0$. To see this, consider a compartment without any type 2 particles: then $T \propto 1/N_1^2$ (from equations (4.19) and (4.20)) and hence F_1 loses its N_1 dependence in the dilute limit (cf. second line of equation (4.21)), making it non-zero for $N_1 = 0$.

[29] Because of a refinement in the flux model, the expressions for K and D differ slightly from the ones presented in [1]. Apart from a different scaling (in the parameter D) of the experiments onto the model, there are neither qualitative nor quantitative changes to the conclusions drawn in that paper.

[30] D. van der Meer, K. van der Weele, and D. Lohse, Phys. Rev. E**63** 061304 (2001).

[31] D. van der Meer, K. van der Weele, and D. Lohse, Phys. Rev. Lett. **88**, 174302 (2002).

[32] Statistical fluctuations in the context of compartmentalized clustering have recently been discussed by several authors, see e.g. [19] and U. Marini Bettolo Marconi and A. Puglisi, Phys. Rev. E**68**, 031306 (2003).

[33] J.J. Brey and M.J. Ruiz-Montero, Phys. Rev. E**67**, 021307 (2003).

[34] D. Paolotti, C. Cattuto, U. Marini Bettolo Marconi, and A. Puglisi, Granular Matter **5**, 75 (2003).

Chapter 5

Granular eruptions: void collapse and jet formation [§]

Abstract

Dropping a steel ball onto a bed of loose, very find sand creates an upward jet, which exceeds the release height of the ball. The jet is created as the crater formed by the impact collapses due to the sand pressure. For high impact velocities the void collapse is seen to entrain air beneath the surface. This air bubble slowly rises to the surface where it causes a granular eruption. These experimental observations are accounted for within a simple Rayleigh-type model.

5.1 Introduction

It has been known for a long time that jets can be created when a ball or fluid droplet impacts on a fluid surface [1–5]. Thoroddsen and Shen found related jets when a solid sphere impacts on a deep layer of monodisperse glass beads [6]. When we performed similar experiments on fine sand, we found it hard to achieve quantitatively reproducible results, presumably due to the sensitivity of the experiment to the initial packing density. In order to prepare a well-defined initial state, we have therefore decompactified and homogenized extremely fine sand by blowing air through it via a perforated

---

[§] See also: R. Mikkelsen, M. Versluis, E. Koene, G.-W. Bruggert, D. van der Meer, K. van der Weele, and D. Lohse, *Granular Eruptions: Void Collapse and Jet Formation*, Phys. Fluids **14**, S14 (2002), and D. Lohse, R. Bergman, R. Mikkelsen, C. Zeilstra, D. van der Meer, M. Versluis, K. van der Weele, M. van der Hoef, and H. Kuipers, *Inpact on Soft Sand: Void Collapse and Jet Formation*, Phys. Rev. Lett. **93** 198003 (2004).

bottom plate. In such loose packings, the yield strength is much smaller than in dense packings and we found that the jet formation is strongly enhanced here and reproduces well. In addition, a novel "granular eruption" is observed for deep impacts. To observe the jet formation in more detail, we have also performed experiments in a quasi two dimensional geometry, and finally we describe a simple Rayleigh-type model that numerically reproduces the experimentally observed jet formation qualitatively.

5.2 Experimental observations

As stated in the introduction, we have studied the effect of impact in both a three dimensional and a quasi two-dimensional setup; we will concentrate on the former first. This setup consist of a container with dimensions $15\times15\times50$ cm, which has two transparent side walls such that the impact and the jet can be studied. This container is filled with a 25-40 cm thick layer of non-spherical sand grains with sizes ranging from 10μm to 100μm (average grain size $\approx 40\mu$m. The bottom of the container consists of a porous plate, enabling air to flow through the sand. Air pumped through the sand layer leads to the fluidization of the bed and by turning this flow off slowly the sand layer is left to settle down gently. This procedure results in the generation of a very homogeneous, extremely loose layer of sand. The experiment then consists of dropping a steel ball of radius R_0=1.25 cm into the sand bed from various heights and recording the resulting dynamics with a high speed camera (up to 2000 frames per second).

In this setup we found, for release heights that are not too large, a qualitatively similar phenomenology to the jets observed by Thoroddsen and Shen [6], but when the dropping height, and hence the impact velocity, is above a certain value, interesting new behavior is found. This is illustrated in Figure 5.1, which shows key features of the jet formation for large impact velocity. First the ball impacts, vanishes into the sand, and a crown-like splash is created (Figure 5.1a-d). Inhomogeneities develop in the crown of the splash due to the inelastic particle-particle collisions. A crater is formed and after a while a jet shoots out of the sand at the position of impact (Figure 5.1e-h). While the upper part of the jet is still shooting up, in the lower parts the inelastic particle-particle collisions lead to density inhomogeneities in the jet (similar to what is found for the splash). These inhomogeneities resemble those of the surface tension driven Rayleigh-instablity of a liquid jet, even though there is no surface tension in granular matter. The formation of the splash and jet have also been observed by Thoroddsen and Shen, although

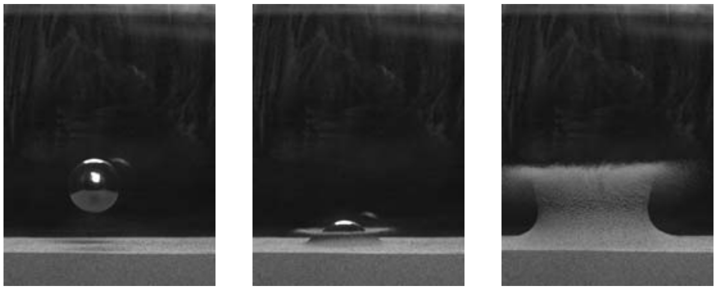

(a) t=-7ms (b) t=5ms (c) t=33ms

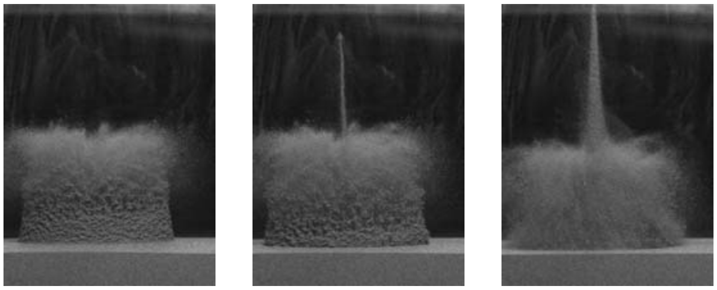

(d) t=88ms (e) t=108ms (f) t=148ms

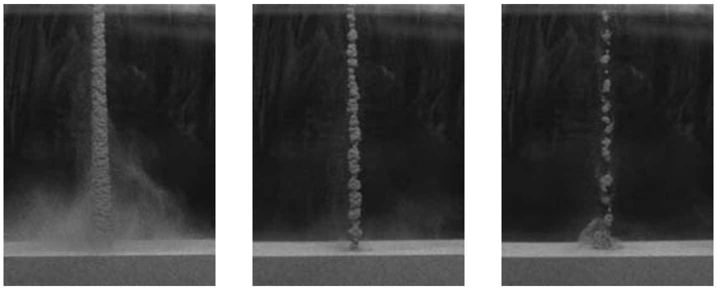

(g) t=233ms (h) t=358ms (i) t=452ms

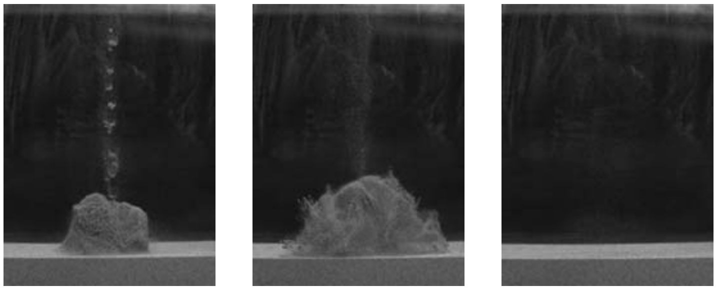

(j) t=503ms (k) t=583ms (l) t=833ms

Figure 5.1: Jet formation after impact (v_0=2.43m/s) of a steel ball of R_0=1.25cm on loose, very fine sand. The jet in this experiment exceeds the release height of the ball. Frames (b)-(d): splash; frames (e)-(f): a jet emerges; frames (g)-(h): clustering within the jet; frames (i)-(k): granular eruption at the surface; frame (l): smooth surface after events.

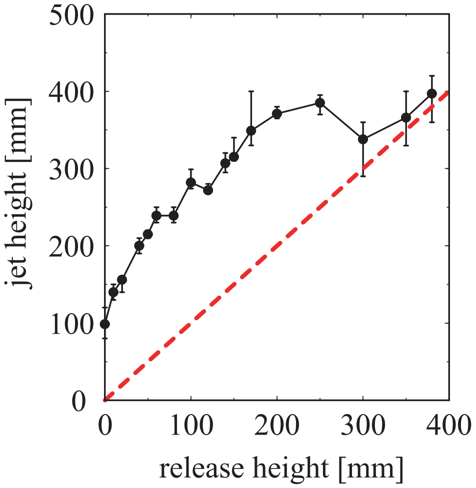

Figure 5.2: Maximum height the jet reaches for different release heights. The maximum always exceeds the release height represented by the dashed line, except possibly for release heights above 300mm. Here the ball penetrates so deep into the sand that it hits the bottom, resulting in the saturation of the maximum height. Notice that dropping the ball right at the sand surface (release height zero) results in a 10cm high jet.

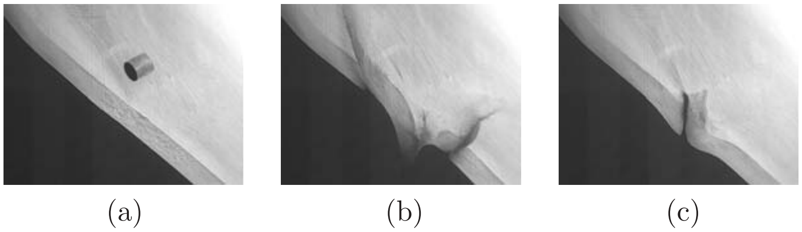
(a) (b) (c)

Figure 5.3: Cylinder impacting on a slit of sand between two transparent plates, resembling a quasi-2D version of the impact experiment. This makes it possible to track the void contours during impact and collapse.

it should be noted that in all our experiments the jet height exceeds the release height of the ball (see Figure 5.2), whereas the jets of Thoroddsen and Shen never reach the release height [6]. This is, presumably, because in their experiments the sand is less fine and more compact.

The novel phenomenon here is the eruption found for high impact velocities, after the jet has reached its maximum height and is on its way down (Figure 5.1i-k). The variation of the strength of this eruption on ball size, release height and on the density of the sand layer indicates that this eruption is related to the void collapse for deep impacts. As we will make plausible below, if this void collapses *above* the ball it entraines air below. This entrained air bubble then slowly rises to the surface and causes the granular eruption when it reaches the surface, resembling a boiling liquid – or even a volcano.

To understand in more detail how the jet and eruption form, and what leads to the qualitative difference between small and large impact velocities, we need to find out what is going on below the surface of the sand. We therefore performed a series of similar experiments in a quasi two-dimensional setup, replacing the ball by a cylinder and dropping it into a container with a quasi-2D cross section of 50cm × 1.5cm, filled with loosely packed sand. The side plates are transparant and we let the cylinder drop with its axis parallel to the surface and orthogonal to these side plates. The same sand is used as in the 3D setup and also here air is blown through the sand in order to generate a homogeneous, loose sand bed. An example of impact in this setup is shown in Figure 5.3, which verifies the two-dimensional nature of the jet formation. The impact formes a splash above the initial height of the layer and a void below (Figure 5.3a). The void collapses as the walls are pushed inwards by the sand pressure (Figure 5.3b), which focusses into a single upward jet (Figure 5.3c) now taking the form of a sheet, but with a much smaller maximum height. This is due to the fact that in 3D the approximately cylindrical void collapses radially inward, while in 2D the void collapse is less focused due to the flatness of the contours.

In Figure 5.4 and Figure 5.5 two side views are shown for low and high impact velocity, respectively. In both cases, the formation of a splash and jet, similar to the 3D case, can be observed. But an important difference between these two cases is how the void collapses. For low impact velocities the void collapses from the bottom and up (Figure 5.4d-g). In contrast, a high impact velocity causes the cylinder to propagate so deep, that the void collapses before the cylinder comes to a stand still, entraining air (Figure 5.5g-h). Notice that in this case two jets are formed: one upwards (the one visible above the surface) and one downwards into the entrained air bubble (Figure 5.5i-j). The bubble slowly rises, leading to a granular eruption at the surface (not shown).

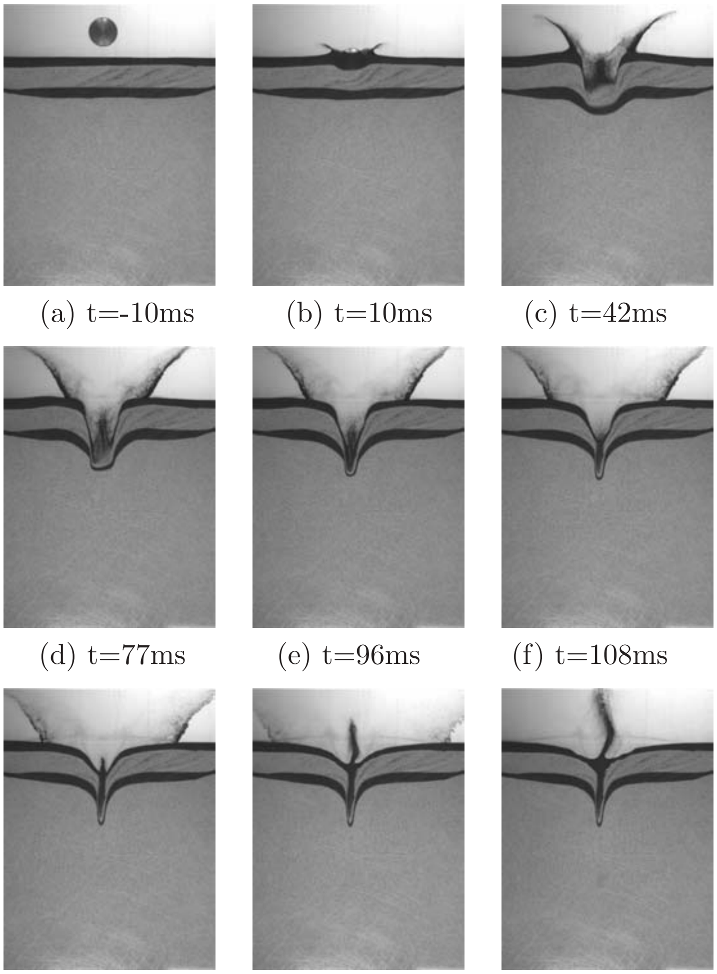

(a) t=-10ms (b) t=10ms (c) t=42ms

(d) t=77ms (e) t=96ms (f) t=108ms

(g) t=123ms (h) t=151ms (i) t=208ms

Figure 5.4: The formation and collapse of a void for low impact velocity ($v = 1.72$ m/s) in the 2D setup. Frames (b)-(d): the impact creates a splash above the surface and a void below; frames (e)-(h): the void collapses from the bottom and up and a jet is formed; frame (i): the jet reaches its maximum height.

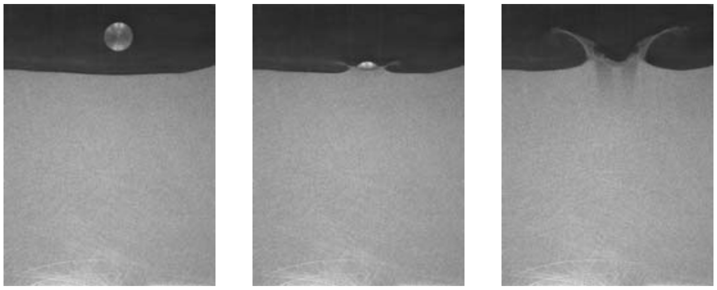

(a) t=-21ms (b) t=10ms (c) t=37ms

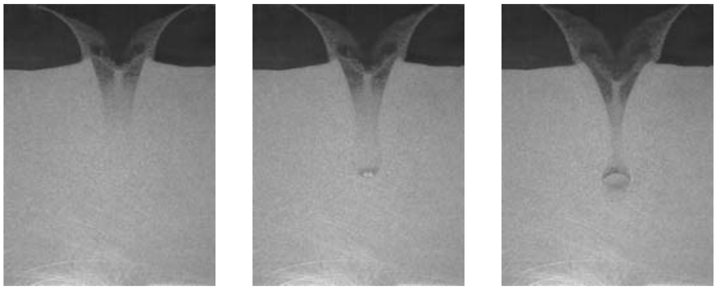

(d) t=66ms (e) t=78ms (f) t=100ms

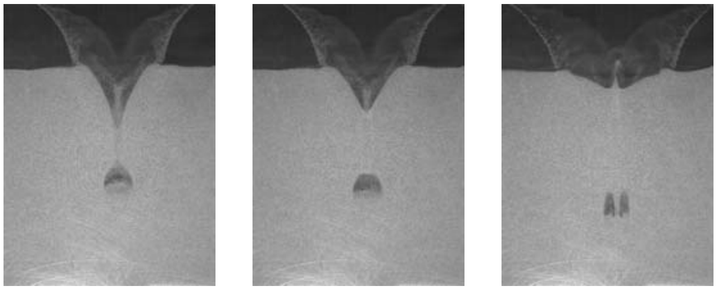

(g) t=108ms (h) t=116ms (i) t=150ms

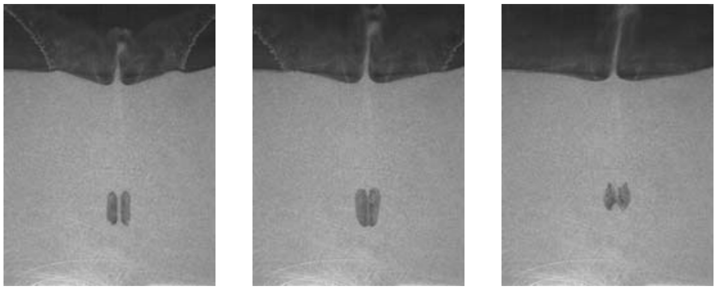

(j) t=166ms (k) t=191ms (l) t=236ms

Figure 5.5: Air entrainment as seen in experiment using the 2D setup for a high impact velocity ($v = 2.43$ m/s). Frames (b)-(e): impact creates splash above surface and void below; frames (f)-(h): the void collapses entraining air; frames (i)-(k): the upward and downward jets are formed: frame (l): the bubble rises.

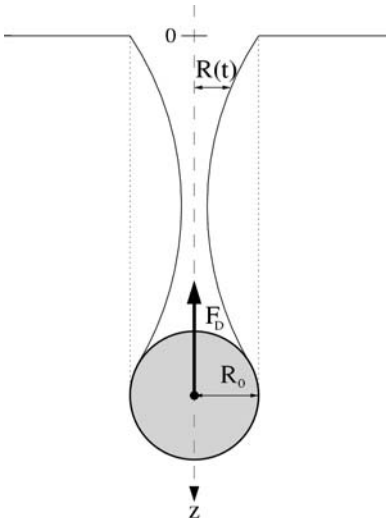

Figure 5.6: Sketch of the void collapse. When the accelerated sand grains from the sidewalls of the cylindrical cavity collide on the axis of the cavity, two jets are formed: One downward into the entrained air bubble formed above the sphere, and one upward straight into the air.

5.3 Rayleigh type model

To work out the essentials of the void collapse, we now construct a “minimal” continuum mechanical model. First, the delay curve $z(t)$ of the ball in the sand can be obtained from a simple force balance model involving drag, gravity, and added mass. It describes the experimental results obtained for a falling ball equipped with a thin tail rod, which allows for easy depth measurements [9]. The delay curve $z(t)$ of the ball is inverted to obtain $t_{pass}(z)$, the time when the ball passes the layer of sand at depth z. This sets the initial conditions for the collapse of the two-dimensional void, namely $R(z, t_{pass}) = R_0$ and $\dot{R}(z, t_{pass}) = 0$. Here $R(z, t)$ is the time and depth dependent radius of the void, see figure 5.3.

Assuming that the sphere penetrates the sand under the influence of a constant deceleration a_f, and hits the surface with an impact velocity v_0, it comes to a stand still after $t = v_0/a_f$. The impact velocity as a function of the dropping height h_r, is found from energy conservation to be

$$v_0 = \sqrt{2gh_r} \quad . \tag{5.1}$$

The maximum depth the sphere reaches is

$$d_{max} = \frac{1}{2} v_0^2 / a_f \quad , \tag{5.2}$$

and the trajectory of the sphere is

$$z(t) = v_0 t - \frac{1}{2} a_f t^2 \quad . \tag{5.3}$$

Inverting this expression yields the time $t_{pass}(z)$ when the sphere passes the layer at depth z,

$$t_{pass}(z) = \frac{v_0 - \sqrt{v_0^2 - 2a_f z}}{a_f} \quad . \tag{5.4}$$

Next, the collapse of the void formed by the ball has to be described. It is driven by the ("hydrostatic") sand pressure $p(z)$ at depth z. For small z the pressure simply is $p(z) = \rho_s g z$, for larger z it saturates [10]. Here, ρ_s is the sand density, assumed to be constant.

We consider the implosion of a cylindrical cavity in a surrounding incompressible and inviscid fluid initially at rest at pressure $p(z)$. The Euler equation in cylindrical coordinates takes the form

$$\frac{\partial v}{\partial t} + \frac{\partial}{\partial r}\left(\frac{1}{2}v^2 + \frac{p}{\rho_s}\right) = 0 \quad . \tag{5.5}$$

Inserting the continuity equation $rv = F(t) \Leftrightarrow v = F(t)/r$ into equation (5.5) gives

$$\frac{\dot{F(t)}}{r} + \frac{\partial}{\partial r}\left(\frac{1}{2}v^2 + \frac{p}{\rho_s}\right) = 0 \quad . \tag{5.6}$$

By assuming that R_∞ is a far away point, such that $v(R_\infty, t) = 0$ and $p(R_\infty, t) = p(z)$ at all times, we are able to integrate equation (5.6) from R_∞ to $R(t)$,

$$\int_{R_\infty}^{R} \frac{\dot{F(t)}}{r} dr + \int_{R_\infty}^{R} \frac{\partial}{\partial r}\left(\frac{1}{2}v^2 + \frac{p}{\rho_s}\right) dr = 0 \quad , \tag{5.7}$$

which gives the equation

$$\dot{F}(t) ln \frac{R}{R_\infty} + \frac{1}{2}V^2 - \frac{p(z)}{\rho_s} = 0 \quad . \tag{5.8}$$

Here we have used that $p(R, t) = 0$, $v(R_\infty, t) = 0$ and $p(R_\infty, t) = p(z)$.

The continuity equation should also be valid on the cavity border, such that $F(t) = R(t)V(t)$. Writing $V(t) = \dot{R}(t)$, we find a Rayleigh-type ordinary differential equation for an imploding cylindrical cavity in an inviscid, incompressible fluid at pressure $p(z) = \rho_s g z$,

$$(R\ddot{R} + \dot{R}^2) ln \frac{R}{R_\infty} + \frac{1}{2}\dot{R}^2 = \frac{p(z)}{\rho_s} = gz \quad . \tag{5.9}$$

The Rayleigh type model is applied to the collapsing void problem by solving equation (5.9). The sand is discretized into N individual layers which become active as soon as the sphere has passed and the equation for the collapsing void (5.9) is solved for each active layer. Since the sand pressure is assumed to increase linearly with depth, the acceleration with which the cavity begins to collapse also increases with depth. This increase in pressure and the fact that the cavity begins to collapse as soon as the sphere has passed, makes air entrainment possible. Solving the ordinary differential equation (5.9) is numerically relatively straightforward and the dynamics following from these simulations is shown in Figure 5.7, resembling the void collapse in the 2D experiments for high impact velocity shown in Figure 5.5. Just as in the experiment shown in Figure 5.4, the void described by this model collapses from the bottom and up for low impact velocities (not shown).

5.4 Conclusion

When a solid sphere impacts on a loosely packed bed of sand, a splash is formed above the surface and a jet is seen to rise straight up into the air. The jet is created as the crater formed by the impact collapses due to the sand pressure. For a sufficiently high impact velocity we find that air is entrained beneath the surface. This entrained air bubble then slowly rises to the surface where it causes a granular eruption. We have described the void collapse by a simple Rayleigh-type model, and found good agreement with experimental findings.

References

[1] A. M. Worthington, *A study of splashes* (Longman and Green, London, 1908).

[2] H. Oguz and A. Prosperetti, J. Fluid Mech **219**, 143 (1990).

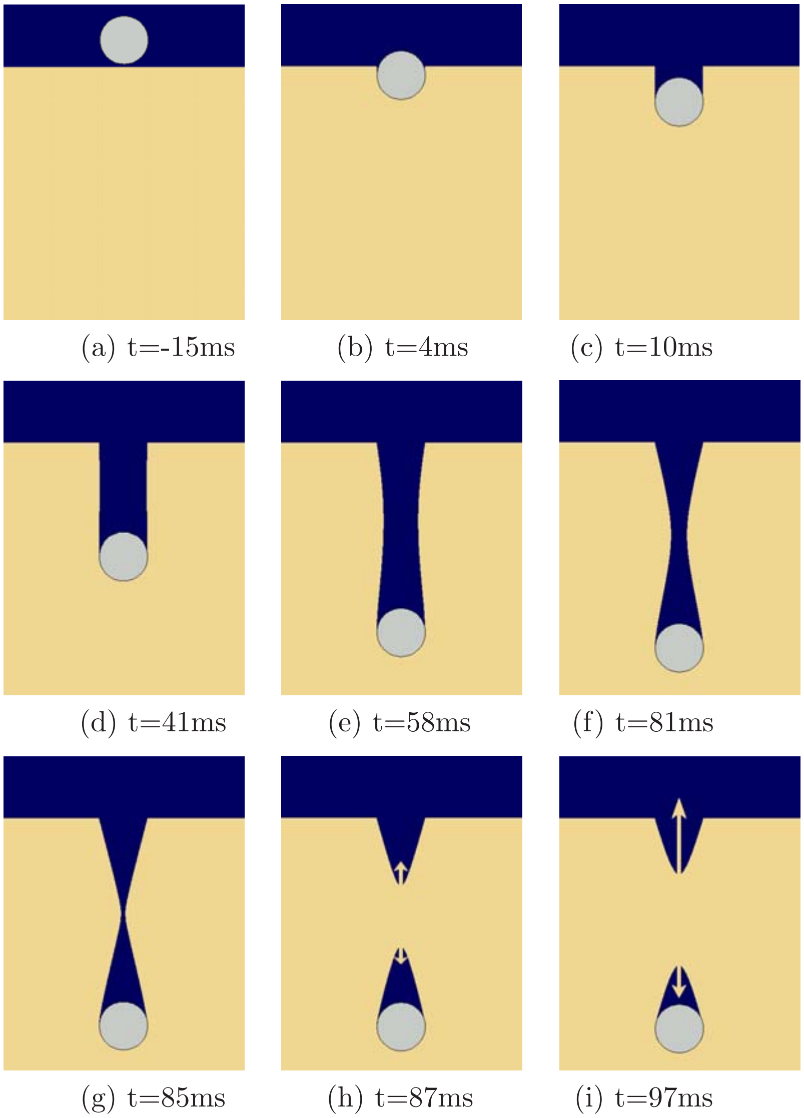
(a) t=-15ms (b) t=4ms (c) t=10ms

(d) t=41ms (e) t=58ms (f) t=81ms

(g) t=85ms (h) t=87ms (i) t=97ms

Figure 5.7: Cross-section of the 3D-void collapse following from the Rayleigh-type model, for the same impact velocity and ball radius as in figure 5.1. The void is pressed together by the "hydrostatic" pressure from the side, leading to a singularity and an upward and downward jet.

[3] A. Prosperetti and H. Oguz, Ann. Rev. Fluid Mech. **25**, 577 (1993).

[4] J. E. Hogrefe, N. L. Peffley, C. L. Goodridge, W. T. Shi, H. G. E. Hentschel, and D. P. Lathrop, Physica D **123**, 183 (1998).

[5] D. Lohse, Phys. Today **56**, 36 (2003).

[6] S. T. Thoroddsen and A. Q. Shen, Phys.Fluids **13**, 4 (2001).

[7] R. Mikkelsen, M. Versluis, E. Koene, G.-W. Bruggert, D. van der Meer, K. van der Weele, and D. Lohse, Phys.Fluids **14**, S14 (2002).

[8] D. Lohse, R. Bergman, R. Mikkelsen, C. Zeilstra, D. van der Meer, M. Versluis, K. van der Weele, M. van der Hoef, and H. Kuipers, Phys.Rev.Lett. **93**, 198003 (2004).

[9] D. Lohse, R. Rauhé, R. Bergmann, and D. van der Meer, *Dry Quicksand* Nature, in press (2004).

[10] J. Duran, *Sands, powders, and grains*, 1st ed. (Springer, New York, 1999).

Chapter 6

Granular flows in Couette cells: wall localized shearbands

Abstract

An experimental study of granular shear flows in Couette-like rheometers is presented. For sufficiently deep layers of grains, the system exhibits a narrow shear band which is localized at the inner wall and is independent of the bottom topography. For a wide variety of particle shapes and polydispersities we have found that the velocity profiles of these shear bands tend to decay exponentially away from the inner cylinder. This decay rate does not only depend on the size of the particles, but also on the radius of curvature.

6.1 Introduction

When external stresses are applied to a granular material, the resulting flow is different from that of an ordinary fluid. Instead of deforming uniformly, narrow *shear bands* are formed where the material flows and yields, while the rest of the material remains solid-like and barely deforms. Shear bands dominate the flow, represent areas of material failure and energy dissipation, and are important for the understanding of many industrial and geophysical processes. The narrow width of typical shear bands (5-10 grain diameters) forms a major obstacle for continuum theories for granular flows.

For slow granular flows this behavior is typically described by Mohr-Coulomb models, which are based on an analogy with the classical description of friction between two solid bodies. For ordinary friction, an object on a frictional surface remains at rest until the tangential force exceeds the product of the static friction coefficient and the normal force. When the object is made to slide, the ratio between tangential and normal force is given by the dynamic friction coefficient. This dynamic friction coefficient is usually smaller than the static one, leading to hysteresis, and is only a weak function of the shearing velocity.

In the granular context one considers the materials as continuous (i.e. ignores the small grain-scale structure) and assumes that the frictional laws should hold for any imaginary plane in the material. Instead of normal and tangential forces one then considers the normal and tangential stresses along these planes. When applying an overall shear stress to the granulate, one thus searches for planes where the ratio of shear and normal stress is maximal; when they exceed the static friction coefficient, yielding along these planes takes place. Since the necessary shear stress to sustain shear flow along such a slip plane is below the static threshold, this model immediately leads to (infinitely) narrow shear bands. In addition, the constant dynamic friction coefficient leads to rate independence, i.e., neither the morphology of the shear bands nor the overall applied stress does depend on the shear rate. But this theory does not predict any of the details of the shear bands (their width, precise functional form of the velocity field etc).

To study the behavior of sheared granular matter experimentally, Couette cells are often used. A Couette cell is a rheometer formed by two coaxial cylinders rotating with respect to each other. In rheology such devices are used to determine (effective) viscosities, yield strengths and aging for a wide range of complex fluids such as foams, mayonnaise and gels. Their circular geometry allows for continuous, long time studies of the material, which is the main advantage, but also leads to a radially inhomogeneous stress field and curvature effects. These two features will be important for granulates.

By filling such a setup with a granular material, a stable flow field can quickly be established where a shear band is formed around the rotating inner cylinder. The shear stresses are largest near the inner cylinder, and following the Mohr-Coulomb picture sketched above, this is where one would indeed expect a narrow shear band. For a wide range of different grains experiments have verified that the velocity profiles are rate independent [1, 2], in agreement with the Mohr-Coulomb models. It therefore is convenient to define a non-dimensional flow rate, $\omega(r)$, which is the ratio between the average azimuthal velocity at r and the rotation rate of the inner cylinder Ω. The velocity profile $\omega(r)$ is a rapidly decaying function when r moves away from the inner cylinder. It is generally agreed that the “width” of the shearband is very narrow and set by the grain scale; the function form of ω is *not* agreed upon [1–5]. Over the past few years, it has become clear that $\omega(r)$ does not really become zero anywhere in the material; even though a superficial inspection suggest the existence of a large, completely stationary part of the system, in fact these areas also exhibit flow, albeit very slowly [2–5].

Mueth *et al.* [2] determined the Couette flow for two different granular media, one consisting of (nearly) mono-disperse, smooth, spherical particles, and one for kidney-shaped particles. In their experiments the velocity profiles were found to be roughly exponential for the mono-disperse, spherical particles and Gaussian for the non-spherical ones. These results support the argument that the overall shape of the velocity profile arises from two main contributions: an exponential "slip" contribution in the presence of layering and a diffusive-like contribution associated with disorder. In general, a combination of these effects can be expected, and so one may attempt to fit the data with a combination of an exponential and Gaussian:

$$\omega(r) = \omega_0 \exp\left(-b\frac{r}{d_p} - c\left(\frac{r}{d_p} - \frac{r_0}{d_p}\right)^2\right) \quad . \tag{6.1}$$

Here d_p denotes the grain size, which is a natural length scale in this problem. Indeed, with this scaling, b was found by Mueth *et al.* to be of order one [2]. The Gaussian term has two fit parameters, c and r_0; the last one is hard to get from real data when the Gaussian term is small. The distinction between the velocity profiles of the spherical and non-spherical particles is essentially given by the ratio of b and c. Mueth *et al.* found for spherical particles $\{b,\ c,\ r_0/d_p\} = \{0.36 \pm 0.13,\ 0.06 \pm 0.03,\ 0.6 \pm 0.8\}$, while for the kidney shaped particles $\{b,\ c,\ r_0/d_p\} = \{0,\ 0.11 \pm 0.02,\ -0.1 \pm 0.5\}$. Other experiments have found similar exponential profiles for nearly mono-disperse, spherical granular media, except for the first couple of grains right next to the inner cylinder where the velocity is found to decrease slower [1].

To gain information about the full 3D flow field is a complex task. Different approaches have been taken, such as submerging the grains in an index matched fluorescent fluid and using a lasersheet to scan through the material [6], as well as X-ray and magnetic resonance imaging (MRI) [2]. The results showed that the velocity profile near the fixed surface at the bottom, at the free surface at the top, and in the interior are the same to within the resolution of these measurements. Thus one only needs to determine the flow at the top surface in order to characterize the flow, a much simpler task than determining the full flow field. This is only true for the simple

Couette flows and not for the more complex split-bottomed Couette flows we will encounter below.

Experiments using Couette cells have revealed many characteristic granular phenomena. For example, in a binary mixture of spherical glass particles size segregation takes place, where the larger particles rise to the top of the mixture and stay there as rotation continues [7]. At the same time the smaller particles, which in these experiments outnumber the larger ones, were found to undergo a convection-like motion where they sink downwards while in contact with or very close to the inner cylinder, but rise upwards when not in its vicinity. This flow pattern resembles that of convection in fluids. It also connects nicely to the Brazil nut effect in a vibro-fluidized granular medium, where large particles surrounded by smaller ones rise to the top of the mixture. The convective motion of the small particles, which rise in the bulk of the medium and sink near the walls of the container, has been argued to be responsible for this phenomenon.

6.1.1 Universal shear zones

To study shear bands without the influence of the lateral boundaries, a simple modification of the Couette cell has been introduced [4, 5]. Splitting the bottom support at $r = R_s$ in two, such that the inner part rotates with the inner cylinder while the outer part remains stationary together with the outer wall (see Figure 6.1), creates a shear zone which propagates up from the discontinuity at R_s, towards the free surface of the material. The resulting flow rapidly reaches a steady state in which it can be kept indefinitely, allowing for accurate observations of the flow field. The radial component of the average surface flow is found to be negligible and the average flow is thus in good approximation azimuthal.

The main observation is that for intermediate filling levels H, where the shear band is not in contact with any of the boundaries, the velocity profiles $\omega(r)$ follow an error-function type master curve:

$$\omega(r) = \frac{1}{2} + \frac{1}{2}\text{erf}\left(\frac{r - R_c}{W}\right) \quad . \tag{6.2}$$

This has been verified for a wide range of granular materials and experimental parameters R_s (slip radius) and H (filling height) [5]. The regime where $\omega(r)$ follows equation (6.2) is denoted the universal regime: by renormalizing the position according to $\lambda = (r - R_c)/W$, all measured velocity profiles collapse onto a single curve. Experiments have shown that these profiles are rate independent, just as in the Couette geometry, and in agreement with Mohr-Coulomb models.

In the universal regime all the information on the velocity profiles at the surface can be condensed in the variation of the center position of the shear zone R_c and its width W with the filling height H and location of the split R_s. R_c was found to be independent of the type and size of grains used, so the only relevant length scales determining R_c appear to be H and R_s. As the filling height H is increased, the position of the shear zone at the free surface $R_c(H)$ moves towards the center of the shear cell. The dimensionless displacement of the shear zone, $(R_s - R_c)/R_s$, is a function of the dimensionless height H/R_s only. The following relation,

$$\frac{R_s - R_c}{R_s} = \left(\frac{H}{R_s}\right)^{5/2} \quad , \tag{6.3}$$

has been found to give excellent agreement with experimental findings for different granular media [5]. The width W was found to be independent of R_s, and grows with H and particle diameter [5].

The results from the ordinary and split-bottomed Couette cells clearly illustrate the paramount importance of the lateral boundaries. Summarizing the main results, in a Couette cell the shear band is located at the inner cylinder, the velocity profile is independent of height, and its functional form may depend on particle shape. For the split-bottomed geometry both the width and the localization of the shear band vary with the filling height H. Increasing H makes the shear band wider while its center position moves closer to the inner cylinder and at a certain filling height, H_c, the shear band reaches the inner cylinder.

In the experiments we will study in detail the wall-localized shear bands. We will first show how the velocity profiles in the split-bottomed geometry evolve towards a narrow wall-localized shear band for filling heights $H > H_c$. We will show that, for large heights, velocity profiles in both Couette and split-bottomed cells become height-independent and equal. We will also find that, away from the inner cylinder, these profiles exhibit an almost purely exponential decay independent of particle properties; this is in apparent contrast to the findings in [2]. Finally we will study the spatial decay rate of these profiles, and find to our great surprise that this decay rate does not simply scale with particle size only, but that the value of radius of curvature plays a crucial role.

6.2 Experimental setup

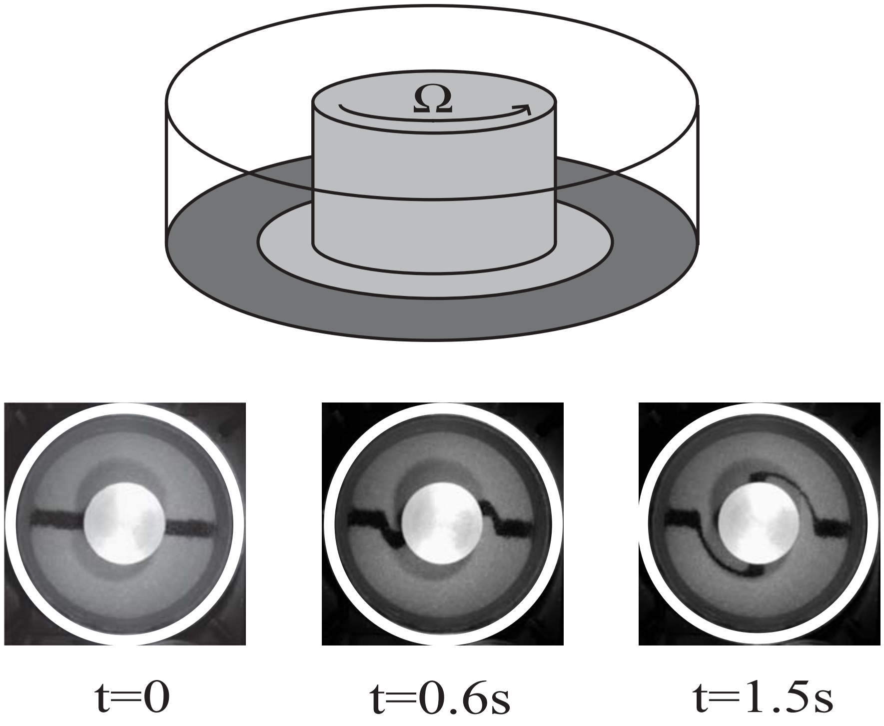

Figure 6.1: Drawing of the experimental setup illustrating the split-bottomed geometry: the dark area of the bottom remains stationary while the bright area of the bottom rotates together with the inner cylinder. The three pictures in the lower row shows the surface flow for 1 mm glass particles filled at $H = 10$ mm. A black line of tracer particles is added to the surface layer, illustrating the bulk localization of the shear zone.

Our experimental setup is constructed of an outer and inner cylinder with radii R_{out} and R_{in} respectively, and a stationary bottom plate. In all our experiments the radius of the outer cylinder is $R_{out} = 110$ mm, while we have a choice of three different inner cylinders with radii $R_{in} = 2.5$ mm, 20 mm, and 40 mm. A disk of radius R_s can be attached under the inner cylinder, which then covers the annular area $\pi(R_s^2 - R_{in}^2)$ of the bottom surface. By fixing the disk to the inner cylinder such that the two rotate together, we obtain the split-bottomed geometry as sketched in Figure 6.1(top). If no disk is attached under the inner cylinder, one obtains the standard Couette

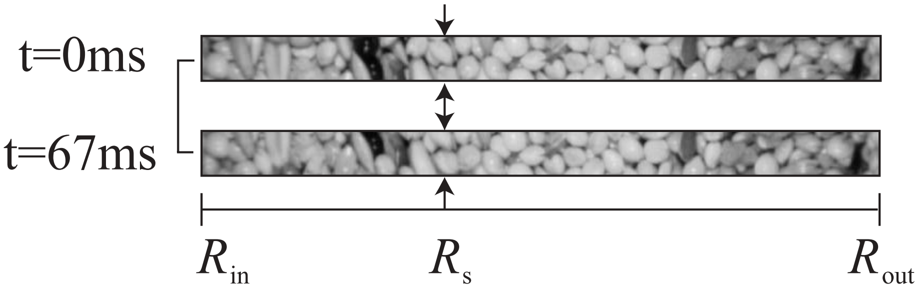

Figure 6.2: Two pictures from experiments using bird seeds filled to a height $H = 10$ mm. The lower picture is taken $t = 67$ ms after the first one. The split is located at $R_s = 65$ mm, marked in the pictures by arrows. Note that all material between R_{in} and R_s is shifted upwards, whereas the seeds the the right of R_s remain (approximately) stationary.

geometry. To obtain rough boundaries, two methods have been employed. The simplest method is to glue grains, similar to those used in the bulk, to the outer wall, inner cylinder and bottom rings. However, for wall-localized shear bands we find that the glue is not strong enough, and gradually the glued particles come off the inner cylinder. In addition, the fact that we want to study many different types of particles makes this procedure very cumbersome. Therefore we have made new inner cylinders where 5 mm deep grooves were cut along the vertical direction of the cylinder. Grains then fill up the space between the grooves and the net result is a boundary that is rough on the order of the grains scale.

The inner cylinder is driven by a DC motor and its rotation speed is controlled by duty cycle modulation under control of a feedback loop. As a result, its rotation speed remains essentially constant even though the exerted torque, due to fluctuations in the material, is varying. Some vibrations are transferred to the granulates as a result, but these appear small compared to the vibrations induced by the shearing of the material itself. For the rotation rates possible with this setup the flow has been verified to be rate independent and centrifugal forces are negligible. For simplicity, the same rotation rate $\Omega = 0.17$ rad/s is employed in all measurements.

The lower row in Figure 6.1 illustrates the surface flow in this setup for a $H = 10$ mm layer of 1 mm glass beads. Here two stripes of 1 mm black particles have been added to the surface layer for illustrative purposes.

The surface motion of the grains are captured with an 8-bit Sony VLFD-500 digital camera with frame rates up to 30 frames per second. The camera is controlled by Labview which is also used for the data analysis. Halogen spots are used to illuminate the surface layer. Each picture captures the cross section of the surface layer from the inner to the outer cylinder. Figure 6.2 shows two typical pictures from an experiment with bird seeds using the inner cylinder with radius $R_{in} = 40$ mm. The split is located at $R_s = 65$ mm. The dimensions of these snapshots are 40x640 pixels, which corresponds to a spatial resolution of 0.11 mm/pixel.

The velocity profile is obtained by a variation on particle image velocimetry (PIV). From the movies of the surface of the granulate, the angular correlation function as function of r is determined for pairs of frames separated by Δt. Averaging over many pairs (typically 2000) and determining the peak of the correlation function results then in the average azimuthal grain motion over Δt, from which the angular velocity can be determined. This dimensional quantity is then non-dimensionalized by dividing by Ω, so that we end up with $\omega(r)$ ranging from zero (no motion) to one (co-moving with rotating cylinder.

To obtain high precision values for the velocity profiles, pictures are taken with three different time intervals for every measurement, $\Delta t = 33.33$ ms, $\Delta t = 1033$ ms, and $\Delta t = 10031$ ms, collecting a total of 2000 snapshots for each Δt. In some cases, e.g. for very large particles, up to 7000 snapshots of dimension 60x640 pixels are taken. The longer time intervals give a better resolution of the particle motion in the slow-moving tail, since the grains have traveled further between two successive images. The three profiles are merged into one by simple rescaling according to the difference in Δt between two measurements. In this manner, ω can be obtained over roughly six decades.

We will perform experiments with grains of different shapes and polydispersities. Table 6.1 shows the names of the different materials available, together with our estimates of their actual average grain size $\langle d_p \rangle$. The bird seeds are rather peculiar, as they consist of a mixture of round ($r \sim 2$ mm) and elongated (dimension $\sim 2 \times 5$ mm) grains (see also Figure 6.2).

6.3 Split-bottomed geometry

In Figure 6.3 we present an example of typical velocity profiles obtained for the split-bottomed geometry with $R_s = 65$ mm and $R_i = 40$ mm, for various filling heights of glass beads of size 0.875 mm. For intermediate filling levels ($H \lesssim 30$ mm) the shear band is not in contact with any of the walls and the profiles resemble the universal profiles found in the original

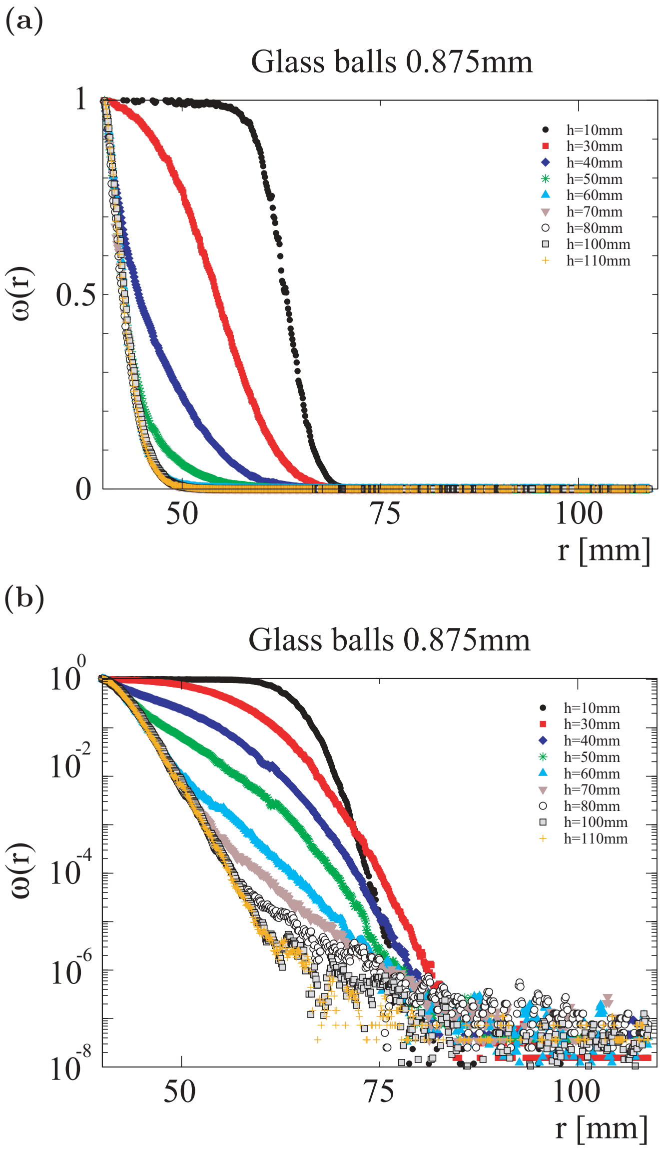

Figure 6.3: Angular velocity profiles measured in the split bottomed geometry at various filling heights H. The velocity at the inner cylinder is normalized to unity. At intermediate filling heights $H < 35$ mm the shear band is located in the bulk, which is denoted the universal regime. Its center position moves towards the inner cylinder and its width grows as H is increased. For filling heights $H > 35$ mm the shear bands reaches the inner cylinder and a smooth transition towards the wall collapsed regime takes place as H is increased.

material	$\langle d_p \rangle$
0.875 mm glass beads	0.9 mm
1 mm glass beads	1.2 mm
2 mm glass beads	2.4 mm
3 mm glass beads	3.2 mm
4 mm glass beads	4.0 mm
5 mm glass beads	5.0 mm
6 mm glass beads	6.0 mm
1.3 mm plastic flakes	1.3 mm
2.3 mm grind sand	2.3 mm
bird seeds	2.0 mm × 5.0 mm

Table 6.1: Estimated values of the average grain size $\langle d_p \rangle$ for the different materials used here.

experiments [4, 5]. By increasing H the shear band location moves closer to the inner cylinder. At some point ($H \approx 35$ mm) the shear band comes into contact with it and a further increase of H results in a transition towards a profile similar to what is measured in a standard Couette cell. This we denote the wall collapsed regime: the shear band is located next to the rotating inner cylinder and the velocity profile immediately decreases with r.

Let us first discuss the results in the universal bulk regime, where the shear band is not in contact with the inner cylinder. Measurements have been performed with spherical, smooth glass beads ranging from $\langle d_p \rangle = 0.9$ mm to 2.4 mm, irregularly shaped plastic flakes with sizes $d_p = 1.3 \pm 0.3$ mm, and bird seeds consisting of a mixture of round (diameter ~ 2 mm) and elongated grains (width ~ 2 mm, length ~ 5 mm). For all materials we find velocity profiles that shows excellent agreement with the error-function given by equation (6.2). The universality of the profiles in this regime is illustrated in Figure 6.5, where the position is renormalized according to $\lambda = (r - R_c)/W$. Here all profiles collapse onto the same curve and no difference is found between approximately monodisperse and irregularly shaped particles as reported in [2] for shear bands in Couette cells. Instead we find that shear bands away from lateral boundaries are universal and independent of the grains, consistent with [4, 5].

To quantify the error between the measured shift of the shear zone center position R_c away from the split radius R_s we introduce the non-dimensional

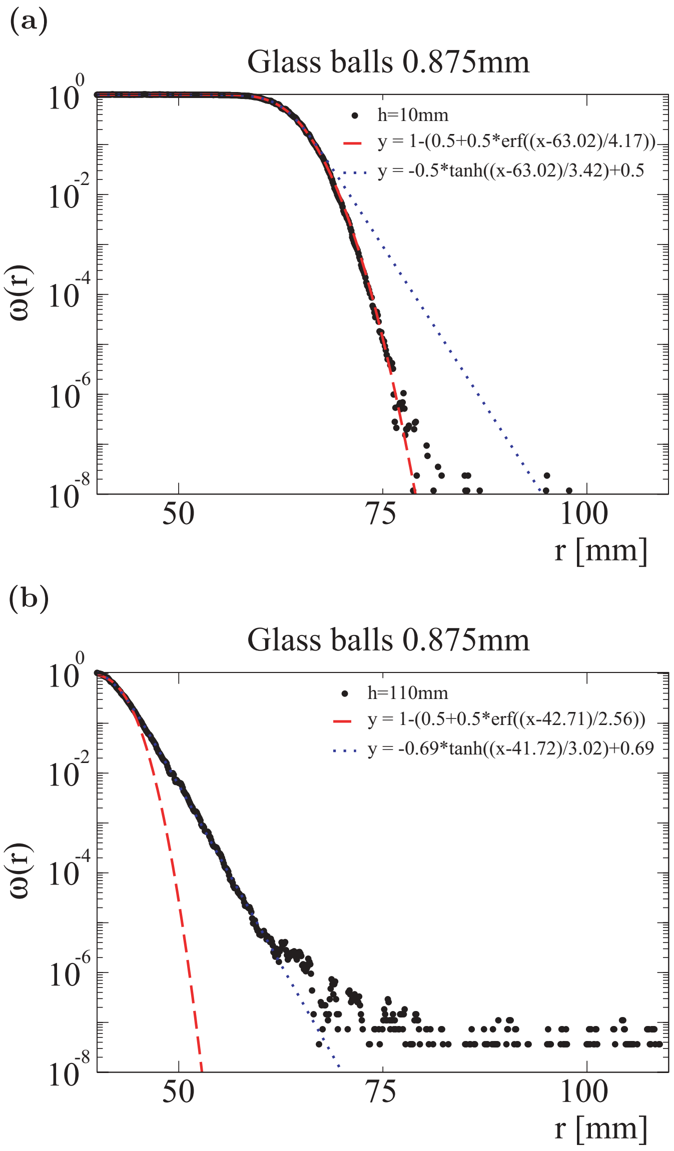

Figure 6.4: Fitting the velocity profiles measured in the split bottomed setup using glass particles of average size 0.875 mm filled to a height $H = 10$ mm (a) and $H = 110$ mm (b) to a tangent hyperbolic (dotted line) and error-function (dashed line) shaped curves. In the universal regime (a) the measured profiles fits well to the error-function, while the tangent hyperbolic only captures the profile well for the first decade. Entering the wall collapsed regime (b) the opposite scenario is found: now the measured profiles agree very well with the tangent hyperbolic, while the error-function decays too quickly after about a decade.

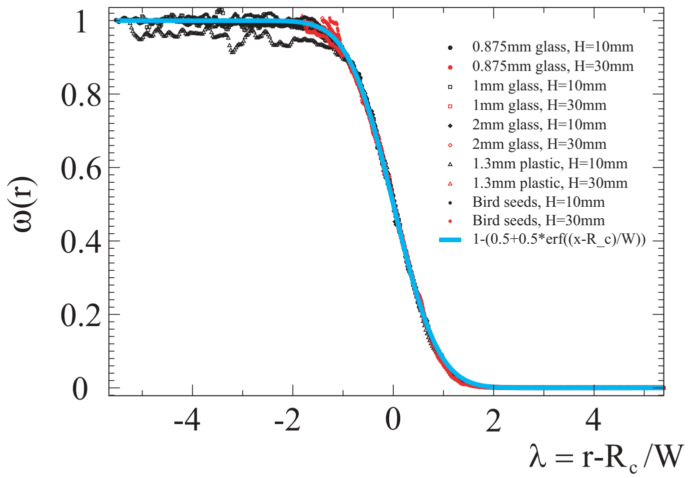

Figure 6.5: Universal bulk velocity profiles obtained for different particles and filling heights, plotted as a function of the rescaled coordinate $\lambda = (r - R_c)/W$. The solid line represents an error-function.

parameter κ:

$$\kappa = \frac{R_c - R_c^*}{|R_s - R_c^*|} \quad . \tag{6.4}$$

Here R_c^* denotes the theoretical location of the shear zone center given by equation (6.3). Table 6.3 shows these quantities together with the width of the shear zone as measured in the universal regime for the different materials. The error κ is quite large for $H = 10$ mm where the difference between the location of the split $R_s = 65$ mm and the predicted location of the center of the shear zone is very small (0.60 mm), but becomes small for larger H, as expected.

We now turn our attention to the shear bands localized near the inner cylinder. Here the measured velocity profiles decay approximately exponentially for large r, which comes out as a straight line in the log-scale plots. The velocity profiles are not purely exponential, in particular, for small r. We found that in good approximation the wall-localized velocity profiles

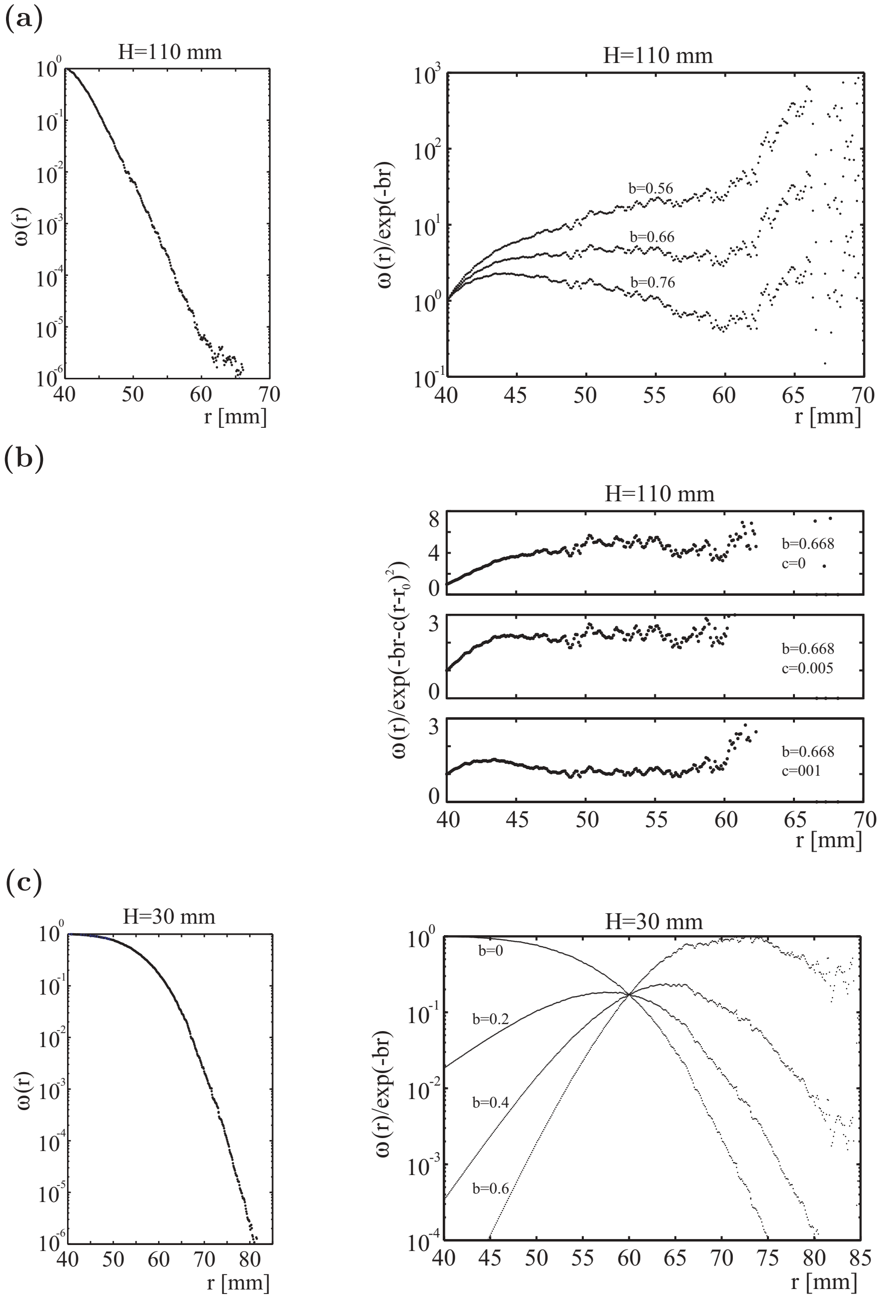

Figure 6.6: The tails of velocity profiles measured in the split bottomed setup for the shear zone located at the inner wall (a)-(b), and in the bulk (c). The left column shows the raw data for (a) H=110 mm, and (c) H=30 mm. In the right column these data sets are divided by equation (6.6); in (a) and (c) we divide by pure exponential $\sim \exp(-br)$, while in (b) we keep b fixed at 0.668, and include a Gaussian correction c.

material	H [mm]	R_c^* [mm]	R_c [mm]	κ	W [mm]
0.875 mm glass	10	64.40	63.02	2.3	4.17
0.875 mm glass	30	55.59	54.30	0.14	8.49
1 mm glass	10	64.40	63.56	1.40	4.51
1 mm glass	30	55.59	56.19	-0.06	8.63
2 mm glass	10	64.40	63.52	1.47	5.60
2 mm glass	30	55.59	57.13	-0.16	10.71
1.3 mm plastic	10	64.40	63.29	1.85	4.15
1.3 mm plastic	30	55.59	54.15	0.15	7.24
bird seeds	10	64.40	63.91	0.82	4.13
bird seeds	30	55.59	54.89	0.07	10.18

Table 6.2: Values for the theoretical prediction of the location of the center position of the shear zone R_c^*, according to equation (6.3), the measured center position R_c, the error κ, defined by equation (6.4), and the width of the shear zone W, for different materials in the universal regime.

approach a tangent hyperbolic shaped curve:

$$\omega(r) = -C \tanh\left(\frac{r - R_c}{W}\right) + C \quad . \tag{6.5}$$

In Figure 6.4 we compare the fits of this equation and the Gaussian form (equation (6.1)) to the data for $H = 30$ mm and $H = 110$ mm. One clearly sees the difference between the Gaussian and exponential tails for low and high filling level. In the intermediate regime, as shown in Figure 6.4b, the fit of the measured $\omega(r)$ to the hyperbolic tangent initially only captures the part close to the inner wall, but gradually extends further and further into the bulk for higher H.

Of course, we would like to make this more precise, since one can already see some Gaussian-like curvature in the “exponential” tails. Ultimately, we wish to fit our data to an equation of the form of (6.1). Since the polydispersity for some of our mixtures is quite large, we will use a simpler variant of this fit formula:

$$\omega(r) = \omega_0 \exp\left(-br - c\,(r - r_0)^2\right) \ , \tag{6.6}$$

so that b and c remain dimensional and we do not have to “guess” the value of d_p.

Figure 6.6 shows compelling evidence that the nature of the tails changes qualitatively with height; by dividing out the leading exponential decay, and plotting the result, one can get a good idea of the strength of possible Gaussian corrections. In Figure 6.6a we show $\omega(r)/\exp(br)$ for a range of values of b. Clearly, for appropriately chosen b, the data is fitted well, even though some rather small curvature can be detected. From the raw data (see inset of Figure 6.6a) there appears to be a change in slope for $\omega < 10^{-6}$, i.e., for r larger than 60 mm. We attribute this to the finite resolution of our velocity detection. The slowest velocity we can detect varies from dataset to dataset but is roughly of the order 10^{-5} to 10^{-6}. This change in apparent slope is also clearly visible in Figure 6.6a. Also, for small r, there is a substantial deviation from the exponential behavior.

In Figure 6.6a the exponential nature of the tails only holds away from the inner cylinder and can only be detected in a limited range. This makes the fitting to equation (6.6) rather difficult. Nevertheless, as we show in Figure 6.6b, a small Gaussian correction can basically straighten out the curve. The best fit of the fluctuating part of the middle of the profile to a horizontal line is obtained for $b = 0.668$, $c = 0.005$ and $r_0 = 52.5$; for r between 45 and 60 mm, where $\omega(r)$ ranges from 10^{-1} to 10^{-6}, the ratio $\omega(r)/\exp\left(-br - c\,(r - r_0)^2\right)$ varies less than 30%. Note that r_0 is chosen in the middle of the fit regime; it should not be taken as a free parameter. Even at the edge of the regime where this fit is good, i.e., for $r = 45$ or 60, the quadratic term in the exponent $c\,(r - r_0)^2$ is equal to 0.78, while the linear term is 8.35. In addition, c is roughly 100 times smaller than b, so the Gaussian contribution is three orders of magnitude smaller than the exponential.

In Figure 6.6c we finally show the ratio between $\omega(r)$ for H=30 mm and a range of exponentials. Clearly, this tail is not close to an exponent, as we already expected from the errorfunction fits discussed previously.

6.3.1 Convective motion

The surface of the granular material stays fairly flat in the universal regime. However, for filling levels where the shear zone meets the wall, a surface crater rapidly develops around the inner cylinder, with a slope close to the angle of repose. This crater reaches its maximum size for deep layers, i.e., in the wall collapsed regime. The sloped surface leads to a radial, inward component of the average velocity at the surface, and particles are seen to slide down the slope towards the inner wall.

Since after a while the slope does not grow, a convection roll must be present, where particles sink down near the wall and rise further away from the inner cylinder. Indeed, a small heap appears at the outward border of the crater which is probably associated with the region where particles rise to the surface.

The dependency of the surface shape on the location of the shear zone is in good agreement with previous results [5]. A buried layer of tracer particles shows no indication of convective behavior in the universal regime using the split-bottomed geometry. In the Couette geometry, however, previous experiments have shown that tracer particles do undergo convective motion, where they progress downwards near the rotating wall until the bottom of the setup is reached. From there they move away from the rotating wall into the bulk of the material, where they at some point slowly rise to the surface [7]. Convection thus only seems important in the wall-collapsed regime and vanishes in the universal regime. In the worst case, the radial component of the surface velocity can be up to 30% of the total and we do not know if and how this affects the azimuthal velocity profiles. In the remainder of this chapter we will focus exclusively on the azimuthal velocity ω.

6.4 Wall collapsed shear zones

In this Section we will focus on the wall-collapsed shear bands. We will first show that in the Couette geometry, $\omega(r)$ rapidly converges to an asymptotic, height independent velocity profile. In addition we will find that the velocity profile for large heights in the split-bottomed case (see Figure 6.3) is indistinguishable from the asymptotic profile in the Couette geometry. Finally, we will illustrate our finding that for a wide variety of particles shapes and polydispersities, the asymptotic velocity profiles $\omega(r)$ tend to an exponential decay away from the inner cylinder.

In contrast to the split-bottomed geometry, where the shear zone progressively shifts towards the inner wall when H is increased, the shear zone in the Couette geometry meets the inner wall for any filling level H. In Figure 6.7 we illustrate that for the Couette geometry the velocity profiles only weakly depend on height, and that for large filling heights, the velocity profiles rapidly converge towards a single curve. By comparing $\omega(r)$ for split-bottomed and Couette geometry, we find, for large heights, the profiles in the split-bottomed setup approach the asymptotic Couette profile. This is illustrated in Figure 6.8a: here the solid circles represent measurements from the split-bottomed setup for different H, and the open circles correspond to the asymptotic Couette cell profile, which is also shown separately in Figure 6.8b. The crossover between universal and wall-collapsed profiles

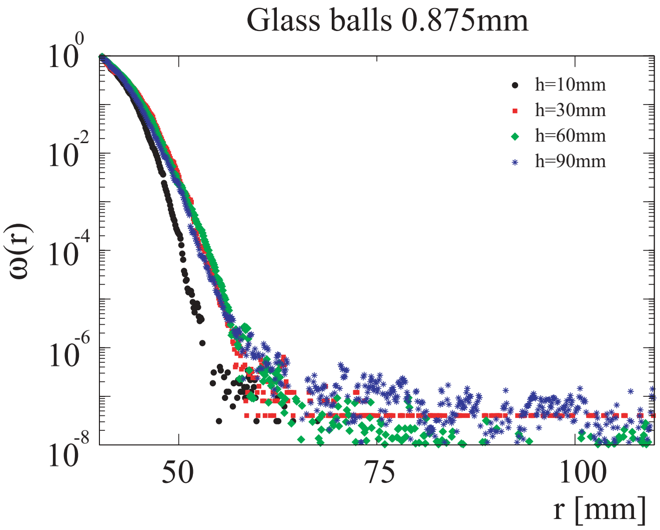

Figure 6.7: Velocity profiles measured in the Couette geometry for 0.875 mm glass beads at different filling height H. In this geometry the shear zone is always located at the inner cylinder, and the profiles are seen to converge with increasing H onto a single curve.

is seen to be a progressive evolution towards the narrow shearband. When the shear zone first starts to localize ($H = 50$ mm), it only overlaps with the asymptotic Couette profile close to the inner cylinder. When H is increased, the overlap extends further and further away from the inner cylinder. In the wall collapsed regime the velocity profile at the surface is thus found to be independent of the bottom topography, and it therefore makes sense to speak of a single, asymptotic profile for large H.

We have measured these asymptotic velocity profiles in the Couette geometry for grains of various shapes and polydispersities. Figure 6.9 shows profiles for (a) 1 mm glass beads (smooth, spherical, highly polydisperse), (b) 3 mm glass beads (smooth, spherical, approximately monodisperse), (c) 1.3 mm plastic flakes (rough, irregularly shaped, highly polydisperse, soft), and (d) 2.3 mm grind sand (rough, irregularly shaped, highly polydisperse, hard). Despite the large variation in grain properties, we find that, away from the inner cylinder, the velocity decays approximately exponentially in all cases.

To quantify this, we have fitted these velocity profiles to equation (6.6). However, as is clear from Figures 6.6 and 6.7, the pure exponential tail can

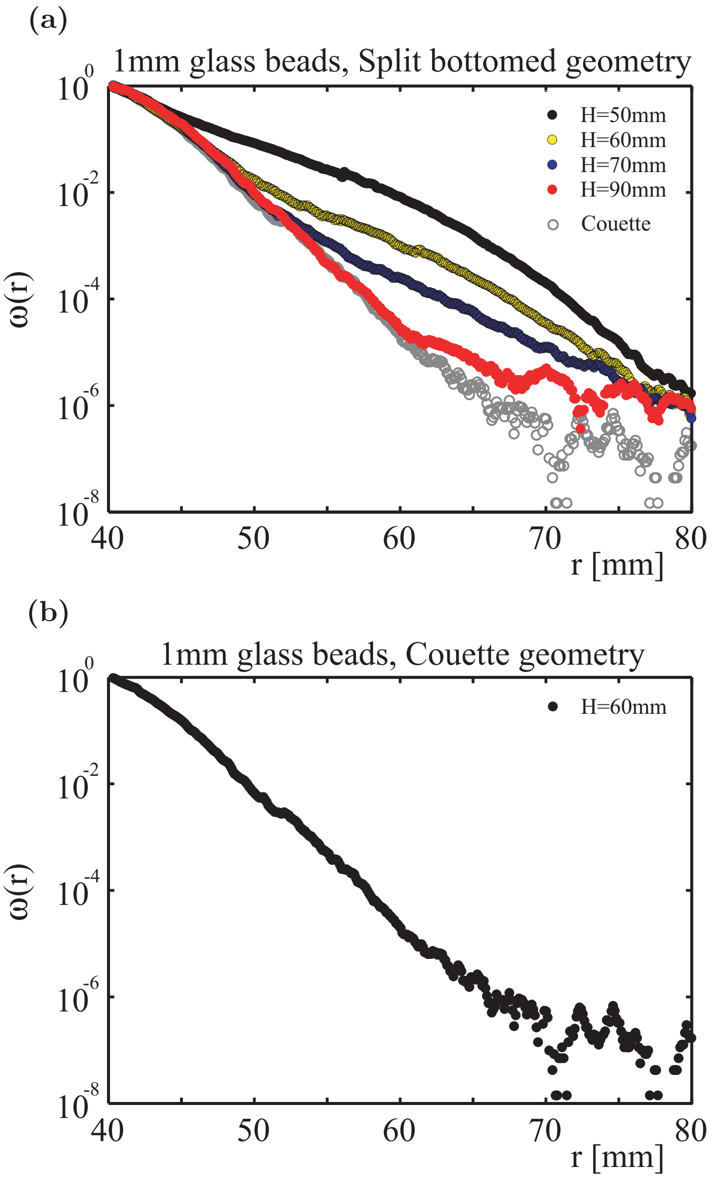

Figure 6.8: Velocity profiles for 1 mm glass beads measured in the split-bottomed setup (a), and Couette geometry (b). The open circles in (a) corresponds to the profile shown in (b), illustrating that the measurements for the split-bottomed geometry converge towards the Couette profile for large H.

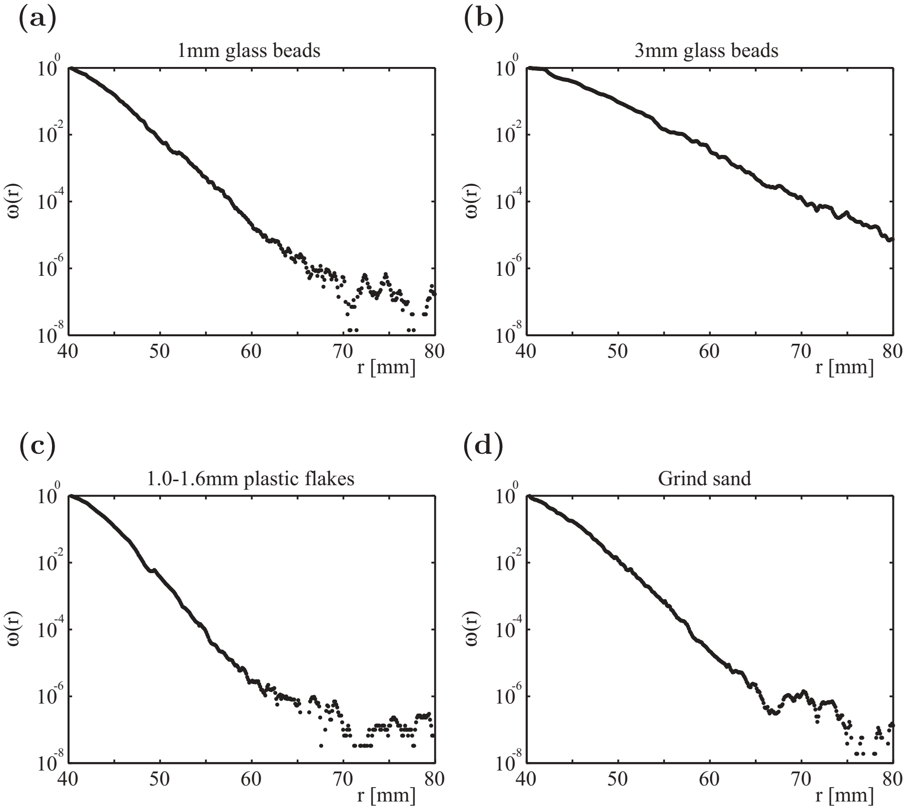

Figure 6.9: Velocity profiles measured in the Couette geometry for grains of different shape and polydispersity: (a) Polydisperse glass beads ($\langle d_p \rangle \sim 1.3$ mm), (b) Monodisperse glass beads ($\langle d_p \rangle \sim 3.2$ mm), (c) Irregular plastic flakes ($\langle d_p \rangle \sim 1.3$ mm), and (d) Irregular grind sand ($\langle d_p \rangle \sim 2.3$ mm). In all four cases the velocity is seen to decay approximately exponential away from the inner cylinder, apart from a narrow region near the side wall, where the profile is curved.

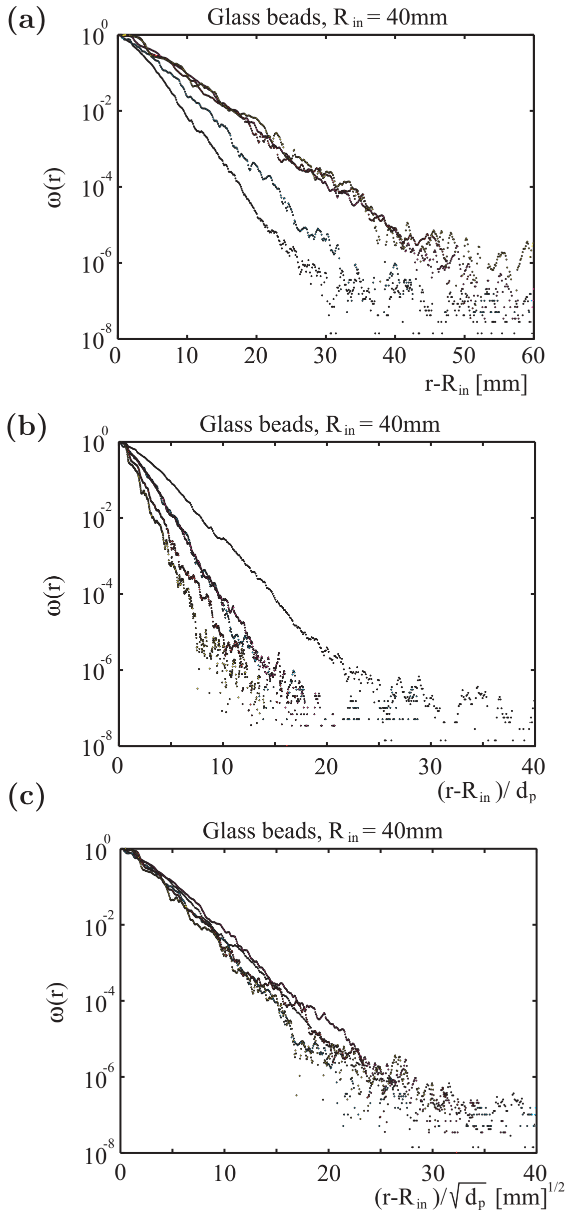

Figure 6.10: Velocity profiles for glass beads ranging from $\langle d_p \rangle \sim 1.3$ mm to 5.0 mm, in the Couette geometry at filling height $H = 60$ mm, with an inner cylinder of radius $R_{in} = 40$ mm. (a) The velocity profiles for the larger particles decay slower than the smaller ones. (b) Here the radial coordinate $r - R_{in}$ has been non-dimensionalized with d_p; to our surprise, the data collapse is rather poor. (c) When the radial coordinate is rescaled as $(r - R_{in})/\sqrt{d_p}$, the data collapse is rather good.

material	$\langle d_p \rangle$	b	c
0.875 mm glass beads	0.9 mm	0.877	0.013
1 mm glass beads	1.2 mm	0.581	0.004
2 mm glass beads	2.4 mm	0.465	0.003
3 mm glass beads	3.2 mm	0.319	−0.003
4 mm glass beads	4.0 mm	0.338	−0.002
5 mm glass beads	5.0 mm	0.344	−0.001
6 mm glass beads	6.0 mm	0.149	−0.003
1.3 mm plastic flakes	1.3 mm	0.739	0.001
2.3 mm grind sand	2.3 mm	0.621	0.006

Table 6.3: Values obtained by fitting equation (6.6) to the velocity profiles in the range $\omega(r) = [10^{-1}, 10^{-5}]$, measured for the inner cylinder with size $R_i = 40$ mm (see text).

material	$\langle d_p \rangle$	b	c
0.875 mm glass beads	0.9 mm	0.545	−0.001
1 mm glass beads	1.2 mm	0.903	0.005
2 mm glass beads	2.4 mm	0.574	−0.001
3 mm glass beads	3.2 mm	0.437	−0.005
4 mm glass beads	4.0 mm	0.332	−0.001
5 mm glass beads	5.0 mm	0.260	0.003
6 mm glass beads	6.0 mm	0.372	−0.005

Table 6.4: The parameters acquired by fitting the experimental data in the range $\omega(r) = [10^{-1}, 10^{-5}]$ to equation (6.6), for the inner cylinder sized $R_i = 20$ mm.

be observed for a limited range in r only. Very close to the inner cylinder, wall effects apparently lead to the bending of the velocity profile, and far away from the cylinder, when ω becomes less than $10^{-5} \sim 10^{-6}$, our data becomes dominated by noise. We have therefore, for all data sets, limited the range of r such that $10^{-5} < \omega(r) < 10^{-1}$. We then first take the log of ω (since we do not want to let our fits be dominated by the largest values of ω), and then fit $\log \omega(r)$ to a quadratic expression: $\log(\omega(r)) = a - br - c(r - r_0)^2$, where r_0 is chosen in the middle of the fitting range. The results of these fits, for $R_{in} = 40$ mm and 20 mm are shown in Tables 6.3 and 6.4. For all particles we find that c is typically two orders of magnitude smaller than b: the tails are in this regime, in very good approximation, pure exponential.

This may appear to contradict the findings in [2], where the profiles for irregularly shaped, polydisperse grains were found to be purely Gaussian. However, in [2] only the first one to two decades where studied, and it is precisely there that we also see some rounding of the curves. Notice that in [2], layering effects present for monodisperse, spherical grains where suggested as an explanation for the exponential tails. Away from the side wall and for polydisperse or rough particles, such layering effects should be weak, and it was argued that in this case Gaussian tails would be observed [2]. This, however, is in contrast to our findings, and the question what determines the functional shape of tails of shear zones is open, in particular because in the bulk always Gaussian tails are found.

In conclusion: for a wide range of particles sizes and geometries, wall collapsed shear bands exhibit exponential tails away from the wall. Therefore, a single number, the decay exponent b, characterizes the main features of these shear bands. In the next Section we will study how this decay exponent varies with particle size and experimental geometry.

6.5 Scaling of wall-collapsed shear bands

From Figure 6.9(a-b) it is clear that the decay of the velocity profiles depends on particle size: $\omega(r)$ decays faster for smaller particles. Table 6.3 confirms this observation for the glass beads with $\langle d_p \rangle$ ranging from 0.9 mm to 3.2 mm, where the exponential prefactor b decreases with particle size, while the Gaussian one c remains approximately constant.

What length scales are present that could influence the spatial decay rate b of the wall-collapsed shear bands? The height of the layer does not play a role, and neither does the location of the split (if present), so that leaves the average particle size $\langle d_p \rangle$ and radius of the inner cylinder R_{in} as the most obvious length scales. For the wide shear zones in the bulk, the width was shown to be independent of R_{in} and R_s. For the narrow shear bands studied here, this is certainly what one would expect, since their decay is fast and appears to be on the grain scale. The relatively large radius of curvature could be expected to be irrelevant, and $\langle d_p \rangle$ would then be the only relevant length scale.

In Figure 6.10a we plot the profiles measured in the Couette geometry for glass beads with $\langle d_p \rangle$ ranging roughly from 1.2 to 5.0 mm. Figure 6.10b shows that the naive expectation that the decay of $\omega(r)$ would scale with particle size, i.e., that plotting the data as function of $\omega((r-R_{in})/d_p)$ would yield a universal master curve, is not correct. The rescaling of the radial coordinate with d_p strongly overestimates the change in the decay rate b with d_p. To our great surprise, plotting the data as function of the rescaled radial coordinate $(r - R_{in})/\sqrt{d_p}$ causes the data to collapse quite convincingly, as shown in 6.10c. The only reasonable conclusion appears to be that there is an additional length scale in the problem that is relevant for these profiles; as discussed above, R_{in} could also play a role. From dimensional analysis it then follows that one then would expect that $\omega(r/(d_p^{\zeta} R_{in}^{1-\zeta}))$ should collapse, and the previous analysis suggests that $\zeta \approx 0.5$.

To check whether the value of the inner radius indeed influences the asymptotic decay, we have constructed two other inner cylinders, one with $R_{in} = 20$ mm and one with $R_{in} = 2.5$ mm. Figure 6.11 shows profiles for (a) 1 mm and (b) 2 mm glass beads obtained for two different inner cylinders, R_{in}=20 mm and 40 mm. Rescaling the radial coordinate with the square root of the inner cylinder and plotting $\omega((r - R_{in})/\sqrt{R_{in}})$, causes a good collapse of the curves for different R_{in}, as illustrated in Figures 6.11c-d for 1 mm and 2 mm glass beads respectively.

In the previous pictures we have shown that the spatial decay rate scales with the square root of both d_p and R_{in}. Combining these two findings, the proper non-dimensional radial coordinate x should be takes as:

$$x := \frac{r - R_{in}}{\sqrt{R_{in} \times d_p}} \ . \tag{6.7}$$

Figure 6.12 shows the resulting data collapse of $\omega(x)$.

This result can be interpreted as follows. Clearly, when both particle size and shear cell geometry would be diluted, the resulting decay rate should scale trivially. Hence, the scaling above can be rewritten as $x = (r - R_{in})/(d_p \times \sqrt{R_{in}/d_p})$, where R_{in}/d_p is the non-dimensional radius of curvature. Apart from this curvature, ω scales trivially with d_p. What is puzzling is that if this result also holds in the limit of straight sidewalls, where $r_{in} \to \infty$, the exponential decay rate would go to zero. The limit of very small R_{in} is also of interest. In Figure 6.13a we show that for small inner radius $R_{in} = 2.5$ mm, the spatial decay rate is even larger, although the scaling with $\sqrt{R_{in}}$ does not hold here anymore; indeed since particle size and radius of curvature are comparable, its unclear what happens here.

A final comment that can be made, is that even though so far we have taken R_{in} as determining the radius of curvature, strictly speaking, one should use the local value of r. As a result, for large particles and small values of R_{in}, one may even expect to see a gradual variation of the exponential decay rate. In Figure 6.13b, we show data for $R_{in} = 2.5$ mm and for increasingly large particles. Indeed, the spatial decay rate appears

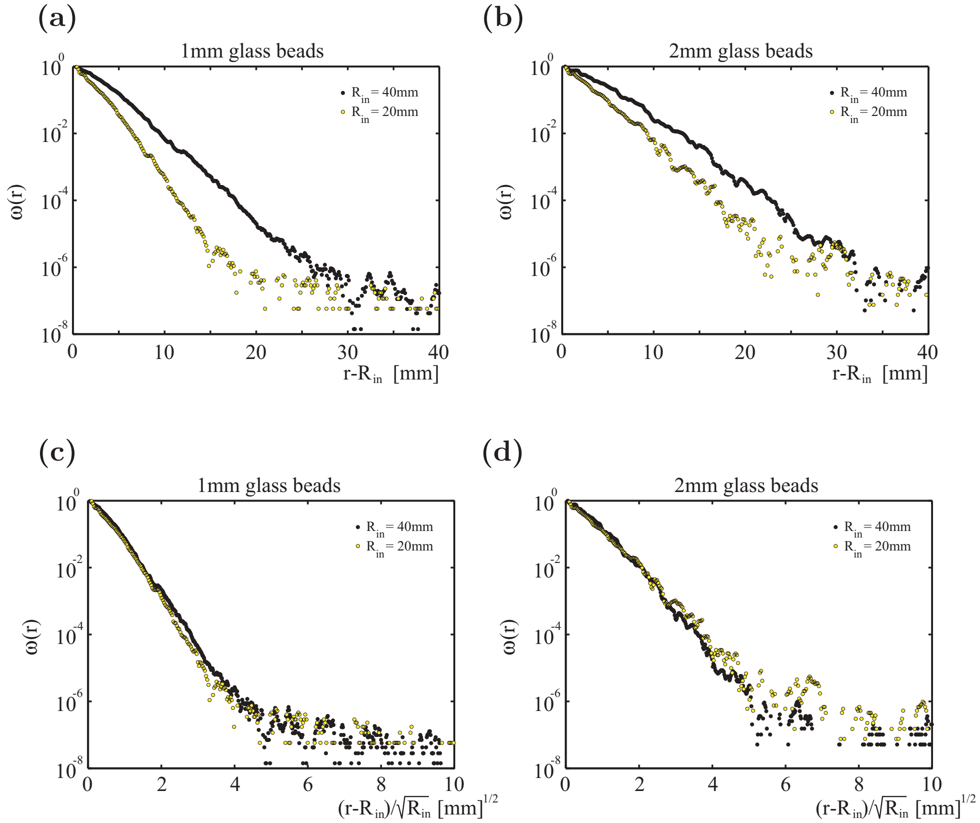

Figure 6.11: Velocity profiles for 1 mm and 2 mm glass beads for inner cylinders with $R_{in} = 20$ mm and 40 mm. (a-b) For both particle sizes, the velocity profile decays fastest for the smallest inner cylinder. (c-d) By rescaling the radial coordinate with the square root of the size of the inner cylinder, the two curves collapse onto a single curve.

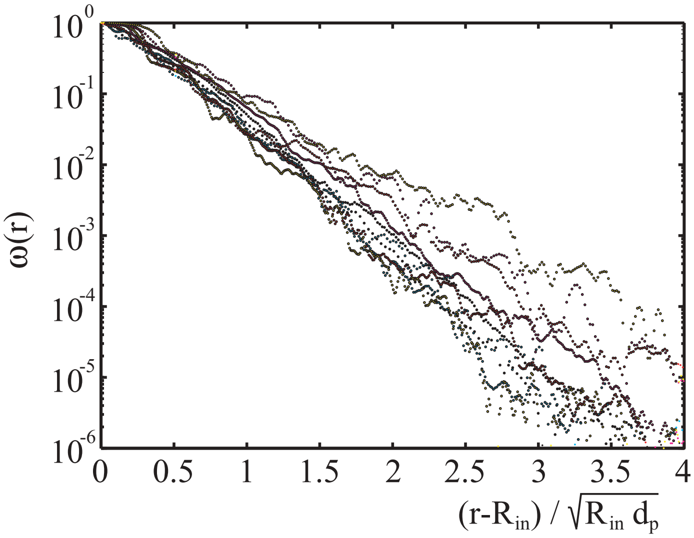

Figure 6.12: Rescaled velocity profiles for glass beads of average size $\langle d_p \rangle$ 1.2 mm to 5.0 mm for the two inner cylinders with radii R_{in}=20 and 40 mm. When rescaled according to $(r - R_{in})/\sqrt{R_{in} \times d_p}$ a reasonable overlap is found, especially in the first three decades.

to diminish for increasing r, leading to the upward curving of the velocity profiles.

6.6 Conclusion and discussion

In this Chapter, both wide shear bands in the bulk and narrow shear bands forming near the inner cylinder of Couette-like rheometers have been studied in detail. The main new findings are the robustness of the exponential tails of the wall collapsed shear bands, and the surprising scaling of the corresponding spatial decay rate.

There are two possible caveats. First of all, there is a substantial convection roll present for the wall collapsed shear bands, and we do not know what its effect is on the velocity profiles, and in particular their tails. It is difficult to control this convection, although we are planning experiments with various surface treatments of the rough inner cylinder. The vertical grooves employed here could enhance convection, while completely rough surface may suppress is; this is left for further work.

Secondly, the measurements of ω over almost six decades are technically

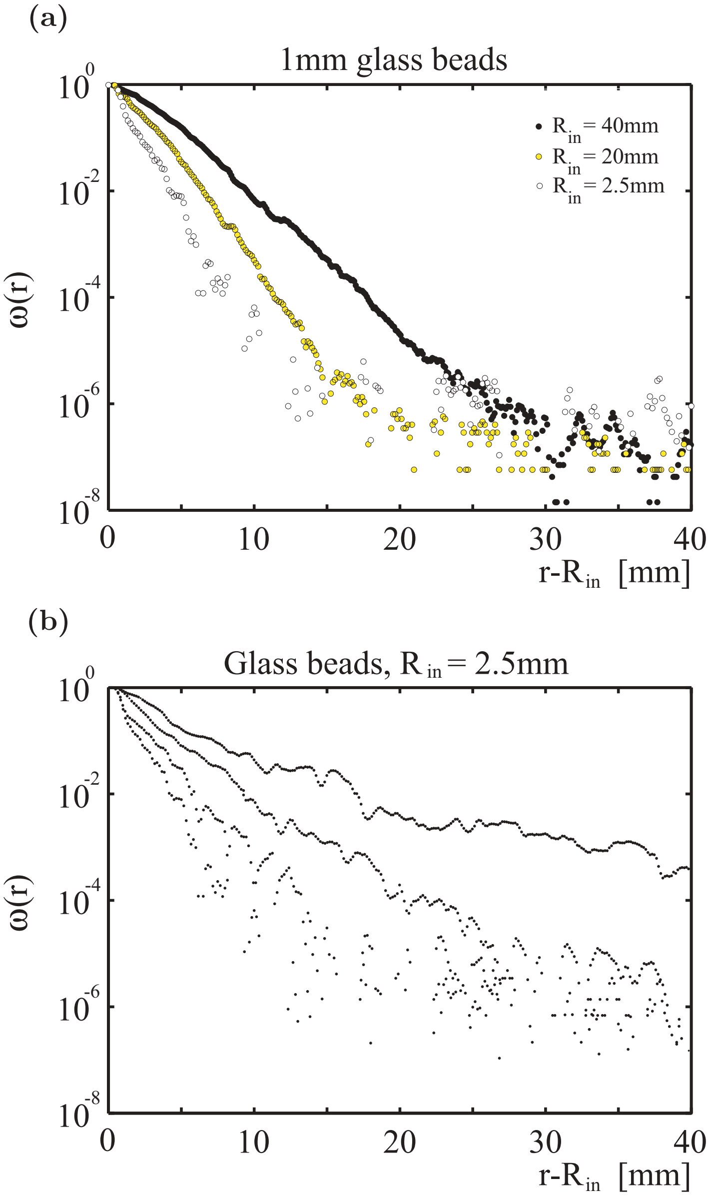

Figure 6.13: (a) Velocity profiles for 1 mm glass beads for three different inner cylinders. (b) Upward curving of velocity profiles for the largest particles ($\langle d_p \rangle = 1.2, 2.4, 3.2, 6.0$ mm) and small R_{in}.

convoluted. Preliminary investigations indicate that deep in the tail regime, i.e. for small values of ω, fluctuations are relatively strong. It is not clear how strong these fluctuations influence the measured values of ω when these are of the order 10^{-4} or less.

To investigate the role of both the convection and the fluctuations further, one could imagine tracking (colored) particles in the regime where ω approaches zero. Their motion will give detailed information on the radial component, on the fluctuations, and finally also on the average value of the azimuthal velocity, which then can be compared to the values obtained by our PIV method.

References

[1] L. Bocquet, W. Losert, D. Schalk, T. C. Lubensky, and J. P. Gollub, Phys. Rev. E **65**, 011307 (2001).

[2] Daniel M. Mueth, Georges F. Debregeas, Greg S. Karczmar, Peter J. Eng, Sidney R. Nagel, and Heinrich M. Jaeger, Nature **407**, 385 (2000).

[3] T. S. Komatsu, S. Inagaki, N. Nakagawa, and S. Nasuno, Phys. Rev. Lett. **86**, 1757 (2001).

[4] Denis Fenistein and Martin van Hecke, Nature **425**, 256 (2003).

[5] Denis Fenistein, Jan Willem van de Meent, and Martin van Hecke, Phys. Rev. Lett **92**, 094301 (2004).

[6] J.-C. Tsai, G. A. Voth, and J. P. Gollub, Phys. Rev. Lett. **91**, 064301 (2003).

[7] R. Khosropour, Jessie Zirinsky, H. K. Pak, and R. B. Behringer, Phys. Rev. E **56**, 4467 (1997).

Chapter 7

Conclusion

In this thesis we have explored granular media that are driven in a variety of manners. Chapters 2-4 deal with compartmentalized, vibrofluidized granular gases, Chapter 5 deals with impact of a heavy object on fine sand, and Chapter 6 concerns the slow flow of granular media in shear cells.

The findings described in Chapter 3, which concerns a numerical study of the role of fluctuations in compartmentalized granular gases, can be summarized as follows. First of all, the statistical fluctuations profoundly influence the clustering behavior of a compartmentalized granular gas. As long as the number of particles N is sufficiently large, the clustering still largely follows the lines of a standard second-order phase transition (i.e., a pitchfork bifurcation with critical exponent $\beta = 1/2$). For smaller N, however, the enhanced influence of statistical fluctuations breaks the mean-field behavior. We demonstrated this by means of bifurcation diagrams and also via the diverging correlation time at the clustering transition.

In order to model the fluctuations in our system, we constructed a mapping describing the particle exchange between two compartments per shaking cycle, in which the mean-field flux and the fluctuations appear as two separate terms. This separation enables us to directly compare the relative importance of both contributions to the dynamics and to study how the fluctuations start to dominate for decreasing particle number N. Our results show that already at $N = 300$ (i.e., much less than the 10^{23} particles of textbook statistical physics) mean-field results and the Eggers flux theory hold very nicely. Only for smaller N does the finite-number noise start to dominate, and the mean-field description breaks down.

In Chapter 4, clustering in bidisperse granular gases was studied. The main conclusion of this work is that experiment, theory, and numerics all agree on the phenomenon of competitive clustering in a bidisperse granular gas: The clustering can be directed either towards the compartment initially containing the majority of the large particles (type-I clustering) or to the one containing mainly small particles (type-II) simply by adjusting the shaking strength.

The best quantitative agreement with the theoretical flux model is found when the size ratio between the large and small particles is not too much larger than 1. This can be traced back to the fact that in the model the granular temperatures of the different species are assumed to be equal, which is an accurate assumption only when these particles have similar sizes. Since the region of competitive clustering is found to move closer and closer towards this limit when we let the number of large particles grow, this means that the theory works best for comparatively large numbers of large particles.

In Chapter 5, we studied the impact of a heavy sphere on a loosely packed bed of fine sand. This results in the formation of a splash and a jet which rises straight up into the air. The jet is created as the crater formed by the impact collapses due to the sand pressure. For a sufficiently high impact velocity we find that air is entrained beneath the surface. This entrained air bubble then slowly rises to the surface where it causes a granular eruption. We have described the void collapse by a simple Rayleigh-type model, and found good agreement with experimental findings.

In Chapter 6 both wide shear bands in the bulk and narrow shear bands forming near the inner cylinder of Couette-like rheometers have been studied in detail. The main new findings all concern the wall collapsed shear bands. We have shown how, for the split-bottomed geometry, the profiles exhibit a sharp crossover between the asymptotic wall profile for small radii, and a less steep decay for large radii. The asymptotic profiles for split-bottomed and ordinary Couette cells were found to be equal. This leads to the first main conclusion that for sufficiently deep layers, the velocity profile of wall-collapsed shear bands does not depend on the bottom topography.

Moreover, we have found that for a wide variety of particle shapes and polydispersities, the asymptotic velocity profiles tend to an exponential decay away from the inner cylinder. This contrasts earlier work, which suggested that only when layering effects are present an exponential tail is found. And in turn, layering effects would only occur for monodisperse, spherical particles. Interestingly, in our setups we can obtain both Gaussian and exponential tails, independent of particle shape or polydispersity.

The exponential tails can be characterized by a single number, the spatial decay rate. We found that the decay rate does not only depend on particle size, but also on the radius of curvature. This contradicts a large body of generally accepted evidence in the literature on granular shear bands, and questions what will happen in geometries where the curvature can be neglected.

The above results can all be translated to practical problems, and to possible solutions. The clustering experiments in compartmentalized systems are relevant for industrial conveyor belts and sorting machines. Our results may be useful to develop production lines in which granular clustering is minimized. Also the demixing of granular mixtures described in Chapter 4 is a major problem in numerous industries that depend on well-mixed granulates. Based on our results, mixers can be made more efficient if they can adjust the shaking strength to the local distribution of large and small particles, thus taking advantage of the competitive clustering effect. Granular jets, as described in Chapter 5, may be relevant to processes occuring in nature, such as meteorite impacts. It is conceivable that the material ejected by impacts (via the enormously upscaled splash and jet) contributes significantly to the exchange of matter between planets.

Finally the onset of shearing motion, as described in Chapter 6, is of paramount importance in understanding how landslides and avalanches are triggered. Knowing the fundamental characteristics of granular shear flows may be essential in detecting potential shear bands, and thus contribute to the development of improved warning systems.

Summary

Granular media, such as sand, flour and boulders, exhibit strongly energy dissipating interactions. Indeed, a marble thrown into a bucket of marbles does not bounce back, and a pile of sand at rest does not exhibit any dynamics. Therefore, to see some interesting dynamics, energy has to be supplied to these systems. In this thesis, three different methods of energy input are explored: shaking, impacting, and shearing.

To study clustering in granular gases in a controlled fashion, grains are put into a container divided into two compartments by a wall (see Chapter 2). When this container is shaken violently, the grains jump around inside the container, colliding with the walls and each other. When the shaking strength is reduced below a certain critical value, a peculiar phenomenon can be witnessed: the grains begin to accumulate into one of the compartments. Hence, the symmetric distribution of particles found for violent shaking, in which both compartments contain an approximately equal number of grains, gives way to an asymmetric particle distribution. This can be understood as follows: Collisions between grains are inelastic, and energy is dissipated in every collision. At reduced shaking strengths the energy input from the vibrating bottom is not able to overcome this energy dissipation. As a result, any fluctuation whereby one compartment becomes slightly more densely populated, causes more energy to be dissipated here; the density will increase further and particles will find it difficult to escape. Ultimately, this leads to the formation of a stable asymmetric particle distribution. This clustering behavior is well described by a theoretical flux model, which expresses the particle flux as function of the numbers of particles in the compartments and the shaking strength.

For a large number of particles in the system, the transition to the clustered state is smooth and continuous. In Chapter 3 the effect of lowering the total number of particles in the system on the clustering transition is studied. For small number of particles, fluctuations in the particle flux between the two compartments become strong, and at some point the mean-field behavior of the transition is overwhelmed by the fluctuations.

The clustering behavior of a bi-disperse mixture of particles, i.e, a mixture of particles of two different sizes, is studied in Chapter 4. Depending on the initial particle distribution, such a mixture is experimentally found to cluster competitively: By tuning the shaking strength, the clustering can be directed either towards the compartment initially containing the majority of the large particles or to the one containing the majority of the small particles. These findings have been verified in molecular dynamics simulations and in an extended, bi-disperse version of the flux model.

Chapter 5 is on the mode of energy input through impact: When a heavy sphere falls onto a loose bed of sand, a splash is formed above the surface. Then a narrow jet rises straight up into the air. This phenomenon is studied in detail by performing experiments for different impact velocities. We found that the sequence of events is as follows. First, the sphere penetrates down into the sand. This forms a cylindrical crater which then collapses due to the sand pressure. The inward flowing sand then focuses into two jets, one upward and one downward. The former reaches heights exceeding the release height of the sphere. For high impact velocities the crater collapses long before the sphere comes to a standstill, and air is entrained below the surface. This air bubble slowly rises towards the surface where it causes a granular eruption.

Finally, if an external stress is imposed on a dense granular medium, it does not flow as a normal fluid would do under the same conditions. Instead a narrow shear band is formed where the material yields and flows, while the rest of the material remains solid-like and barely deforms. The differences between shear bands located in the bulk and near a wall are studied in Chapter 6, with emphasis on the transition between the two regimes. For shear bands in the bulk the tails of the velocity profiles are found to follow a Gaussian profile, while wall-localized shear bands are found to decay exponentially away from the wall. Surprisingly, the spatial decay rates of the exponential tails do not simply scale with particle size, but also the radius of curvature is found to play an important role, challenging accepted views on shear bands.

Samenvatting

Granulaire materialen, zoals zand, meel en keien, vertonen een wisselwerking die sterk dissipatief is. Zo zal een knikker die in een zak met knikkers valt niet terug stuiteren, en een hoop zand blijft gewoon rustig liggen zonder vormverlies. Om interessante dynamica te zien in deze systemen moet men er energie aan toevoegen. In dit proefschrift worden drie verschillende manieren van energietoevoer beschouwd: schudden, een inslag van buitenaf, en het aanbrengen van een afschuifspanning.

Teneinde het clustergedrag in granulaire gassen te bestuderen, doen we enkele honderden kogeltjes in een vat, dat door middel van een lage wand verdeeld is in twee gelijke compartimenten (zie Hoofdstuk 2). Wanneer het vat heftig geschud wordt, vliegen de kogeltjes alle kanten op, voortdurend botsend met de wanden en met elkaar. Dit is een granulair gas. Wanneer nu de schudsterkte omlaag geschroefd wordt tot onder een bepaalde kritische waarde neemt men een merkwaardig fenomeen waar: de kogeltjes verzamelen zich in n enkel compartiment. Dat wil zeggen, de verdeling van de deeltjes over de twee compartimenten wordt asymmetrisch. Dit is een gevolg van het feit dat de botsingen tussen de kogeltjes niet volkomen elastisch zijn; bij elke botsing gaat een gedeelte van de kinetische energie verloren. Bij lage schudsterkte is de energietoevoer van de trillende bodem niet meer voldoende om dit energieverlies te overstemmen. Een kleine fluctuatie in de verdeling, waarbij het ene compartiment wat meer deeltjes bevat dan het andere, betekent dat er in het eerste compartiment meer botsingen plaatsvinden en dus meer energie verloren gaat. De kogeltjes worden daar dus langzamer en ontsnappen minder gemakkelijk uit het compartiment, met als resultaat dat de dichtheid nog verder omhoog gaat. Dit leidt uiteindelijk tot stabiele, asymmetrische dichtheidsverdeling over de twee compartimenten: een cluster van langzame deeltjes in het eerste compartiment, en slechts enkele (maar veel snellere) deeltjes in het tweede compartiment. Deze clustering is uitstekend te beschrijven met een theoretisch fluxmodel, dat de deeltjesstroom van het ene naar het andere compartiment uitdrukt als functie van het aantal deeltjes in het compartiment en de schudsterkte.

Als het aantal kogeltjes in het systeem voldoende groot is, verloopt de overgang naar de geclusterde toestand precies volgens de mean field theorie van faseovergangen. In Hoofdstuk 3 wordt bestudeerd hoe dit verandert naarmate het aantal deeltjes kleiner wordt gemaakt. Voor kleine deeltjesaantallen wordt de invloed van statistische fluctuaties in de flux steeds groter, en tenslotte gaat het mean field gedrag verloren in de ruis.

In Hoofdstuk 4 beschouwen we een bidispers mengsel van grote en kleine kogeltjes. Uit onze experimenten blijkt dat de clustering in een dergelijk mengsel competitief is: Afhankelijk van de schudsterkte zullen de deeltjes clusteren in het compartiment dat aanvankelijk de meeste grote kogeltjes bevat of in het compartiment met de meeste kleintje kogeltjes. Deze verrassende experimentele uitkomst wordt bevestigd en nader uitgewerkt door middel van moleculaire-dynamica simulaties en via een uitgebreide, bidisperse versie van het fluxmodel.

In Hoofdstuk 5 richten we onze aandacht op een andere wijze van energietoevoer, wanneer we een metalen kogel op een bed van losgewoeld zand laten vallen. Bij de inslag is eerst een splash te zien, bestaande uit zandkorrels die weggeslingerd worden vanuit het centrale punt van inslag, en kort daarna schiet een jet van zand loodrecht de lucht in. We leggen dit in detail vast met behulp van een hoge-snelheidscamera, voor verschillende inslagsnelheden van de kogel. De volgorde van de gebeurtenissen is als volgt: Eerst boort de kogel zich in het zand, en vormt daarbij een cilindrische krater die daarna weer ineenklapt onder invloed van de druk in het zand. Op de as van de krater vormt zich een drukmaximum en het toestromende zand wordt omhoog en omlaag geperst in de vorm van twee jets. De omhoog gerichte jet komt in onze experimenten altijd hoger dan de hoogte waarvan de kogel wordt losgelaten.

Voor hoge inslagsnelheden sluit de krater zich al voordat de kogel tot stilstand komt, en dit betekent dat er een flinke hoeveelheid lucht ingevangen wordt tussen het punt waar de krater zich sluit en de kogel. Deze lucht stijgt, in de vorm van een bel, omhoog door het zand en veroorzaakt bij het bereiken van de oppervlakte een eruptie die doet denken aan kokend water, of zelfs een vulkaan.

Tot slot wordt in Hoofdstuk 6 de reactie van een granulair medium op een externe afschuifspanning bestudeerd. Het gedrag blijkt heel anders te zijn dan voor een gewone vloeistof. Er vormt zich een smalle shear band waarbinnen het materiaal meegeeft aan de afschuifspanning en gaat stromen, terwijl de rest vrijwel volledig in rust blijft en nauwelijks vervormt. We richten ons in het bijzonder op de verschillen tussen de shear bands in het midden van het medium en die vlak bij de wand, en bestuderen de overgang tussen deze twee regimes. De shear bands in het midden van het medium vertonen een snelheidsprofiel met een zogenaamde Gaussische staart, en die vlakbij de wand hebben een exponentile staart. Verrassend genoeg schaalt deze exponentile staart niet alleen met de grootte van de granulaire deeltjes, zoals algemeen werd aangenomen in de literatuur over shear bands, maar daarnaast blijkt ook de kromtestraal van het systeem een belangrijke rol te spelen.


PH-STL
PH-STL

Acknowledgements

The work presented in this thesis is the results of the efforts of several people. I would like to thank my supervisor Detlef Lohse for giving me the chance to be introduced to the physics of granular matter. I am also very grateful to Ko van der Weele and Devaraj van der Meer who both have played major roles during my research, particular in the work on clustering in granular gases. Special thanks to Martin van Hecke for giving me the chance to work on sheared granular matter, and for the intense assistance during the final part of my research. Furthermore I would like to thank all my colleges in Twente and Leiden for the many hours spend discussing physics, as well as other issues, at various offices, labs, and conferences.

None of the experiments carried out during my research would have been possible without technical assistance. I am very grateful to the Twente technicians Gert-Wim Bruggert and Henni Scholten for the construction of various setups and their assistance to many problems, as well as for introducing me to genuine "twents". Also big thanks to Jeroen Mesman at the fine-mechanics workshop in Leiden, and to Bas Benschop for assistance with computer (and car) related problems.

I would like to thank the people at *V.V. Drienerlo* for soccer related activities. Special thanks to the proud members of Veld 3 for participating in the numerous defeats and occasional victories at various soccer fields in and around Enschede, and for the frequent 3rd-half triumphs.

Thanks to the members of *Parachutisten Centrum Midden Nederland* (PCMN) for introducing me to the fantastic world of skydiving, the never failing to function rental gear, and the PH-STL and PH-TGC for the hours and hours spend climbing to altitude.